Winter 2018

EXPERIMENTAL EVALUATION OF FATIGUE TEST SETUP FOR A GUSSET-LESS TRUSS CONNECTION

Duncan William McGeehan
University of New Hampshire, Durham

EXPERIMENTAL EVALUATION OF FATIGUE TEST SETUP FOR A GUSSET-LESS TRUSS CONNECTION

BY

Duncan W. McGeehan

BS, University of New Hampshire, 2017

THESIS

Submitted to the University of New Hampshire in Partial Fulfillment of the Requirements for the Degree of

Master of Science in Civil Engineering

December, 2018

This thesis/dissertation has been examined and approved in partial fulfillment of the requirements for the degree of Master of Science in Civil Engineering by:

Thesis Director, Erin Santini Bell, Ph.D., P.E. Civil and Environmental Engineering

Ricardo A. Medina, Ph.D., P.E. Civil and Environmental Engineering

Eshan V. Dave, Ph.D. Civil and Environmental Engineering

On December 6th 2018

Original approval signatures are on file with the University of New Hampshire Graduate School.

ACKNOWLEDGEMENTS

I would like to acknowledge the NHDOT (New Hampshire Department of Transportation) for their technical and financial support throughout this project. This work was partially supported by National Science Foundation Grant #1430260. Any opinions, findings, and conclusions or recommendations expressed in this material are those of the author and do not necessarily reflect the views of the National Science Foundation.

I would like to sincerely thank my advisor, Dr. Erin Santini Bell, who was the PI of this project, for her continued support, guidance, and patience throughout this work. I would like to sincerely thank Dr. Ricardo A. Medina, the Co-PI of this project, for his tireless efforts towards this work. Both Dr. Bell and Dr. Medina were incremental in maintaining forward progress and focus on the goals of this research despite the many setbacks that we have faced. I would also like to thank Dr. Eshan V. Dave for his support throughout my time at UNH, and his willingness to lend his time and knowledge when needed.

I would like to thank Fernanda Fischer for her efforts in the start of this project and laying the groundwork for this study. Thank you to Shokoufeh Zargar, for her input and expertise along the way. Thank you to all the people who helped move this project forward along the way; John Ahern, Scott Campbell, Dr. Gary Schajer, Andrew Lanza, Christian Harris. I would also like to thank my friends and officemates for all the fun along the way, and my family for all the support. Last but certainly not least, I would like

to extend a special thank you to Ashley Blum for her continued support and encouragement in all my pursuits.

TABLE OF CONTENTS

LIST OF FIGURES

LIST OF TABLES

ABSTRACT

EXPERIMENTAL EVALUATION OF FATIGUE TEST SETUP FOR A GUSSET-LESS TRUSS CONNECTION

by

Duncan W. McGeehan

University of New Hampshire, December 2018

In 2013, the newly designed Memorial bridge, located between Portsmouth, NH, and Kittery, ME, was opened to traffic. The structural system of the bridge is composed of truss elements with a unique "Gusset-less" connection which utilizes curved steel to transition from the chords to the diagonals where splice plates join the members. With such a unique connection, it is important to verify the design assumptions and assess the performance. In this study, the fatigue performance of the Gusset-less connection is investigated through an experimental fatigue test of a scale model of the connection.

In a high-cycle fatigue test, it is critical to ensure that consistency is maintained across all testing periods. This is especially challenging when the test setup is not standardized, and the laboratory infrastructure is limited. In this work a monitoring protocol was developed to systematically monitor the structural response of the test setup. Using this protocol, across a total of 1,600,000 fatigue load cycles the average difference in structural response was found to be 5% across the test setup. Using the most conservative assumptions, using a hot-spot stress of 14 Ksi at the toe of the weld, the

AASHTO S-N curve, and a category C fatigue detail, the connection has been tested and the results show that the design expectations are exceeded.

The residual stresses were investigated in the top-flange of the fatigue specimen. The stresses indicate a compressive stress at the surface of the specimen, which is consistent with the residual stress profile of a sand blasted metal. The magnitude of the stresses was higher than the theoretical limits of the calculation method and therefore must be used qualitatively, not quantitatively.

1. INTRODUCTION

This chapter will provide background information on the project. Following the background, an overview of the objectives of this work will be outlined. Finally, background information on fatigue testing, measurement methods used, fatigue test monitoring, Finite Element Modeling (FEM), and residual stresses will be outlined, and a literature review provided.

1.1 Project Overview

The Memorial Bridge spans the Piscataquis river between Portsmouth, NH, and Kittery, ME. The original Memorial Bridge had been in operation since 1923, when it was opened to traffic originally, making it over 89 years old when it was officially closed in 2012 due to structural deficiencies. The original design was a vertical lift bridge utilizing a traditional steel truss structural system, where the center span of the three-span bridge was the vertical lift span. In 2013 the new Memorial Bridge, designed by HNTB corp., was opened to traffic. The new bridge utilized a similar design with a lift-span in the center and a steel truss structural system. One of the major changes was the innovate connection designed for the members of the truss system.

In most bridges that use a steel truss structural system, the connections between the members are made using gusset plates. When using gusseted connections, there are multiple structural members framing into one joint, where the gusset plates are bolted

and/or welded to each side of the members. Although widely used and studied, the gusset plate connections have a few major drawbacks, such as the following;

- Gusset plates make inspections more difficult. Specifically, the plates will cover the structural members that are being connected.
- The members framing into the connection location cause stress concentrations.

On the new Memorial Bridge, this is avoided through the use of a "Gusset-less" truss connection, shown in **Error! Not a valid bookmark self-reference.**. This connection aims

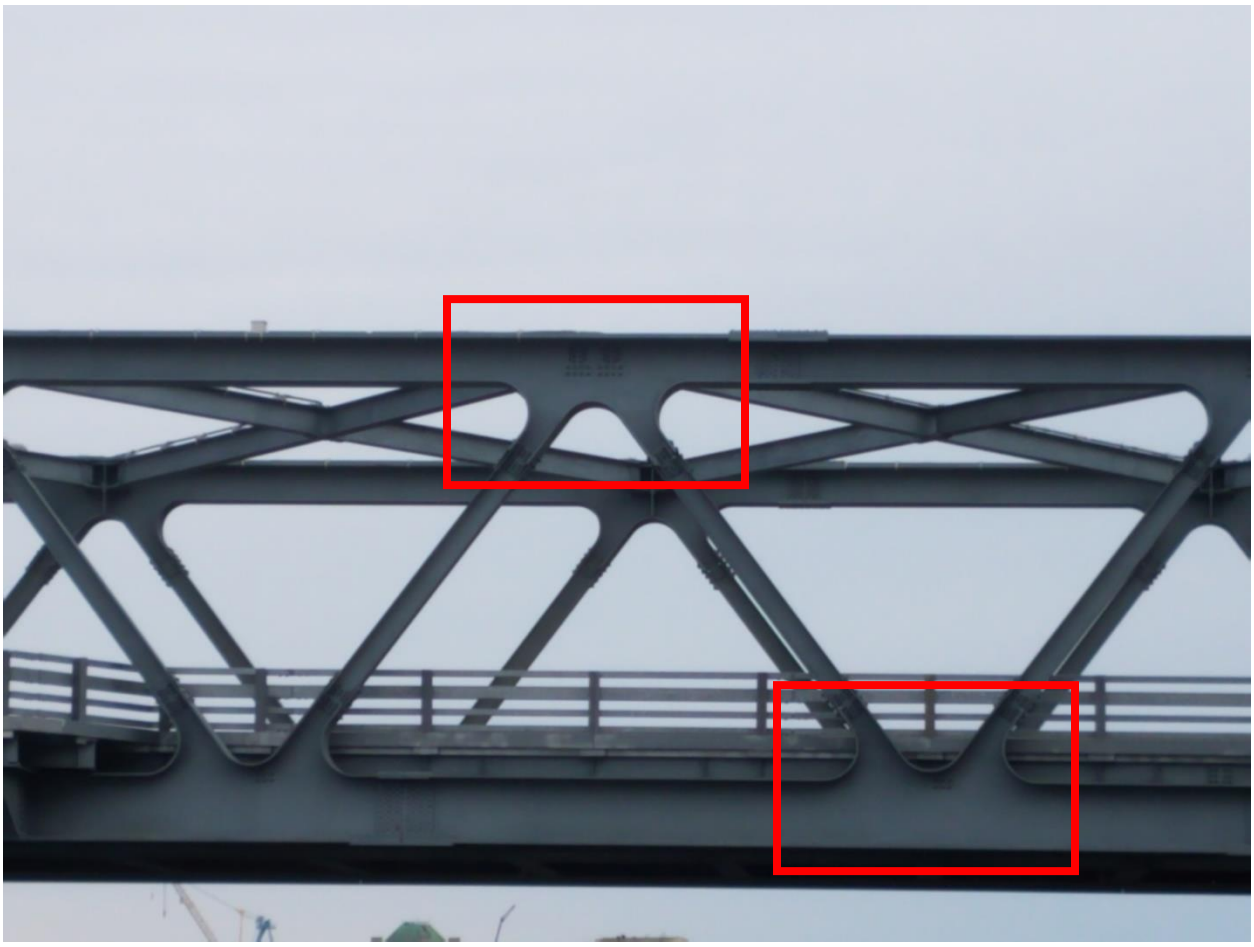

Figure 1 - Gusset-less Connections

to have a smooth transition of forces from the diagonal truss members to the top and

bottom chords of the truss system. This is accomplished using cold-bent steel flanges and a unique geometric approach. Since connections are incorporated into the chords of the bridge, the diagonals members are connected individually using bolted splice plates. Some of the main benefits of using this connection are as follows [1];

- Reduction in number of bolts needed on the bridge, compared to a traditional gusseted connection.
- The connections are much easier to inspect than a gusseted connection since nothing is shrouded behind a large plate.
- The spliced connections can be partially replaced while the bridge is under load.

Although this connection has many benefits, it has not been as widely used or studied as a traditional gusseted connection. One aim of this research is to investigate the structural performance of this connection through laboratory testing. More specifically, the aim of the overall study is to evaluate the fatigue performance of the Gusset-less truss connection. In addition to the structural performance, it is important to understand the connection and the critical locations for inspections. The overall project also intends to use the laboratory data to aid in the development of an inspection protocol for the Memorial Bridge.

1.2 Thesis Objectives and Contributions

As previously discussed, the overall objective of this research is to evaluate the fatigue performance of the Gusset-less truss connection. In this thesis, work towards the evaluation will be presented. The contribution of this thesis to the overall project is in the

form of experimental fatigue testing, which is used to evaluate the fatigue life prediction of the Gusset-less connection. Additionally, a test monitoring protocol was developed to ensure consistency across testing periods. Lastly, a work towards measuring and calculating the residual stresses in the Gusset-less test specimen was done. The layout of this thesis is presented below;

Chapter 1 – Introduction; This chapter will provide background information on the project, an overview of the objectives of this work, and a summary of relevant literature.

Chapter 2 – Laboratory Test Setup; This chapter will introduce the experimental fatigue testing, specifically the physical test setup, the loading protocol and the instrumentation plan for the fatigue test.

Chapter 3 – Fatigue Test Monitoring; This chapter will discuss the importance, and the development, of a monitoring protocol for high-cycle fatigue testing performed across multiple testing intervals.

Chapter 4 – Finite Element Monitoring; This chapter will discuss the use of finite element modeling as a tool for understanding and evaluating the fatigue test specimen and setup.

Chapter 5 – Fatigue Testing Results; This chapter will introduce the results of the fatigue testing and the implications of those results

Chapter 6 – Residual Stresses; This chapter will discuss the importance, and the measurements, of residual stresses in the fatigue test specimen.

Chapter 7 – Summary, Conclusions, and Future Work; This chapter will present an overall summary of the work, including conclusions, and future work for this project.

In addition to these chapters, this thesis includes six appendices;

- Instrumentation – Strain gauge data sheets, DIC background and additional info
- Fatigue Test Tracking – Data sheets from testing
- System ID – Additional plots from system IDs
- Additional Fatigue test results
- Residual Stress Calculations – MATLAB Code of integral method
- Residual Stress Measurements – Additional residual stress measurements

1.3 Background Information and Literature Review

In order to achieve the goals of this thesis, a literature review was needed to provide a background information on the work to be performed. In this literature review, there are five main topics investigated; instrumentation, test monitoring, finite element modeling, fatigue, and residual stress. The background information needed for this study is provided in the following section.

INSTRUMENTATION

Structural performance prediction of innovative connection details requires both advanced design tools and analysis models that are verified through experimental data. For most civil structures field or full-scale tests to failure are not feasible, therefore scale-model laboratory experiments are critical to advancing the state-of-the-art for structural

design. Scale-model laboratory experiments must be carefully designed to provide information on specific structural behaviors. In order to isolate the target behavior, all of behaviors, including influences of boundary conditions and members interactions, must be controlled and accurately accounted for in the associated structural models.

Characterization of the structural response of a laboratory experiment can be challenging depending on multiple factors including the experimental objectives, specimen geometry, available laboratory resources and infrastructure, experimental setup, and loading conditions. These factors will have a large influence on the selection of what type of measurements can be made and the method used to obtain those measurements. The typical types of measurements used to characterize a structure are the displacement, the strain, the acceleration, or any combination thereof, in the directions of interest. Obtaining these measurements is not always a trivial task depending on the experiment and the level of characterization desired. Therefore, it is important to choose the appropriate measurement method that will provide the best characterization of the system to achieve the goals of the experiments.

The measurement methods used in this study include: 2-Dimensional Digital Image Correlation (DIC), strain gauges (uniaxial and rosettes), and Linear Variable Differential Transformers (LVDTs). Each of these measurement methods are used to characterize a specific behavior in the system and create redundancy in the measurement collection.

Resistance based strain gauges have been used extensively to measure the strain response of civil engineering structures. The gauges work by forming a circuit in which there is a known electrical resistance, and as the specimen is deformed, the gauge is also deformed, and a change is resistance is measured. Based on the gauge geometry and the circuit, this change in resistance is converted to a strain measurement [2]. In a fatigue test, it is important to ensure that the gauge is not susceptible to failure due to repeated loadings [3].

LVDTs have also been used extensively [4] to measure the displacement response of civil engineering structures. The LVDTs work by associating the position of the LVDT core with a signal value. As the position of the core changes, the magnitude and sign of the signal changes, allowing the LVDT to measure the magnitude and direction of the displaced core [5].

Finally, 2-D DIC has also been used frequently and has been gaining popularity as imaging technology has advanced. Generally, in a civil engineering application, DIC is used to measure full-field surface displacements and strains. This is accomplished by identifying and tracking the movement of groups of pixels, through a series of digital images, captured via a speckle pattern on the area of interest. Using a correlation algorithm, as the specimen is deformed, the translation vectors for each pixel grouping are calculated and the movement is computed relative to the location of the pixel groupings of an undeformed reference image [6].

TEST MONITORING

The instrumentation generally serves the purpose of measuring the structural response of the test specimen, but in specialized testing fixtures, it is important to understand the behavior and influence of the different components of the entire test setup. Since the consistency, reliability, and performance of the experiment are vital, it is important to monitor the response to ensure the behavior is as expected using a systematic approach. Research has been performed on characterization of structural systems and the interaction between experimental and numerical models considering field conditions and errors [7-9].

FINITE ELEMENT MODEL

In civil engineering applications, finite element models (FEMs) are often used as an analytical tool to aid in design as well as the analysis of local and global behavior of engineering structures. The key to using a FEM as a tool in engineering is understanding the assumptions that go into the analysis being performed and being able to distinguish between a good estimation and a bad estimation of reality in terms of results. This requires experience and engineering judgement when creating the FEM as well as interpreting the results.

Often finite element modeling is an iterative process in which models are created and refined until reasonable results are obtained. Within these iterations adjustments are made in the form of element type, element geometry, load applications and boundary conditions, to name a few. One of the most common sources of variation in FEM results

is the mesh used, in terms of geometry and type [10]. In most software, there are a wide variety of element types to choose from depending on the model geometry. Some of the common elements used are beam elements (1-D), quadrilateral or triangular (2-D), and tetrahedral or hexahedral (3-D) [11]. In addition to the element-type, the size of the elements is of great importance. Many previous research studies [10, 12, 13] have shown that the size of the elements have a large impact on the accuracy and resolution of the analysis. Unfortunately, as the element size decreases, more elements are required for a model of the same size, and with more elements the computations become much more time consuming. For this reason, it is important to refine a mesh, typically through a sensitivity analysis, until any further changes in mesh size do not greatly influence the results. The ideal mesh will minimize computation time while maximizing the accuracy in the model. As previously mentioned, the acceptance of the model is dependent on experience and engineering judgement, so great care must be taken to ensure that the model is representative of reality.

FATIGUE

Fatigue, in terms of engineering materials, is the degradation of material due to repeated loading and unloading. The cyclic loading causes cumulative damage in the material which causes microscopic cracks to form and propagate. Fatigue failures occur when these microscopic cracks reach a critical size and then they propagate very quickly [14]. The fatigue life of a structural component is defined as the number of cycles, with an applied stress range, before the crack reaches this critical size.

In most cases fatigue can be categorized as high-cycle or low-cycle fatigue. High-cycle fatigue is characterized by a low applied stress range and results in a high number of load cycles to failure, typically greater than 10^5 cycles [15]. Low-cycle fatigue is the opposite, with a high applied stress range which results in a low number of load cycles to failure [14]. This relationship between cycles to failure and the applied stress range is typically documented in terms of an S-N curve [14]. The S-N curves use a log-log scale with the y-axis showing the applied stress range and the x-axis showing the expected cycles to failure. A sample S-N curve for welded steel fatigue details is shown in Figure 2 [16]. As the figure shows, there are two distinct portions of an S-N curve. The first portion shows the relationship between the applied stress and the expected cycles to failure, but at a certain threshold the slope flattens, and the cycles to failure increase indefinitely. This threshold is commonly referred to as the endurance limit and it signifies the maximum applied stress range at which fatigue failure would not occur. This means that any applied stress equal to or lower than the endurance limit will not result in any fatigue damage [14]. These relationships are derived experimentally with many inputs such as material, geometry, and loading conditions. These inputs are the most influential factors in terms of fatigue performance and for this reason, S-N curves exist for many different materials and geometries.

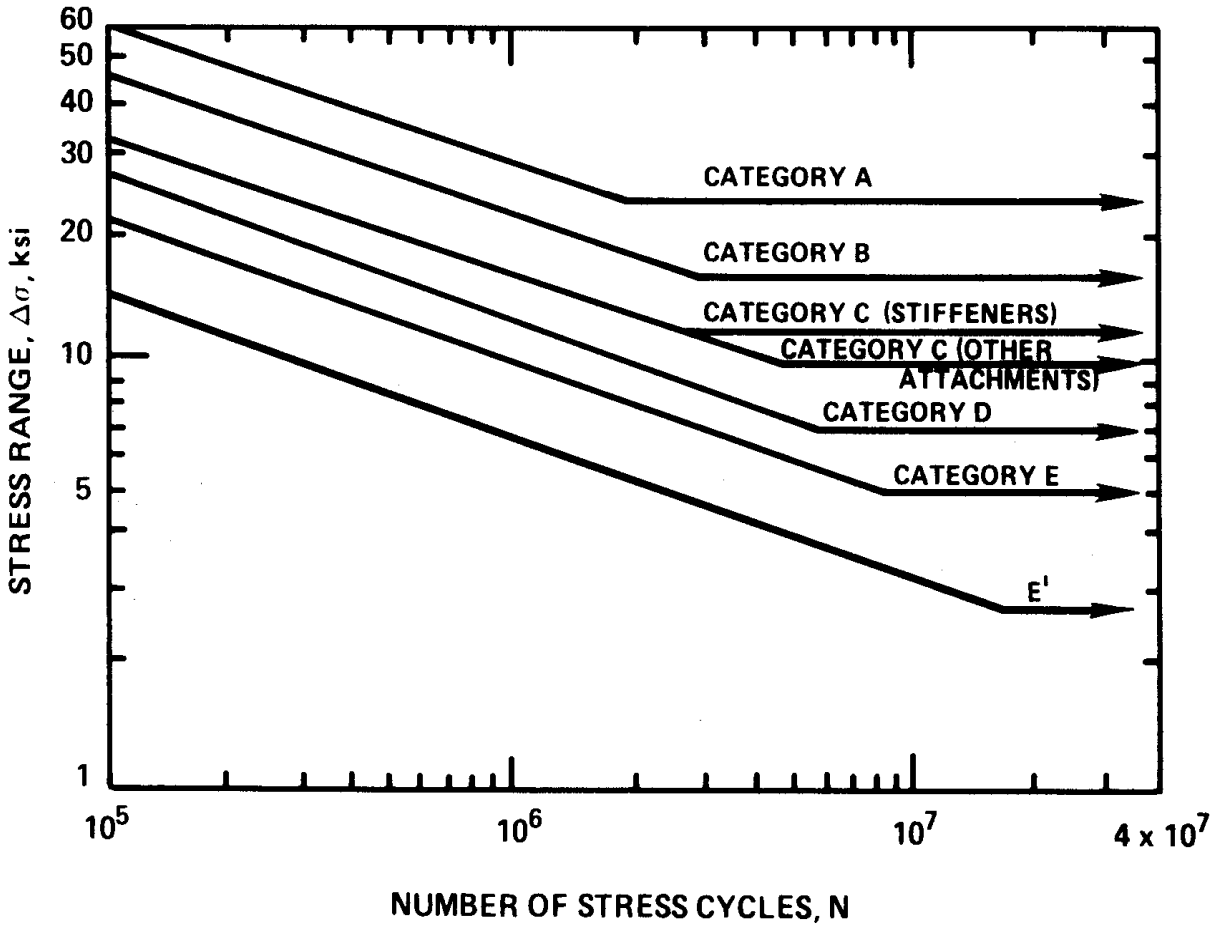

Figure 2 - Welded Steel S-N Curves [16]

The fatigue performance of welded structures has been studied extensively [17-19]. From these previous studies typical welded steel details have been categorized according to loading and geometry, and the S-N curves have been developed to characterize the fatigue performance. Figure 3 is a schematic defining the fatigue categories shown based on the geometry and loading [19]. Some of the important things to note about these experimentally derived relationships are that the test was performed in the stress measured was the nominal stress, the loading was a fully-reversed loading,

and the residual stresses were not measured, but were assumed to be the same for each weld configuration [20].

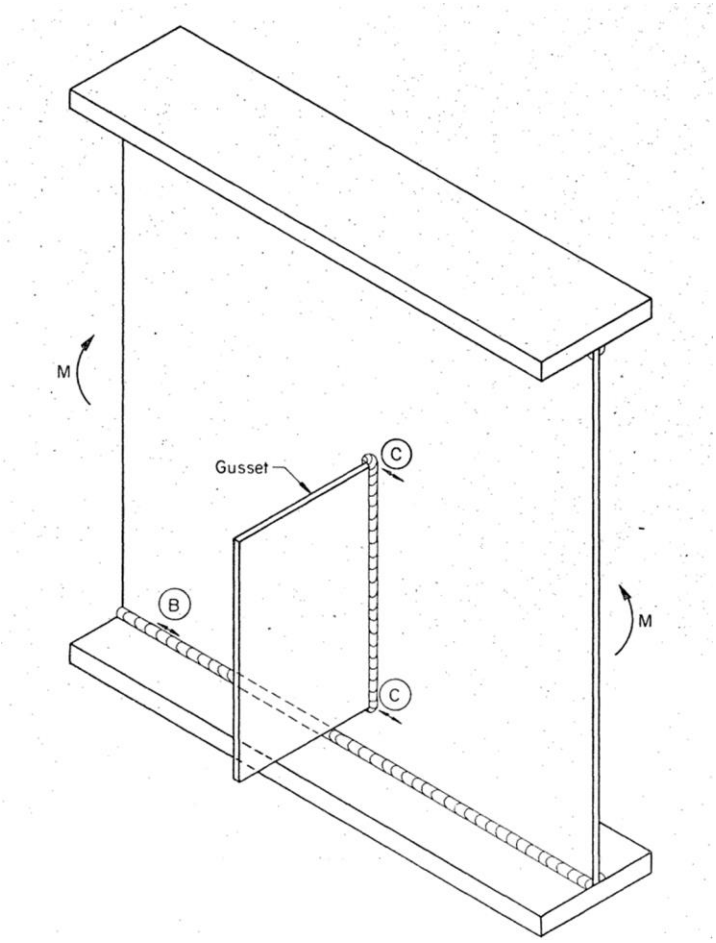

Figure 3 - Sample Fatigue Categories [19]

Nominal stress refers to the stress at some distance from the weld, but that distance is not explicitly defined. This stress is essentially the stress close to the weld without any effect from local concentrations due to the weld geometry or a notch [21]. Another approach that can be used is the structural stress, or hot-spot stress. This is a method in which stresses are measured close to the weld and extrapolated to incorporate the stress concentration effect of the weld geometry [21].

In terms of loading there are a few variables which have a large impact on the fatigue performance. The most influential factor is the applied stress range, in which the higher the applied stress ranges the lower the expected cycles to failure. Another important variable that has more of a secondary effect is the mean applied stress. Generally, there are two common loading scenarios for a fatigue test; a fully-reversed loading or a pulsating-tensile loading. The fully-reversed case is when the cyclic stress range is centered about zero stress, meaning that the specimen experiences an equal magnitude of compressive and tensile stresses. The pulsating-tensile loading is when the cyclic stress range is limited to tensile stress only, meaning that the mean stress is tensile, and the specimen is never loaded in compression. The effect of mean-stress has been studied extensively [22-25], to summarize, a tensile mean-stress is detrimental to fatigue performance and a compressive mean-stress is beneficial. The theoretical relationship is shown graphically in Figure 4 [26], where Sm is the mean stress. Methods have been

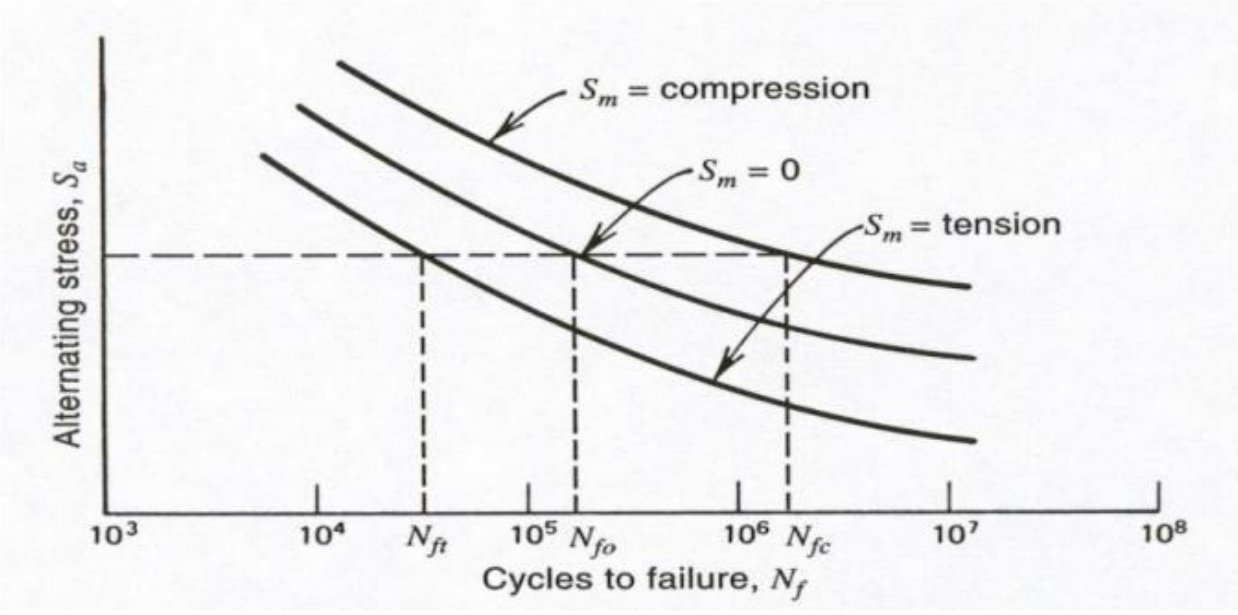

Figure 4 - Mean-Stress Effect [26]

developed to convert the different types of tests to the fully reversed case in order to compare the results to the standardized S-N curves. The most commonly used relationship is the Goodman line shown in Figure 5 [27]. This line uses a combination of

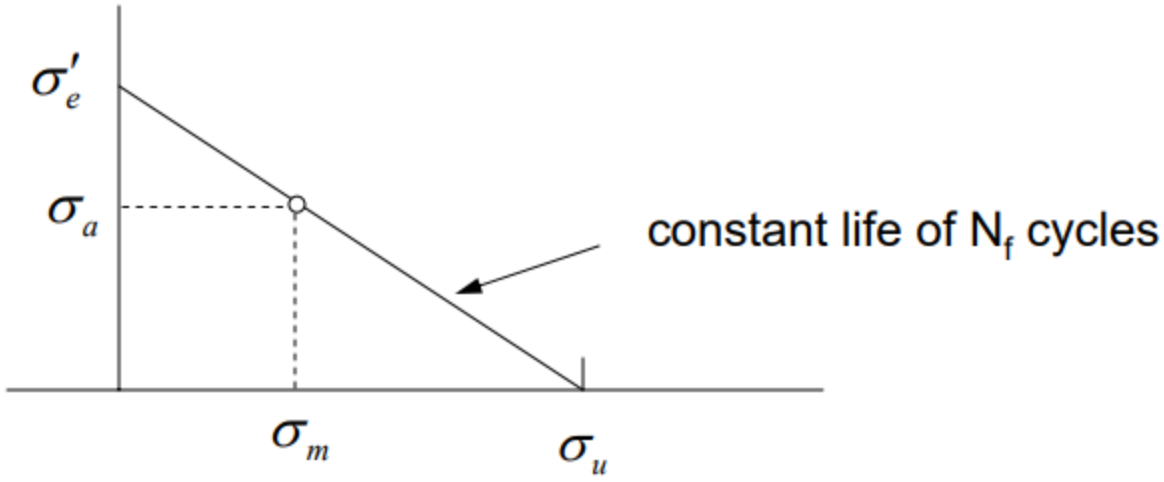

Figure 5 - Goodman Line [27]

alternating stress (σ_a), along the y-axis, and mean-stress (σ_m,) along the x-axis to identify an equivalent alternating stress (s'_e) that would provide the same fatigue life, in terms of cycles, when the mean stress is zero.

In addition to the mean-stress effect, the residual stress state of the specimen will have a secondary effect on the fatigue performance. The behavior is similar to the mean-stress effect where tensile stresses are detrimental and compressive stresses are beneficial to fatigue performance [28]. Often times the residual stresses are not accounted for in civil engineering applications.

RESIDUAL STRESS

Residual stresses are stresses that are created from manufacturing or fabrication processes and remain in the material even after any external loads are removed [29]. Some examples of the most common sources of residual stresses are welding, cold-bending, and hot-rolling. These stresses are often overlooked due to their complexity and the difficulties in measuring them reliably, but the effect of this initial stress state can be critical in terms of structural performance, in terms of material strength, fatigue performance, or even stability [29].

In terms of measurement methods, there are a variety of different methods, each with their own limitations and applications. Generally, the methods are categorized into relaxation measurement methods and diffraction methods. Relaxation methods rely on the relationship of the deformations caused from releasing the residual stresses present in a specimen through cutting, drilling, or other material removal methods [29]. Since material is being removed, relaxation methods are categorized into destructive methods, and semi-destructive methods. Destructive methods, as the name suggests, are methods in which the specimen to be evaluated must be significantly damaged, often to a point where the specimen no longer be used, while semi-destructive methods are methods in which the damage is tolerable or is insignificant to the performance of the specimen. Diffraction methods are often also referred to as non-destructive methods because no damage is induced through the measurement method.

Of all the available methods, the most common, and often the most convenient, is the hole-drilling method. The hole-drilling method consists of drilling a hole on the surface of a specimen and measuring the deformation of the materials around the drilled hole [29]. These local deformations can be captured with a variety of methods, but the most common is using a specialized strain rosette. Using this method, which has been standardized in ASTM E837-13a, it is possible to determine the residual stresses through the depth of the test specimen. The main limitations of this method are as follows;

- The method relies on an assumption of material linearity. It is said that the method is quantitative up to 70% of the yield stress of the material, beyond that the results are only qualitative [30].
- The depth of measurement is dictated by the rosette geometry and is typically limited to approximately 2mm.

The hole-drilling method used in this study will be discussed in further detail in section 6.2.

2 LABORATORY TEST SETUP

This chapter will briefly discuss the design of the scale gusset-less truss connection fatigue specimen, with the limitation of the structural laboratory as a main design constraint, which was part of a previous thesis [31]. Additionally, the laboratory fatigue test setup will be described in detail in its original state, which was part of a previous thesis [31]. The test setup in its current state will be presented with a discussion of the adjustments made to the setup. The laboratory setup will also introduce and explain the fatigue loading protocol. Lastly, the instrumentation of the specimen and test setup will be discussed.

2.1 Specimen Design

The gusset-less truss connection, Figure 6, used in place of typical gusseted connection on the previously mentioned Memorial Bridge, has a unique geometry which incorporates prominent bends in the steel to create a transition from the chord to the

Figure 6 - Memorial Bridge, Top-Chord Gusset-less Connection

diagonals. In addition to this, the connection has large, multiple-pass welds connecting the flanges to the web. In the design of this connection, the critical fatigue location was identified as the curved weld of the gusset-less connection on the bottom chord of the bridge. Additionally, this area was assumed by the designer to be a category C weld fatigue detail. A structural Finite Element Model (FEM) was created during the design to estimate the distribution of stresses through the gusset-less connection, in the critical location, based on the fatigue loading of the bridge [1]. The output of that model, Figure 7, was also used as a comparison point for the design of the scaled gusset-less fatigue specimen.

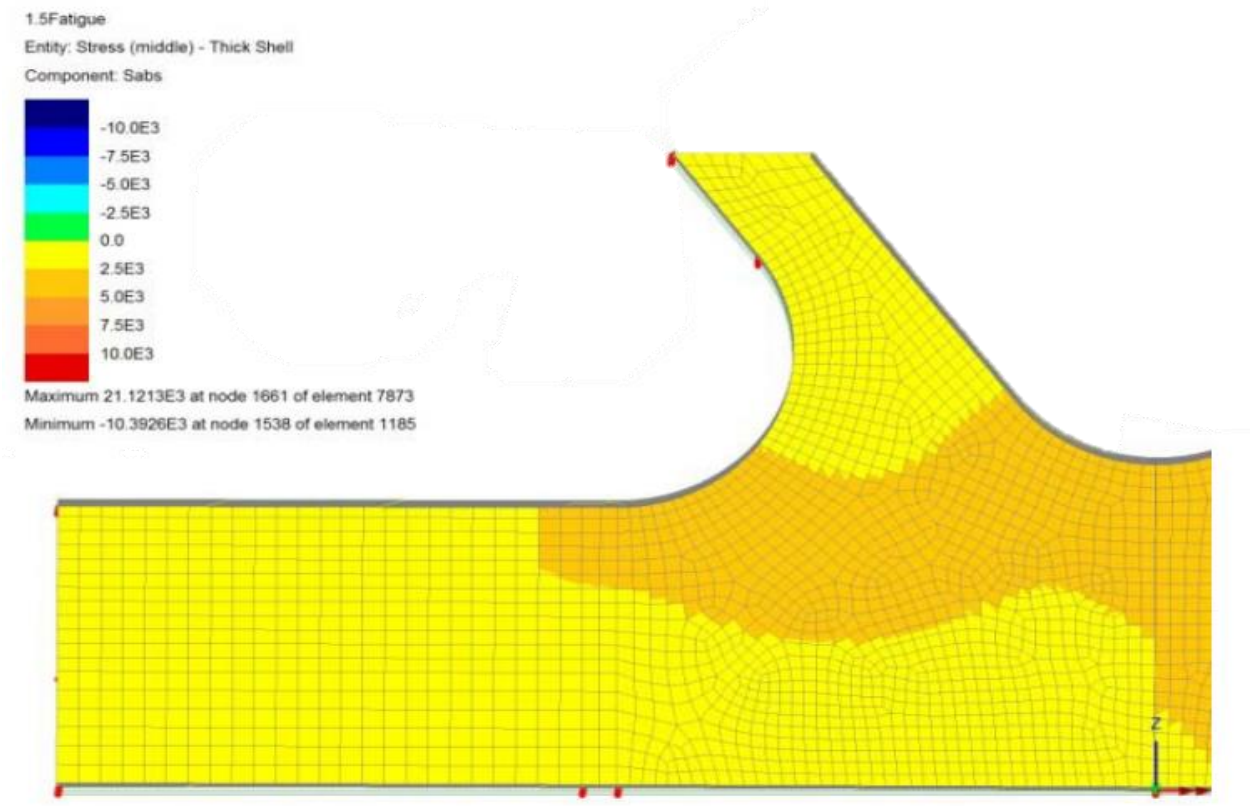

Figure 7 - HNTB Design Stress Contour [1]

The design of the fatigue test specimen [31] revolved around three main factors;

1. Capturing and replicating the structural behavior of the in-place connection, present at the bridge.
2. Replicating the same fabrication process, specifically regarding the weld size and number of passes, as well as the cold-bending of the top flanges.
3. Scaling the connection in a way that would allow for a representative test to be conducted with the equipment limitation of the UNH Structural Engineering Laboratory.

Based on these design goals, the limitations of the structural laboratory were identified as the primary constraint for this scaled connection. The main limitation was the lack of infrastructure designed to carry lateral forces, which will be discussed when the fatigue test setup is introduced. The supports required for the fatigue test played a large role in the geometric constraints of the specimen. For this specimen design, similitude scaling was used to determine the geometry and loading. The primary design check was a comparison to the design stress contours from HNTB. For this check, several numerical models of different geometries and loading configurations were used to check the stress contours and general behavior of the specimen. The progression of the geometric cutbacks is shown in Figure 8 [31].

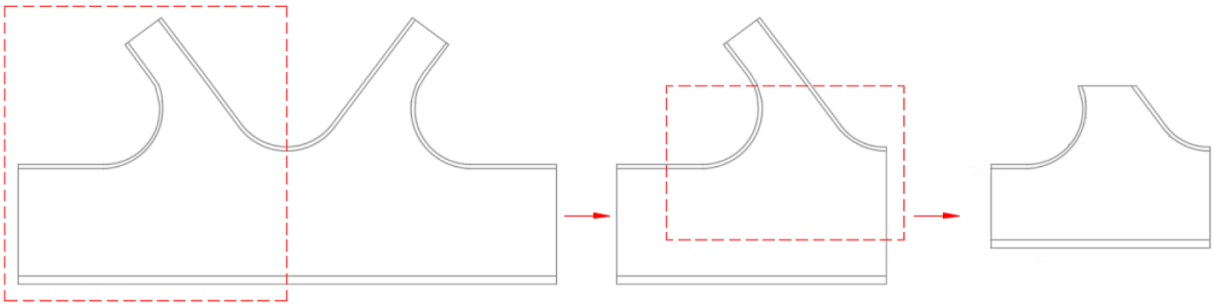

Figure 8 - Geometric Reductions of Scaled Connection [30]

The final scale factor used was 1:1.62 in terms of geometric scaling signifying that the geometry of the specimen is approximately 62% of the actual connection [31]. The final geometry and relevant material properties used are shown in Figure 9. Note that two vertical plates are bounding either side of the test specimen in order to mount it to the actuator and support respectively. Lastly, the specimen was fabricated by Canam-Bridges, the steel fabricator for the Memorial Bridge. This ensured that the fabrication procedures used to produce this specimen were the same as those used in the actual fabrication of the Memorial Bridge.

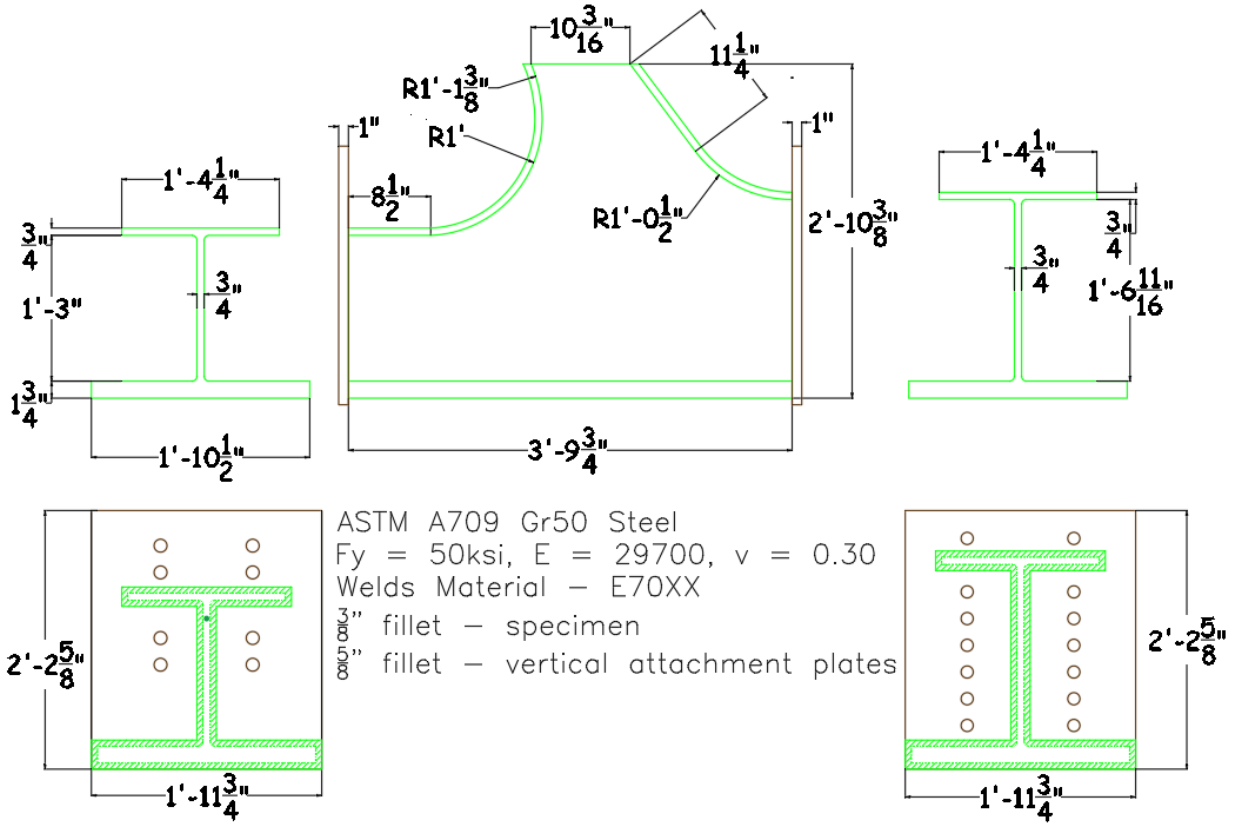

Figure 9 - Specimen Dimensions and Material Properties

In terms of the load application, it was decided to apply the load axially with a vertical offset from the centroid. This decision was made to ensure a loading was applied to the specimen that was representative of the bottom-chord of the Memorial bridge [1], based on the design calculations, which has an axial load and a moment applied. More importantly, this loading was found to result in a similar stress contour to that of the design even without the diagonal contributing to the loading of the specimen.

2.2 Fatigue Test Setup

The UNH Structural Laboratory has a variety of testing capabilities but for this unique, large-scale, fatigue test some additional infrastructure was needed. As

previously mentioned, the main constraint of the laboratory is the lack of infrastructure capable of handling lateral forces. The main system for mounting equipment in the structural laboratory is the "Strong-floor" system, which was designed for pull-out forces. Therefore, in addition to the specimen design, an initial design for the fatigue test setup was produced [31]. The design goals for the test setup were the following;

- The ability to mount and support the fatigue rated hydraulic actuator, at multiple heights.
- The ability to support the gusset-less fatigue specimen.
- Provide a transfer of the reactionary forces from the fatigue loading into the "Strong-floor" system.

The support system design consisted of two parts; (1) the "Reaction Block", and (2) the support "Bracket". The original reaction block was made up of a horizontal steel base plate with 8 bolt holes for floor anchors, two vertical steel plates with 16 bolt holes for the actuator attachment rods, four steel kickers, and 16 steel tubes. All the individual components were welded together as seen in Figure 10.

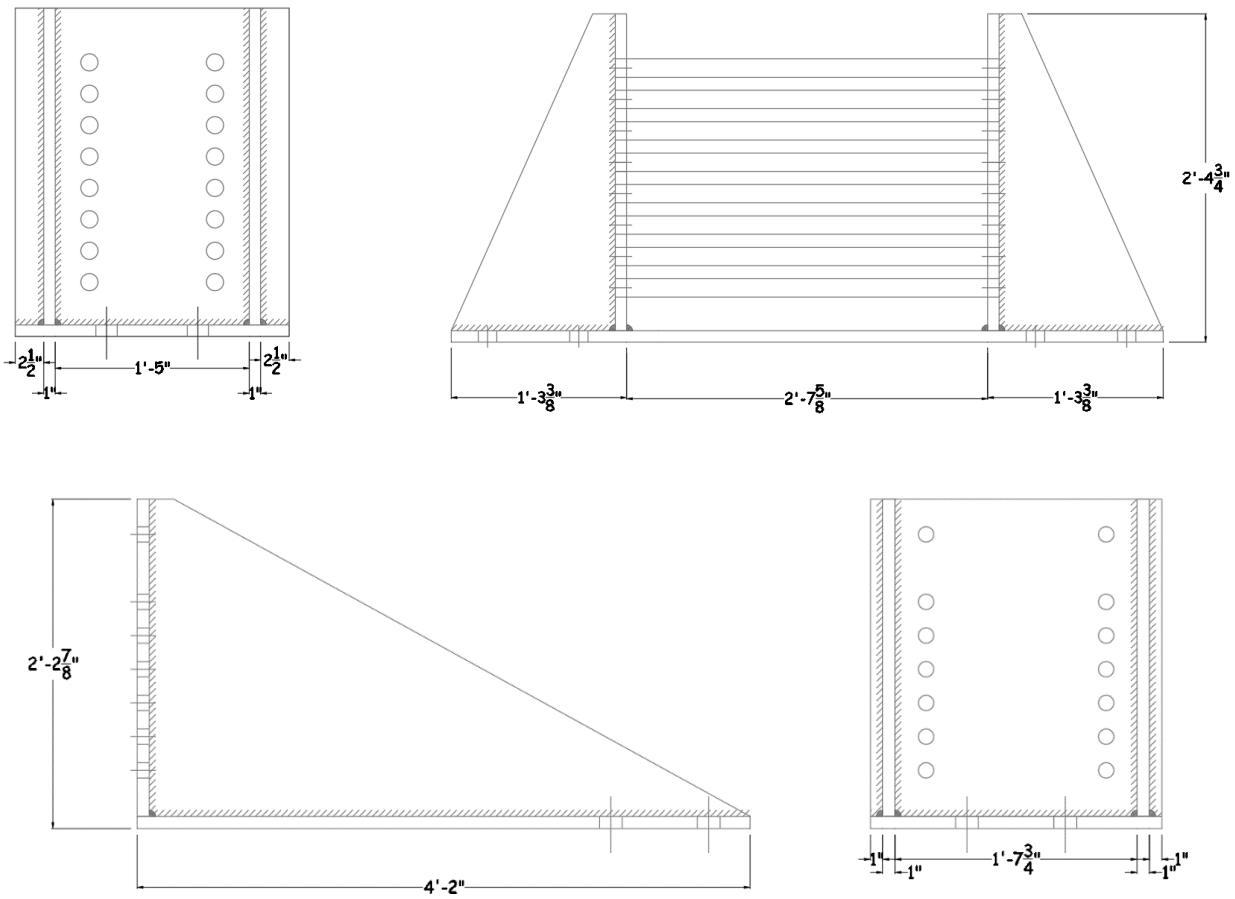

Figure 10 - (1) Reaction Block (top), (2) Support Bracket (bottom)

The steel tubes were in place to provide means for the actuator attachment rods to pass through the reaction block if concrete was cast between the two vertical steel plates, which was considered in the preliminary design. The support bracket is made up of a horizontal steel base plate with four bolt holes for floor anchors, a vertical steel plate with 14 bolt holes for specimen attachment bolts, and two steel kickers to provide stiffness to the vertical plate.

Once the test setup was fabricated, the supports were positioned in their appropriate locations based on the Strong-Floor anchor pattern and bolted in place. With the supports in position the actuator was lifted into position and attached to the reaction block using high-strength threaded steel rods with nuts torqued to 1400 ft-lb. Finally, the specimen was bolted, to a specified 800 ft-lb of torque, into the test setup. After installation of the supports and test specimen, some initial static load tests were performed to identify the behavior of the system. Specifically, the strain in the area of interest and at the boundary conditions, as well as the displacements in key locations along the test setup were investigated, which will be discussed in detail in section 3.2. These measurements led to four key observations made about the test setup in its initial state;

1. There was significant support motion in both the reaction block and the support bracket, causing undesirable actuator motion.
2. The vertical plate connecting the specimen and the actuator, also referred to as the specimen tip, was displacing significantly in the vertical direction.
3. The specimen tip was rotating significantly out of plane about the horizontal loading axis.
4. There was a high strain reading (2000 $\mu\epsilon$) in the vertical direction on the vertical plate connecting the specimen and the actuator.

Based on these observations, some modifications to the test setup were needed in order to further control the behavior of the test setup. Specifically, the modifications are

intended to ensure the desired loading was applied to the fatigue specimen while protecting the hydraulic actuator from undesirable side loading [32].

The first modification was creating a new boundary condition at the specimen tip, hereby referred to as the "shim support", in order to restrain the vertical displacement as well as the rotation of the test specimen. This was accomplished using multiple steel shims, shown in Figure 11, wedged under the tip of the specimen at two locations, on either side of the specimen tip. This support acts as a roller in the plane of loading because the steel shims can slide against each other while restricting motion in the vertical direction. It should be noted that this only restrains the vertical motion while applying a tensile load, which causes the specimen to displace downward. Due to the discretization of the shims, at either ends of the specimen tip, the rotation about the plane of loading is also restrained. In addition to the shims at the tip of the specimen, shims were added under the reaction block and bracket to increase the contact with the floor and decrease rotations at the supports.

Figure 11 - Location of Shim Support at Specimen Tip

The other major modification was the addition of concrete between the two vertical plates of the reaction block to increase the overall stiffness. Specifically, the rotation of the base plate of the reaction block caused significant rotation of the vertical plate where the actuator is connected to the reaction block. This rotation was due to the portion of the base plate between the two vertical plates being essentially unrestrained. This was identified as the source of the undesirable actuator motion. Figure 12 shows the

added reinforcement in the reaction block (a) and the reaction block with the additional concrete (b).

Figure 12 - Reaction Block Reinforcement (a), Reaction Block with Concrete

The final modification was the change in actuator position to prevent a stress concentration on the vertical plate attaching the specimen to the actuator. During installation, it was noted that the vertical plate had a significant bend, most likely due to the welding process. When the actuator was in it's original, highest, position and the bolts were tightened, this bend was removed due to the force from the bolts. The straightening of this plate caused the strain in the plate close to the weld to exceed the yield strain of the material, creating a point in the test setup that would be prone to fatigue damage to the magnitude of the strain applied. Since this location was not the area of interest, it was decided to lower the actuator to the next position, which resulted in a significant reduction in the strain at the location.

With the modifications to the test setup made, additional tests were performed, and the structural response was measured and found to be acceptable. The test setup in its final state is shown in Figure 13. This configuration consists of the reaction block, the actuator, the fatigue specimen, the shim support, and the bracket.

Figure 13 - System Components - Overall Test Setup, Reaction Block (a), Bracket Support (b), Specimen (c), and Shim Support (d)

In addition to the physical test setup, a loading protocol was also developed for this test. The loading protocol can be divided into three main sections;

1. The pre-cyclic loading
2. The cyclic fatigue loading
3. The post-cyclic loading

The loading protocol is applied using MTS Multi-Purpose Testware software to apply either loads or displacements to the MTS 244.41 hydraulic actuator. In this specific loading protocol, the commands are given in terms of force measured on the load cell, a device to measure the force applied, of the actuator. The loading procedures were coded in the MPT Procedure Editor in the form of force commands.

The pre-cyclic loading consists of two ramp functions in which the load is brought from 0 Kip to 40 Kip in 10 seconds, then from 40 Kip to 20 Kip in 5 seconds and occurs before the cyclic fatigue loading. The purpose of this ramp loading is to create some unique peaks in the measured response that will be used to synchronize the data sets from different measurement methods. The post-cyclic loading consists of three ramp functions in which the load is brought to 40 Kip in 7.5 seconds, then 60 Kip in 5 seconds, and finally 0 Kip in 7.5 seconds. The post-cyclic loading occurs after the cyclic fatigue loading and serves as a second point of synchronization for the post-processing.

The cyclic fatigue loading, which is implemented after the pre-cyclic loading and before the post-cyclic loading, that is being used in this test is a pulsating tensile loading,

in which, the actuator is cycling in force control as a sinusoidal signal in tension. The loading specifications are as follows:

- Mean axial load applied: 55 Kip
- Cyclic amplitude: ±50 Kip
- Cyclic frequency: 3.5 Hz
- Applied function: Sine wave
- Cycles per Test Session: Varies.

The level of loading was limited by the capacity of the actuator load cell, which is 110 Kip, while maximizing the applied tensile stress range, this was decided to increase the chances of fatigue failure. With this level of loading, the endurance limit of a category C fatigue detail, which was the design assumption, would be exceeded according to the numerical models. The pulsating tensile loading is used to be representative of the conditions on the Memorial Bridge, where the bottom-chord will be in tension under the

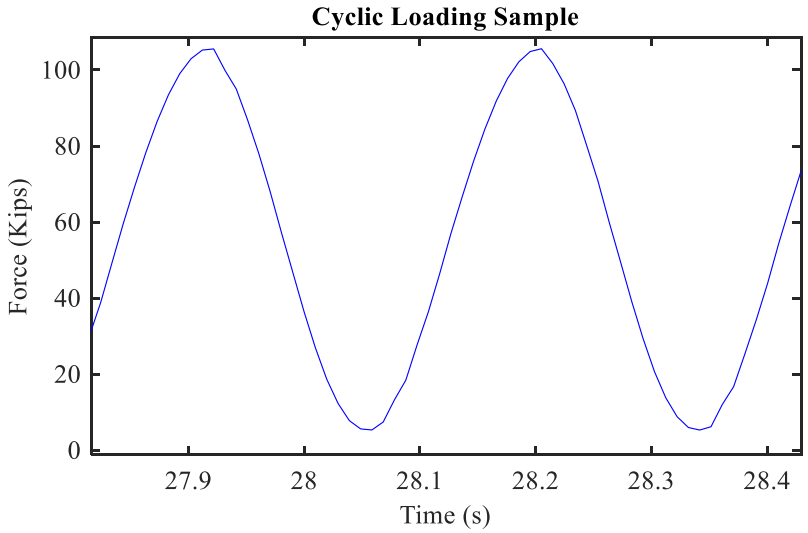

Figure 14 - Cyclic Loading Sample

service loads. It is also important to note that the test was performed in ambient temperature (xx degrees) in a controlled lab environment. The frequency of loading was limited to ensure the test was performed in a "quasi-static" loading [31]. A sample of the cyclic loading is shown in Figure 14, and a sample of the overall loading protocol is provided graphically in Figure 15 below. Figure 16 shows a schematic of the loading.

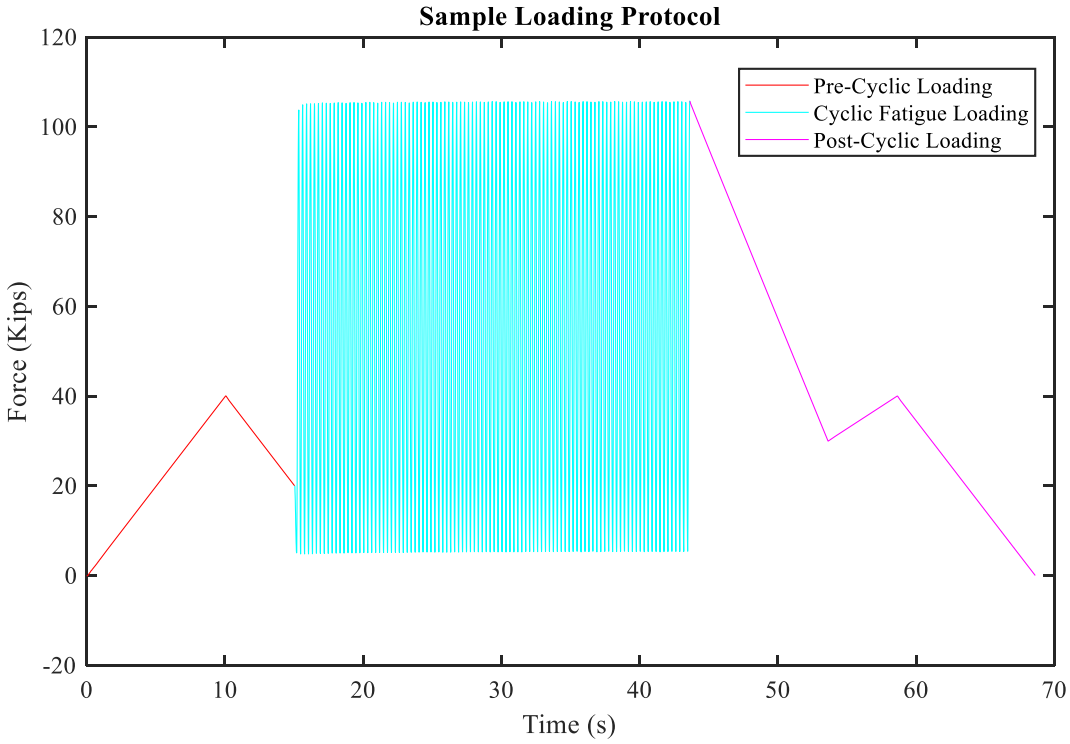

Figure 15 - Sample Loading Protocol

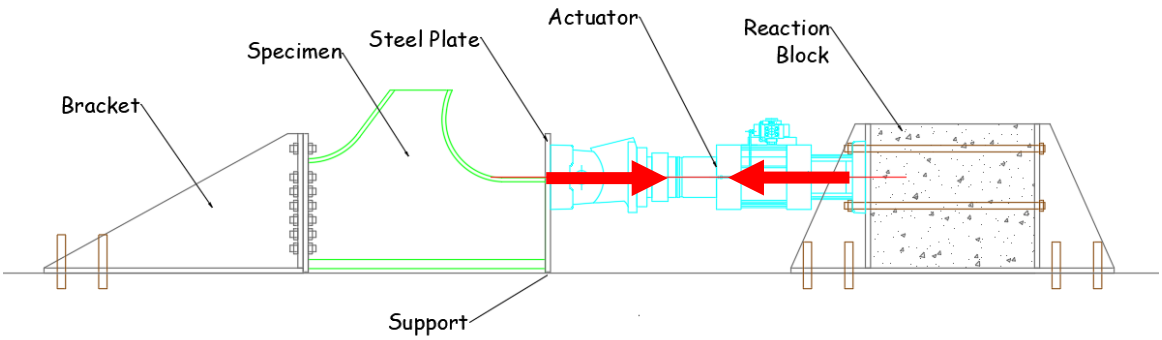

Figure 16 - Loading Schematic

In addition to the development of the loading procedures, the tuning parameters as well as the limits for the actuator were selected. The tuning of the actuator refers to adjusting the inputs, in terms of a proportional-integral-derivative (PID) control loop. The specific methods for tuning this control loop were obtained from the MTS user manual [33]. The goal of tuning the actuator controls was to ensure that the command being input, in terms of force and frequency, matched the actual measured output of the actuator. Additionally, with a poorly tuned actuator, especially when using force-controlled testing, the system is susceptible to instability in which the measured force can rapidly deviate from the command in terms of magnitude and frequency. This is one of the main reasons for the limits being implemented. The limits refer to an upper and lower force limit that, if the actuator load cell reading exceeds, will interlock the hydraulics and stop pressure from reaching the actuator. The upper limit, set to approximately 107 Kip, is in place to prevent the actuator load cell from reaching the 110 Kip limit, while the lower limit, set to approximately -2 Kip (compression), is in place to prevent the specimen from being loaded in compression. Therefore, in the case of instability, the limits will be exceeded, and the hydraulics will quickly cease pressure to the actuator.

2.3 Instrumentation

The objectives of the experiment must be considered prior to determining the location and type of sensors. Each sensor should provide a needed piece of information to fulfill these objectives. For this experiment, the bridge owner was interested in (1) investigating the design assumption of fatigue category C [20] for the gusset-less truss connection, which implies infinite-fatigue life under service conditions, and (2) collecting data useful for providing guidance for fatigue-focused visual inspection procedures of the gusset-less connection through the service life of the bridge. An additional interest of the research was verifying the structural model of the gusset-less connection and evaluating the dissipation of strain with distance from the weld toe. In order to accomplish these goals, the experimental set up, including boundary condition and component interface, must be categorized and fully understood for both fatigue assessment and structural model verification.

The measurements techniques and sensors that are utilized for the scale model laboratory fatigue experiment are Digital Image Correlation (DIC), Linear Variable Differential Transformers (LVDTs), and strain gauges (uniaxial and rosettes), which are used to measure displacements, rotations and strains. The instrumentation used can broadly be categorized as contact (LVDTs and strain gauges) and non-contact (DIC) measurements.

Strain gauges and LVDTs are two of the most traditional contact tools for obtaining structural response measurements. These sensors function by maintaining contact with

the specimen, through contact in the case of the LVDT, or bonding (epoxy or spot-weld), in the case of the strain gauge. These tools tend to be the most commonly used due to their cost, availability, reliability, and accuracy of structural response measurements. Although strain gauges are the most frequently used sensors, there are some significant drawbacks and limitations to their use and applicability. One of the most significant drawbacks for the strain gauges is the installation procedure, which generally consists of the following:

1. Surface preparation consisting of abrasion (sanding or grinding) followed by a thorough cleaning of the surface to remove particles and oils which could weaken the adhesive bond.
2. Positioning of the gauge to define the measurement direction(s).
3. Application of accelerant to prepare the gauge for adhesion.
4. Application of adhesive and bonding of the gauge.
5. Positioning of the lead wires and soldering if necessary.
6. Connection to strain measuring device and data recording.

Strain gauges are limited to relatively smooth and preferably flat surfaces that allow complete bonding of the gauge to the specimen. Additionally, the locations that the strain gauges and LVDTs can be installed is limited to locations that can be physically accessible with sufficient space to perform all the steps necessary for installation.

Another major drawback to these contact measurements is the amount of surface preparation required for adequate installation. Not only is surface preparation a

significant amount of work but it also has the potential to interact and affect the specimen behavior. Specifically, if there is any coating or outer layer of environmental protection on a specimen, the surface preparation requires coating removal, while this is not an issue for laboratory specimens exposed to indoor environmental conditions, it can adversely impact field application. Further, strain gauges and LVDTs only provide discrete measurements at the point of installation. Often times, the amount of measurements needed to fully characterize the response of a specimen is significant. To capture all the required measurements, many sensors are necessary, which is costly in terms of number of sensors and installation time. To a lesser extent, the size of these sensors may also provide important limitations, especially when localized strain measurements are needed very close to one another.

The DIC measurements fall under the non-contact measurements category since contact is not present between the cameras and the specimen. DIC identifies and tracks the movement of groups of pixels captured via a speckle pattern on the area of interest. Using a correlation algorithm, the translation vectors for each pixel grouping are calculated and the movement is computed relative to the location of the pixel groupings of an undeformed reference image. A mathematical background of the DIC analysis method is provided in Appendix A. Although DIC is not as widely used as the traditional measurement methods, it is becoming more popular as digital image technology advances become more cost-effective and the post-processing technology improves. DIC measurements, while not being as consistently accurate as traditional methods, given the

impact of image collection conditions and camera capability, excels in many other aspects. One of the largest benefits of DIC compared to other forms of instrumentation is its ease of installation. DIC requires very little installation time depending on the type of equipment used and the environment where the measurements are collected. The general installation procedure is as follows:

1. Application of a suitable tracking pattern to the measurement area of intertest. Typically, this is done with a black on white speckle pattern or the inverse.
2. Placement of camera(s) to focus on the measurement area. If 2-D DIC is being used, the cameras need to be perpendicular to the area of interest. When 3-D DIC is being used, a minimum of two cameras will be in a stereo configuration, typically at an angle of 30 degrees with respect to each other.
3. Adjustment of camera(s) settings to optimize focus, lighting, and resolution. These parameters should be optimized uniquely for the test setup and the hardware used.
4. Image capturing. Typically, a commercial program is used to control the capture settings/timings, especially in the case of 3-D DIC in order to synchronize the multiple cameras.

An experienced user can record measurements with DIC in a relatively short time without difficulty. The other major benefit is that the DIC measurements can be used to characterize a large area where applying multiple gauges would not be feasible. With the correct setup and equipment, it is possible to obtain a full-field characterization of the

area of interest. One major drawback for the DIC is the computational effort is much more significant compared to the strain gauges and LVDTs. This is due to the differences in data, with the strain gauges and LVDTs it is a direct measurement and there is no post-processing needed, but with DIC it is indirect in that it is converting pixel movements into displacements and strains mathematically. Lastly, the initial cost of the DIC equipment can be high, but it is a tool that can be reused and applied to a variety of situations, which has the potential to mitigate long-term costs.

The strain gauge instrumentation plan for the specimen is shown in Figure 17. The naming convention for the gauges are as follows;

- Specimen side; N = on the North face of the specimen, S = on the South face of the specimen, VP = on the vertical plate of the specimen.
- Type; R = Rosette type strain gauge, U = Uniaxial type strain gauge.
- Location; W = web of specimen. FB = Flange (bottom-side). FT = Flange (top-side).
- Number; the number corresponding to specific gauge of a specific type.
- Example; NRW1 = Rosette number one on the North face of the specimen web

In this study, a total of 12 strain rosettes and 10 uniaxial strain gauges are being used to characterize the strains throughout the specimen. The uniaxial strain gauges used were CEA-06-125UW-120 gauges while the rosettes used were EA-XX-125BZ-350, all of which were wired in a quarter bridge configuration [2]. The device used to connect the strain gauges to a data acquisition computer was the NI cDAQ™-9178 chassis with NI

9219 Universal Analog Input Modules, and the data acquisition software was LabVIEW 2017. The capture frequency chosen for all strain gauges was 60Hz, which was sufficient enough to characterize the response given the input frequency, while maintaining a reasonable sized data set from each testing period. The strains were chosen to be recorded continuously throughout the entire loading protocol, as opposed to incrementally, to ensure that if there was a change in behavior, it would be captured through the strain measurements. Lastly, it is important to note that the strain gauges were calibrated, or zeroed, while the specimen was not attached to the test setup, meaning that the strains from the installation, mainly the bolt loading and gravity loads, are present in the measured strains. Since the main factor is strain range, the range for each of the gauges during the fatigue loading is of interest, but the mean strain is also important for characterizing the fatigue performance.

As previously mentioned, the strain field near the radiused fillet weld at the web-flange intersection is the area of interest for this fatigue study. For this reason, strain rosettes are installed on both sides of the specimen web at three locations along the curved geometry (NRW1/SRW1, NRW2/SRW2, NRW4/SRW4 in Figure 17) and aligned at three distances from the toe of the weld (NRW2/SRW2, NRW3/SRW3, NRW5 in Figure 17) to capture the strain distribution in the web. Additionally, three rosettes are placed on the top flange; two on the underside (NRFB1/SRFB1) and one on the topside (SRFT1) to characterize the strain in the flange. The uniaxial gauges are placed on the specimen close to the interface between the specimen and its boundary conditions, specifically the actuator and the bracket support (NU1 to NU6; SU2, SU5; VP1, VP2 in Figure 17.) These uniaxial gauges are in place to measure the structural response at the interfaces and provide data useful for characterization of boundary condition effects.

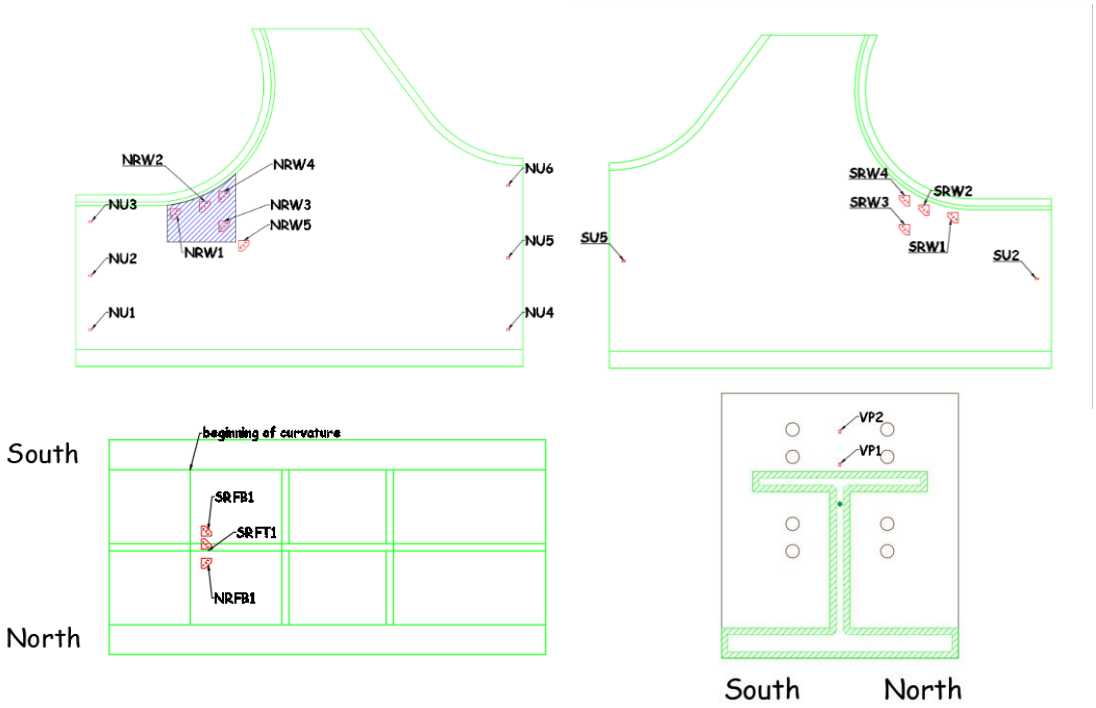

Figure 17 - Instrumentation of Gusset-less Fatigue Specimen

In addition to the strain gauges, DIC is used to measure strains and displacements in the area of interest. In this study, 2-Dimensional DIC is being used. The camera used in this study is the Grasshopper 5.0 MP Mono FireWire 1394b with a 2448x2048 resolution. For image capturing, the VIC-Snap software from Correlated Solutions is used. The images are taken in 30 second intervals, spaced 20 minutes apart, at a capture frequency of 12.5Hz during the capture period. The 30 second capture, followed by 20 minutes of no recording is chosen to reduce the total number of images due to the significant processing time required. The 12.5Hz capture frequency, within that 30 second capture window, is chosen as the highest capture frequency possible given the hardware used in this setup. A schematic, as well as a picture of the DIC setup used in the test is

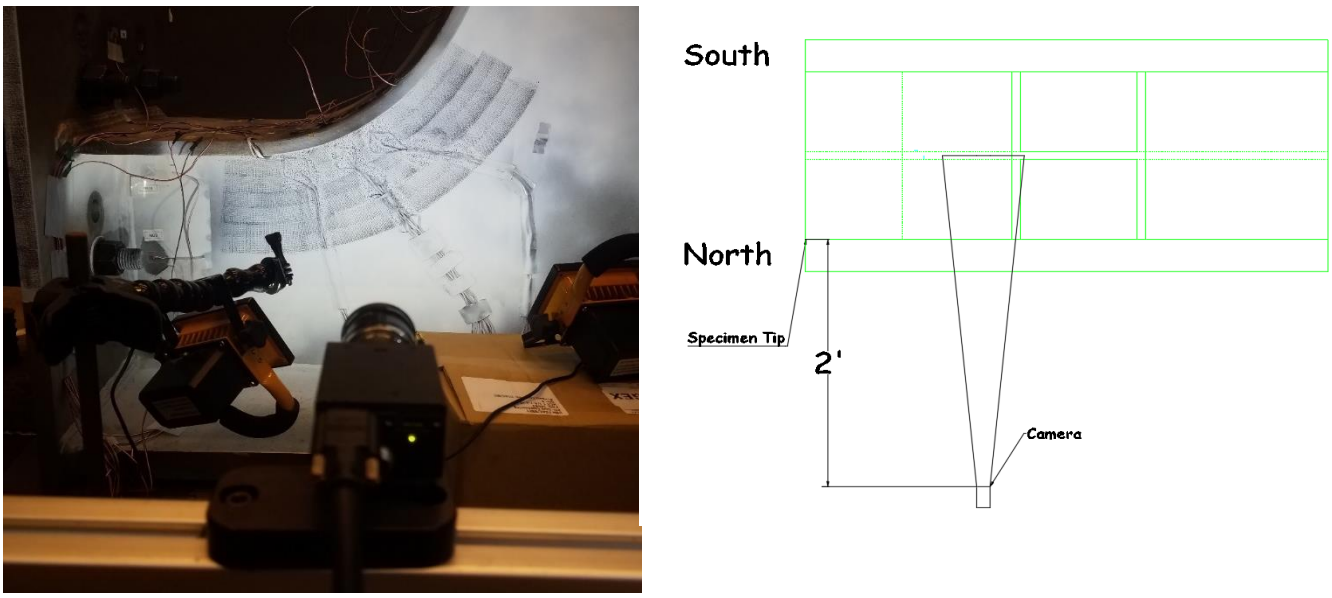

Figure 18 - DIC Schematic and Setup

shown in Figure 18. The area depicted by the blue hatch pattern in Figure 17 represents the field of view that is captured with the DIC via a speckle pattern. The speckle pattern was applied with an ink roller supplemented by permanent marker to produce a high-quality pattern. A sample of the pattern is shown in Figure 19.

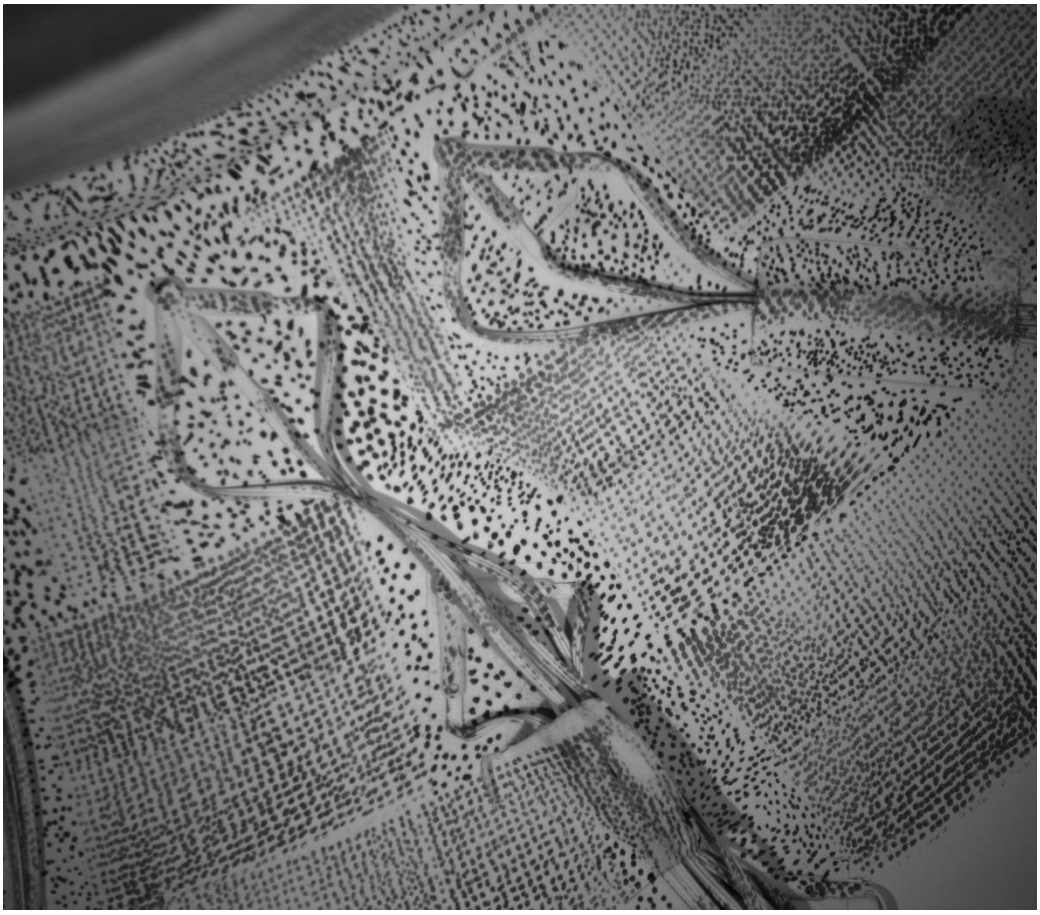

Figure 19 - Sample Speckle Pattern

These DIC measurements serve as verification for the strain rosettes as well as a full-field characterization in this region at locations in which strain rosettes are not present. The combination of all the measurements from DIC as well as the strain gauges can also be used as a comparison to the numeric model of the test setup.

3 FATIGUE TEST MONITORING

This chapter will introduce the developed fatigue test monitoring protocol specific to this test. After this introduction, the System Identification (System ID) that has been performed will be explained in detail and the results of the System IDs performed will be presented. Finally, the force-displacement relationship of the actuator will be discussed, specifically regarding how it is a representative measurement for the behavior of the system.

3.1 Fatigue Test Monitoring Protocol

Ensuring consistent behavior in a high-cycle fatigue test is important, especially when the test must be performed in multiple smaller testing intervals in which the loading is paused and later resumed. There is an added complication in this study in the potential for changes in the test setup due to the fatigue loading of the test setup. Specifically, the shims under the specimen tip as well as all the bolted connections in the test setup have the potential for degradation, in the case of the shims, or loosening in the case of the bolted connections. In this scenario, it is critical to develop a protocol to systematically monitor the structural response of the system and use this data to identify any changes in behavior throughout the high-cycle fatigue test. Additionally, a monitoring protocol aids in identifying potential fatigue damage or failure in the specimen. For these reasons, a test monitoring protocol was developed for this study in order to maintain a consistent structural behavior throughout this test. A graphical

representation of the monitoring protocol is shown in the form of a flowchart in below Figure 20.

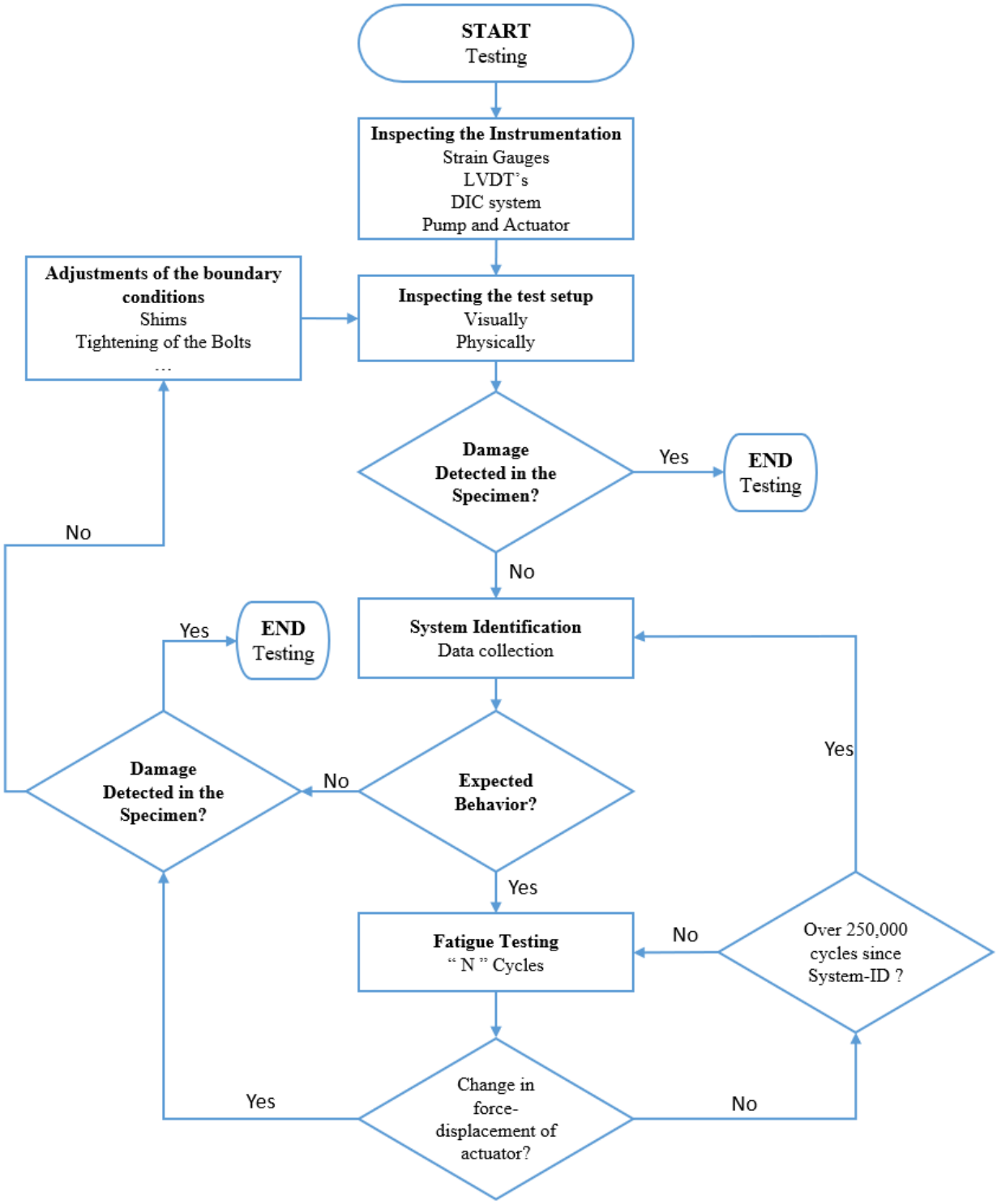

Figure 20 - Monitoring Protocol Flowchart

The flowchart developed for monitoring the high-cycle fatigue test is specific to this research, but the general concept can be applied while the specific monitoring details can be altered to be used in another test.

The start point of this monitoring protocol is equivalent to day zero of testing, meaning that the specimen is mounted in the test setup and is properly instrumented for the fatigue test, but no fatigue testing has been performed on the specimen. Advancing from the start position in this protocol, the next step is to inspect the instrumentation used in the test. This is one of the most critical steps, specifically because the monitoring protocol revolves around making data driven decisions using the measured structural response from the instrumentation. Therefore, it is extremely important to ensure that the measurements that are being used are not compromised. There are a few things that are checked in this instrumentation inspection;

1. Strain gauges, both rosettes and uniaxial gauges, are checked for debonding from the specimen surface. Additionally, the wiring is inspected for any damage. This check is in place to ensure that there has not been any physical change to the gauges. Specifically, due to the location and length of the wires connecting the strain gauges to the measurement system, there is a significant risk that the wires become damaged due to foot traffic in the laboratory.

2. A gauge test, in the form of recording strains for ~10 seconds, is performed to check the strain values being recorded by the gauges. This test will quantitatively indicate any erroneous strain measurements as well as allow the user to quickly identify which, if any, strain gauges need to be inspected further. One example of this is if a strain gauge wire is damaged due to foot-traffic, an abnormally high strain will be shown in the gauge test.
3. The LVDT's are tested in a similar fashion to the gauges. They are visually inspected to ensure that the required contact to the specimen is made and the direction of the LVDT is still consistent with the measurement in the direction of interest. Additionally, the displacements are recorded for ~10 seconds to check for any measurement errors.
4. Lastly the DIC system is assessed. First the camera is turned on and the lens cap removed. The two LED lights are turned on and positioned to illuminate the area of interest. Next the camera is inspected for perpendicularity to the surface in which the area of interest is located on. The saturation of the light is checked in the VIC-Snap software and adjusted to the optimal level through adjustments to the exposure timing. Lastly, images are recorded for ~10 seconds to check for any errors in the recording software. One specific example of an error in this study was that the cameras would sometimes not record at the specified frequency, so adjustments had to be made before testing.

Once the instrumentation has been inspected, ensuring that it is functioning as expected, the specimen and the test setup are inspected visually and physically. This inspection is in place to check for any visual damage in terms of cracking (fatigue related or otherwise), movement of the shim supports, any unexpected wear in the test setup, and any loosening of the bolts. Figure 21 shows an example of shim support which has been

Figure 21 - Shim Support Movement

rotated and shifted. If there is damage detected at this point, the testing does not progress, and the damage is investigated further, but if there is no damage detected in the specimen or test setup a System ID is performed.

The System ID is a full characterization of the structural response of the test setup through measurements at key points in the test setup while it is being subjected to a short version of a testing interval using the fatigue loading protocol. A detailed explanation of the System ID and the measurements taken will be provided in section 3.2. The response captured with the System ID is used as a baseline behavior to compare future system IDs to. Once the System ID is performed and the data is processed, the research team compares the observed structural behavior to the previous System ID or a theoretical behavior in the case of the first system ID. Specifically in this study, the first measurements were compared to a numerical model of the test setup. At this point, the behavior is evaluated, and a decision is made on whether the behavior is as expected or if there is a significant difference between the expected and the measured response.

If the response is significantly different than expected, adjustments must be made to the system to modify and correct the behavior. Some examples of how this is accomplished are; adjusting the shim supports, re-torqueing the anchor bolts, and re-torqueing the bolts connecting the different parts of the test setup. Once the modifications have been made another inspection is performed followed by the System IDif there is no damage detected during the inspection. This process forms an iterative loop until the behavior is acceptable, at which point the fatigue testing can begin.

The fatigue testing is performed in testing intervals with a set number of cycles per interval. The intervals used in this research ranged from 2-hours (~26000 load cycles) up to 12-hours (~155000 load cycles), but due to the likelihood of data acquisition errors

occurring the test intervals were typically 2-2.5-hours. These intervals resulted in the least amount of data acquisition errors while maximizing the cycles performed in the testing interval.

After each fatigue test interval, regardless of the length, the actuator force-displacement hysteresis is examined, specifically the slope, or stiffness of the response. This measurement was identified as a representative measurement for the system response, meaning that if there is a change in the system response, there will be a change in the behavior of the actuator force-displacement hysteresis. This representative measurement will be discussed in greater detail in section 3.3. The hysteresis provides a quick way to determine if the behavior of the system has changed without having to perform a System ID after every testing interval. If there is a change in behavior between two test periods, adjustments should be made to the test setup and a System ID should be performed, iterating until the behavior is corrected. In the case that there is no change in behavior, an additional check is in place to ensure that there are not long intervals without characterization of the test setup. In this study, if there has been no change in behavior after a cumulative 250,000 cycles since the last System ID occurred, a System ID should be performed. This is essentially a safeguard to ensure that if there was a change in behavior, but the hysteresis did not reflect that change, the behavior would periodically be characterized.

In summary, there is a protocol in place to inspect the test setup and track the structural response periodically, or as needed. In addition to a full characterization, a

representative measurement has been identified and used to quickly see if there is a change in behavior. Using a systematic approach as described above and shown graphically in **Error! Reference source not found.**, ensures that consistent conditions are kept throughout the duration of a high-cycle fatigue test performed across multiple testing intervals.

3.2 System Identification

As previously mentioned the system identification (system ID) refers to a full characterization of the structural response of the test setup while it is being subjected to a short version of a testing interval using the fatigue loading protocol. The System ID serves two purposes: (1) ensuring the test is producing measurements in the expected range, and (2) monitoring and verifying the consistency of the structural behavior throughout the fatigue test prior to specimen damage.

In the current high-cycle fatigue experiment, due to the estimated cycles to failure, the test is completed over multiple testing periods. The test is performed under constant loading (force) amplitude and it is expected that the specimen will experience a consistent range of stress, which can be verified, for example, by evaluating the strain history measurements collected during the test. The stability and consistency of the testing environment and boundary conditions is critical during the test. Consequently, it is critical to characterize the behavior prior to the test. Any changes in the test setup during the test could result in system responses that are inconsistent. Using the System ID, a reference set of measurements is generated to serve as benchmark for future

characterizations of the system. Using this benchmark as a reference, the test setup is periodically checked against previous characterizations to ensure that the behavior is consistent between fatigue testing intervals.

One of the key features of the System ID used in this study is the ability to identify behavior at key locations. This is achieved using many sensors and data acquisition devices, namely;

- 2-Dimensional Digital Image Correlation (2-D DIC)
- Linear Variable Differential Transformers (LVDTs)
- Strain Gauges

The background on the measurement devices has been provided in section 2.3. There are two significant change between the instrumentation plan for the fatigue test and the instrumentation used in the System ID. The first is the use of GoPro cameras to capture 2-D DIC measurements at additional locations along the test setup. The second is the use of LVDTs as verification points for the DIC measurements.

The locations of the additional measurements using the GoPro cameras are shown as the red hatched areas in Figure 22. Each location was chosen to characterize the boundaries between different portions of the test setup as well as the relative behavior of each component of the test setup. The LVDTs used in this study is an LVDT-01-030 from BDI, the data acquisition software used is STS-LIVE, and the capture frequency is 100Hz. The locations of the LVDTs are not shown in Figure 22, but are always present in the

system ID. Typically, there are two or four LVDTs used during the system ID depending on availability. The reason they are not depicted is due to the variability in their location along the test setup. Since the LVDTs are the easiest measurement device to relocate and take measurements, the location of the measurements taken with the LVDTs is changed to verify different DIC locations or take measurement where the DIC is not implemented. It is important to note that all measurements are taken simultaneously during each System ID session.

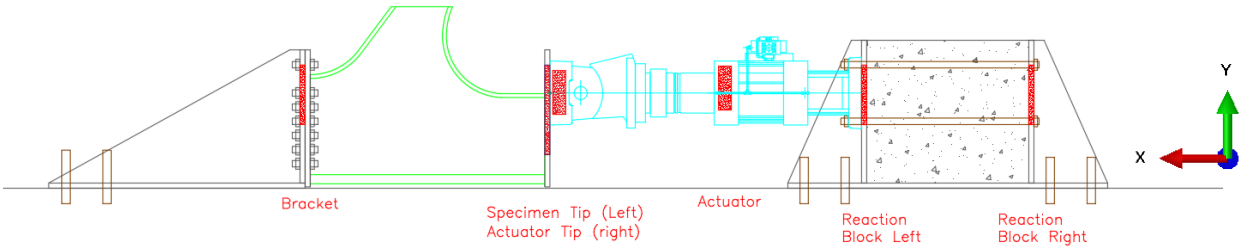

Figure 22 - System Identification - DIC Measurement Locations

The following figures are results from two selected system IDs performed at different point throughout the overall fatigue test. Additional system ID results are shown in Appendix C. The first system ID shown was performed on 07/24/18, which was after approximately 260,000 fatigue loading cycles and the second system ID was performed on 10/23/18, after approximately 1,510,000 fatigue loading cycles. Between these two testing windows, the test setup underwent minor changes in the form of maintenance to the test setup. The primary adjustments were made in the form of replacing shims that were being worn through, and re-torqueing bolts throughout the test setup. The results from the system IDs will be labeled by the date they were

performed, either in the figure title or the legend if the results from both dates are plotted together.

Figure 23 and Figure 24 show the loading history for both System IDs, note that the loading protocol is the same except for the duration of the cyclic portion of the loading. In the test performed on 07/24 the cyclic portion was approximately double that of the second test shown. The reduction in cyclic duration was done to cut down on the overall processing time of the data from each System ID.

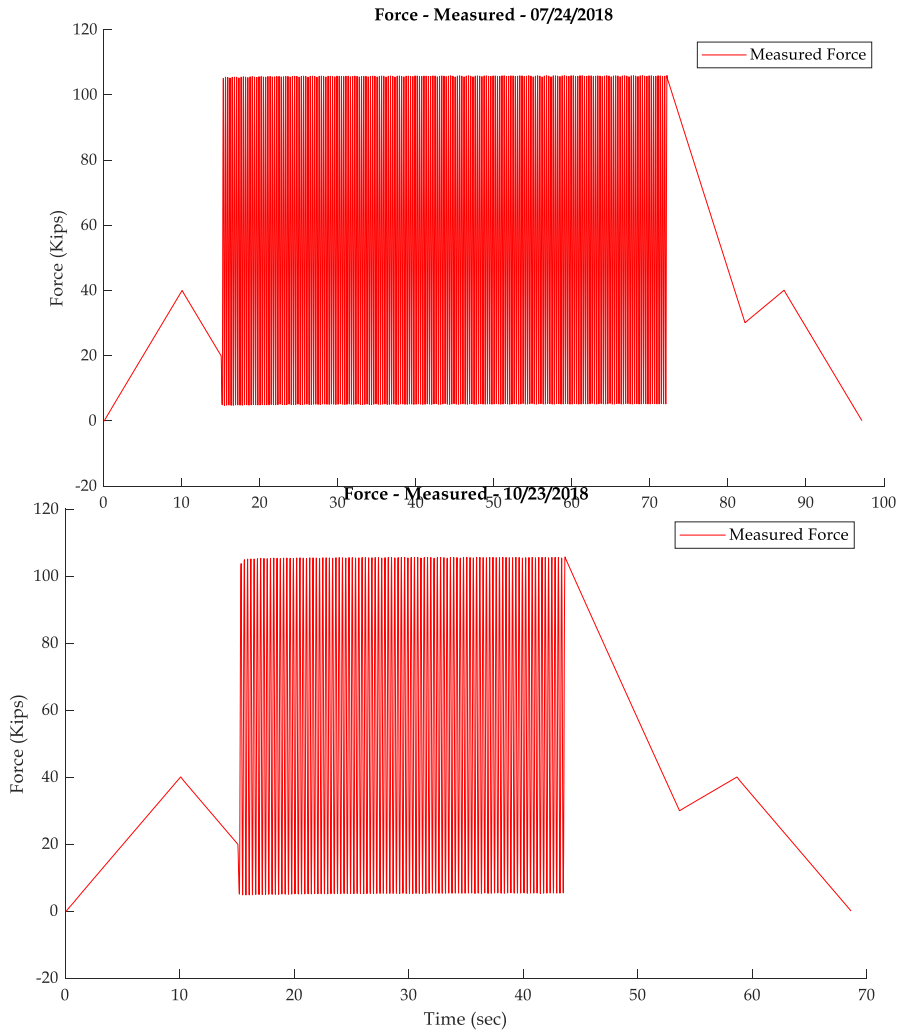

Figure 24 - Force Time-History - 10/23

Figure 25 shows an example of the cross-verification between the measurements with the 2-D DIC and an LVDT, in this case the location is the tip of the actuator and the

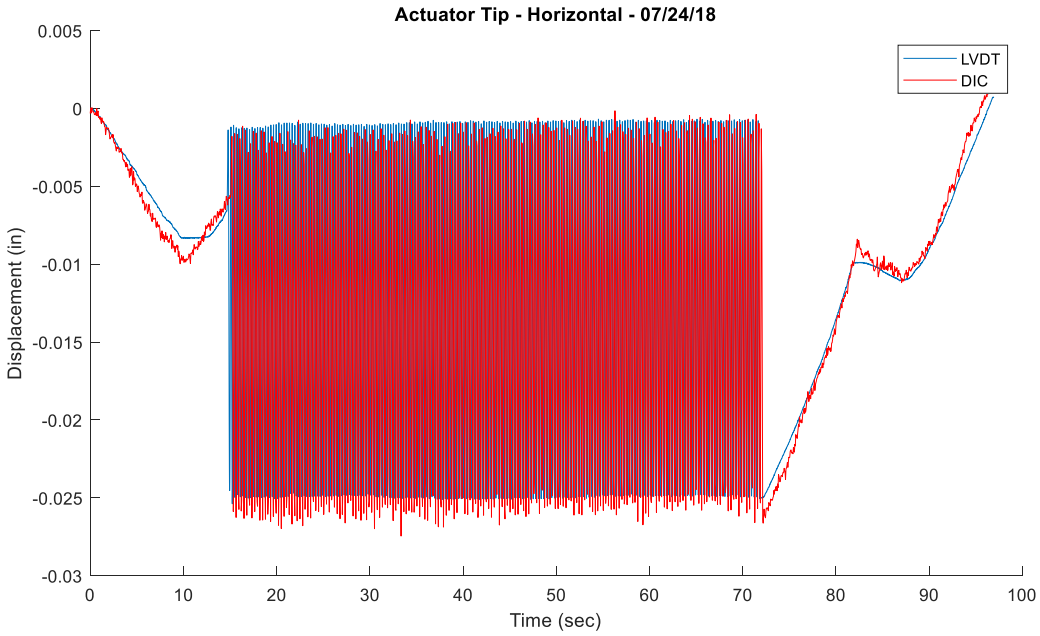

Figure 25 - DIC and LVDT Verification

measurement taken is the horizontal displacement. As the graph shows, the measurements match closely, it should be noted that this is raw data with no post-processing or adjustments.

Since the duration of the cyclic portions of the loading across the two testing periods are different, the following figures will be limited to a 2-second window during the cyclic loading to compare the same measurements from the two different test windows. Figure 26 shows the horizontal displacement of the right side of the reaction block from both test periods. It should be noted that this data is raw, unadjusted, data

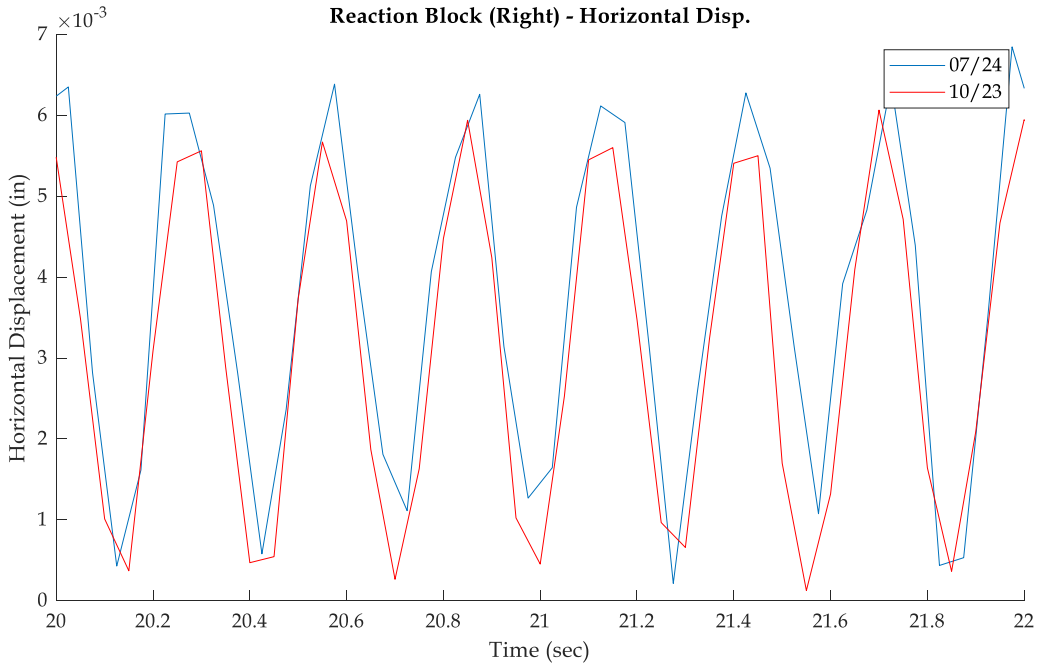

Figure 26 - Reaction Block (Right) - Horizontal Displacement

output from the 2-D DIC. For this reason, some truncations can be noted in the measured response due to the capture frequency of the cameras used. Since the frequency was not high relative to the loading frequency, the peaks of the response were not always captured. Based on the output, a cyclic range of displacement, in the vertical and horizontal directions, was measured for each of the two data sets and the percent difference was calculated based on these cyclic ranges. This was done for the

displacement at each of the measurement locations along the test setup and is shown below in Table 1.

Table 1 - System ID Comparison

Location	Date	Cumulative Fatigue Cycles	Horizontal Displacement Range (in)	Vertical Displacement Range (in)
Reaction Block (Right)	07/24	260375	0.00583	0.00349
	10/23	1546414	0.00570	0.00309
	Difference	1286039	2.4%	11.5%
Reaction Block (Left)	07/24	260375	0.00528	0.000690
	10/23	1546414	0.00558	0.000700
	Difference	1286039	5.6%	1.3%
Actuator	07/24	260375	0.00862	0.00322
	10/23	1546414	0.00873	0.00336
	Difference	1286039	1.3%	4.3%
Actuator Tip	07/24	260375	0.0247	0.01137
	10/23	1546414	0.0257	0.01019
	Difference	1286039	4.3%	10.4%
Specimen Tip	07/24	260375	0.0233	0.00993
	10/23	1546414	0.0240	0.00979
	Difference	1286039	2.8%	1.4%
Bracket	07/24	260375	0.01026	0.001572
	10/23	1546414	0.01121	0.001627
	Difference	1286039	9.3%	3.5%

Based on this table, some slight differences can be seen throughout the comparison across the two testing periods. It is important to note the scale of these measurements when making the comparison, the difference between the two displacement measurements are often less than 1/1000th of an inch. This resolution alone leads to potential measurement errors based on the way the 2-D DIC is calibrated for scale, if there is slight error in defining the proper scale for the analysis the measurements will be off slightly. One other

potential cause of error, as previously mentioned, is the minor adjustments between the shim supports, as well as the torqueing of the bolts. Overall, the differences ranged from 1%-11% with an average difference of 4.84% between the two measurement dates.

3.3 Representative Measurement

Ensuring consistent behavior in a prolonged test is important but performing a System ID before every testing period would be cumbersome and would add a significant delay between testing due to the processing time required to analyze the System ID measurements. Hence, it is important to have the availability of benchmark measurements during the fatigue test that could be used as reference measurements to identify potential undesirable changes in the structural response of the system. Having such measurements allows the test to be monitored between System ID intervals and can be used as a tool to decide when an additional (unscheduled) System ID needs to be performed.

In this study, the measurement that is being used as a representative characterization of the system is the force-displacement relationship of the actuator. This is measured through the actuator LVDT, with respect to the displacement, and the actuator load-cell for the force. The force-displacement relationship is an indicative measurement because if a consistent force is applied (force-controlled test), any change in a stable system, for example boundary conditions, will be reflected in this measurement. For example, if the attachment bolts are not tightened at the specimen-bracket interaction the actuator will end up displacing a further distance to reach the

same level of force compared to if the bolts were completely tightened. Therefore, if there is a noticeable change in the force-displacement hysteresis of the actuator, the test setup ought to be evaluated for changes in the supports, any loosening of bolts, or any noticeable damage. If the source of the change is not visible, a full characterization is required in the form of the SI process. This creates a systematic approach for maintaining a consistent structural response throughout the fatigue test.

Throughout this study, a history of the force-displacement relationship has been monitored to create a benchmark measurement and use this benchmark to assess the presence of changes in the system. Figure 27 through Figure 31 show an overall history of the force-displacement relationship of the actuator throughout the setup and testing phases of this project. Each of the data sets shown, labeled by the date in which the test was performed, are approximately 50 seconds of the cyclic loading protocol close to the end of the respective testing interval. Taking a data window close to the end of the testing period ensures that the maximum number of cycles occurs between the comparisons of the data sets. This is desirable to ensure that the changes that occurred during that testing period are reflected on the measurement before the next testing period occurs.

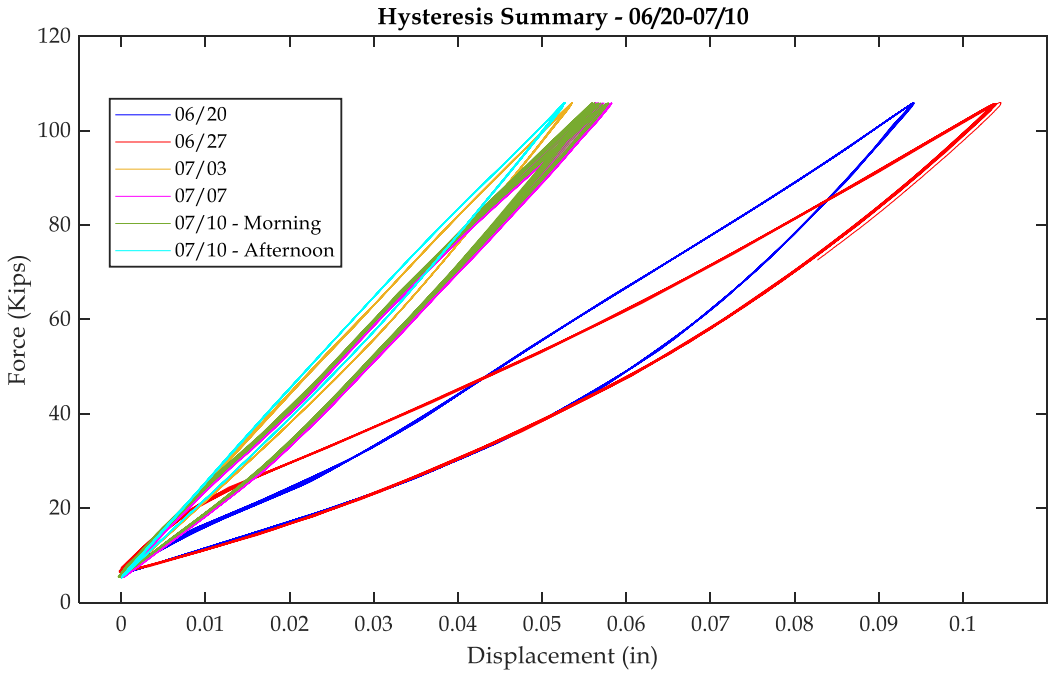

Figure 27 - Hysteresis 06/20-07/10

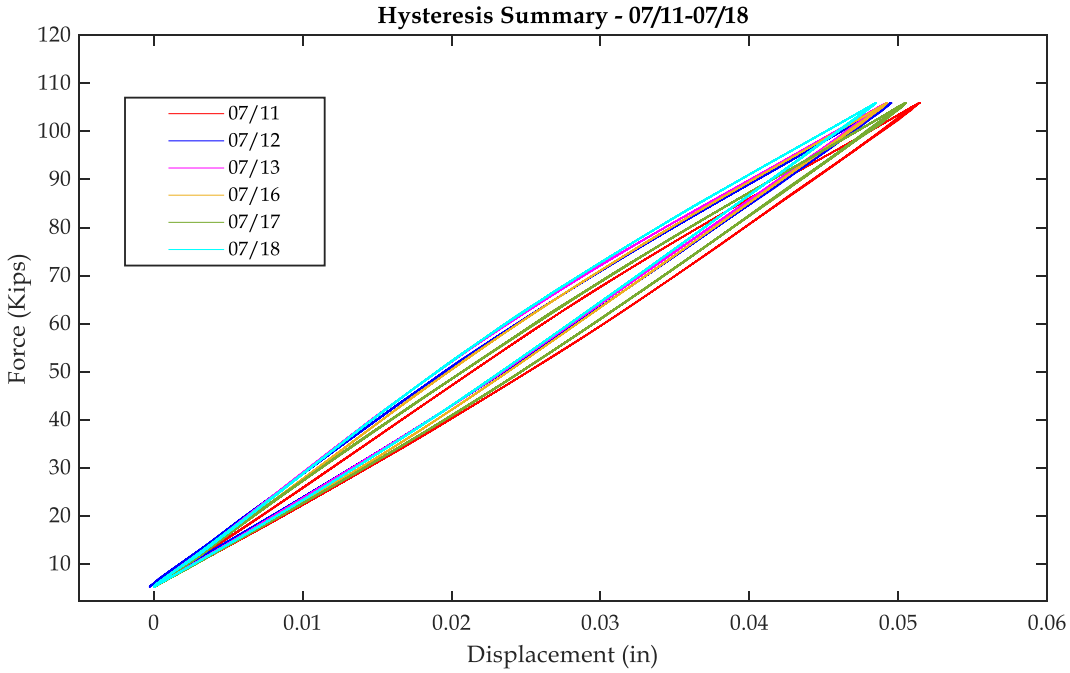

Figure 28 - Hysteresis 07/11-07/18

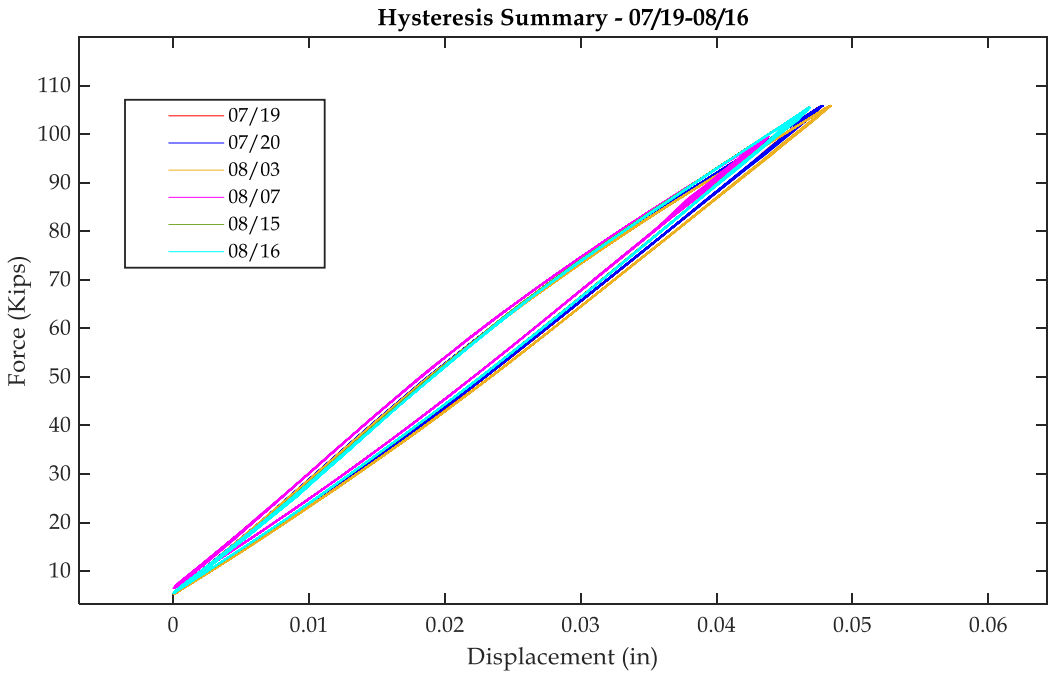

Figure 29 - Hysteresis 07/19-08/16

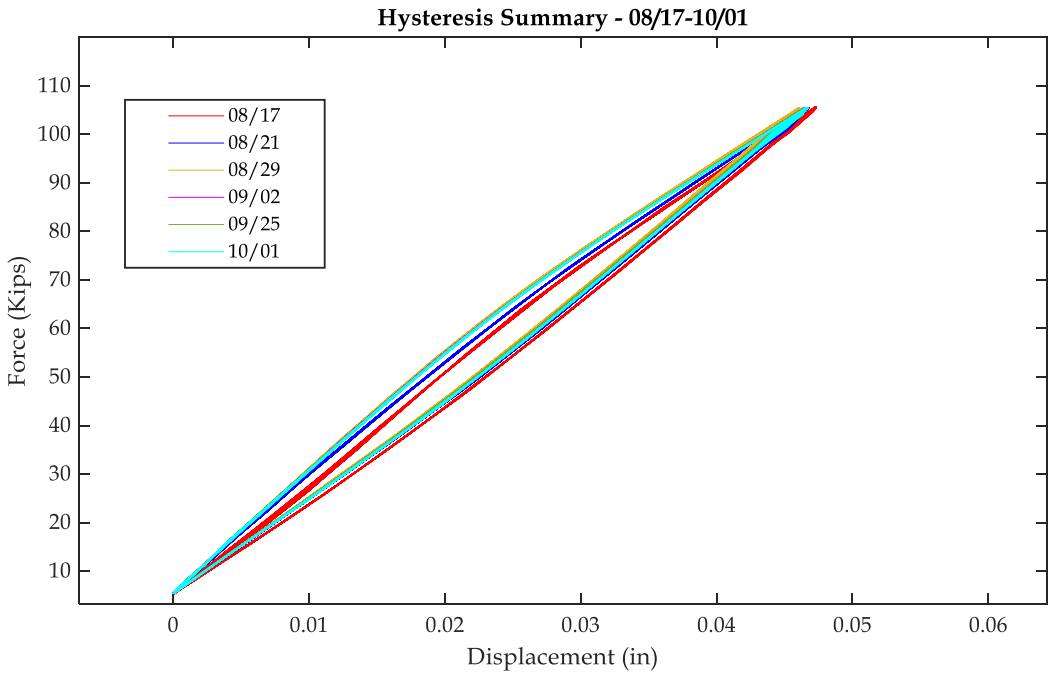

Figure 30 - Hysteresis 08/17-10/01

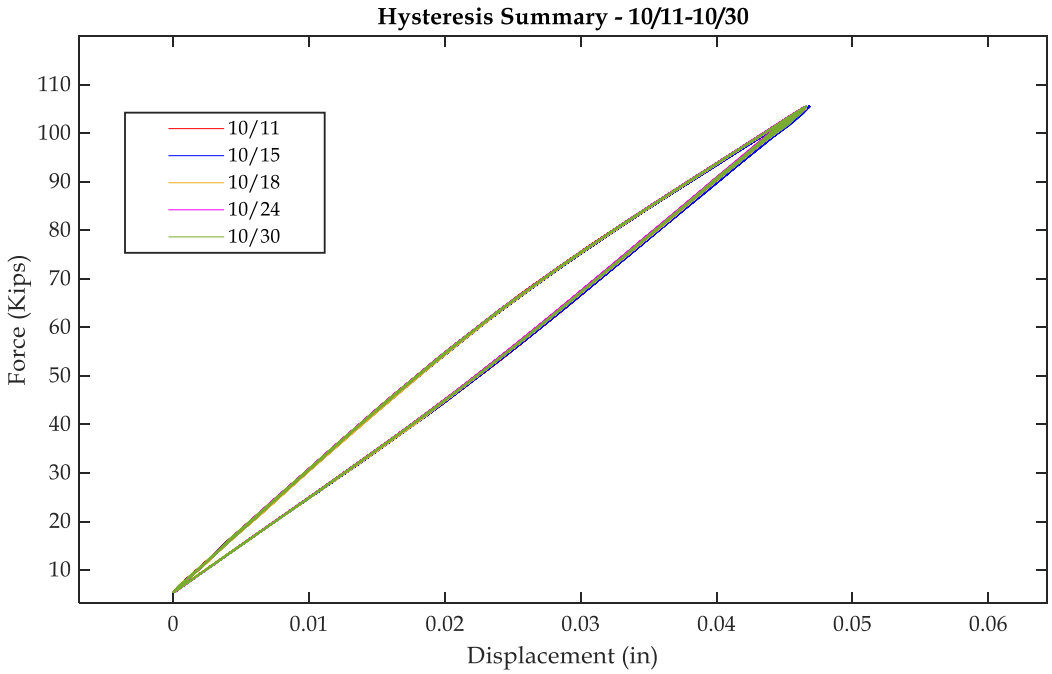

Figure 31 - Hysteresis 10/11-10/30

As the figures above show, besides the initial hysteresis shown in Figure 27, there is a consistent force-displacement relationship across the different testing periods. This indicates that over the time frame between 07/11 to 10/30, the behavior of the test setup was consistent according to this measure. To be able to use this measurement as an indicator, as this study has, it was important to verify that any changes in the test setup would be reflected in this force-displacement relationship. The justification for defining the hysteresis as the representative measurement for the system behavior comes from the observed behavior during the first few test periods, namely 06/20, 06/27, 07/03, and 07/10. Each of these data sets will show the effect of different changes to the test setup and how they are reflected in the force-displacement

The first behavior that should be highlighted can be seen in Figure 32, which shows the force-displacement relationship from test periods on 06/20 and 06/27. The

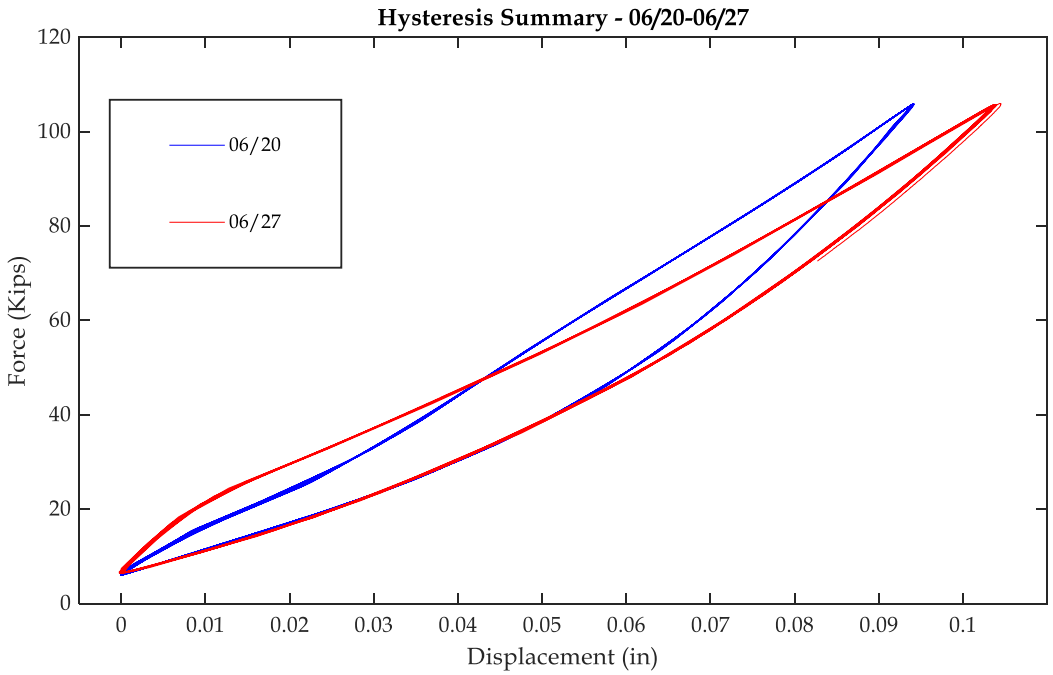

Figure 32 - Hysteresis 06/20 and 06/27

first data set, 06/20, was the first fatigue test period. After inspecting the test setup, minor grinding of the concrete floor was observed under the vertical attachment plate to the actuator. Therefore, the supports were modified from narrow steel channels to flat aluminum shims to mitigate this grinding. The objective of this change was to increase the surface area of the support to distribute the force and allow for the shims to slide on each other rather than the channel grinding against the concrete floor. The change in the force-displacement relationship between 06/20 and 06/27 shows a significant reduction in the slope from the previous test, which is attributed to the change from the steel channel to the aluminum shims. With this change, the specimen was able to displace further under the same load since the aluminum support was much more flexible.

Although this change was subtle, with a change of approximately 0.01 inches of displacement, it was clearly captured with the force-displacement relationship.

The next change in behavior is much more drastic relative to the overall behavior and can be seen in Figure 33. This plot shows the change in the force-displacement

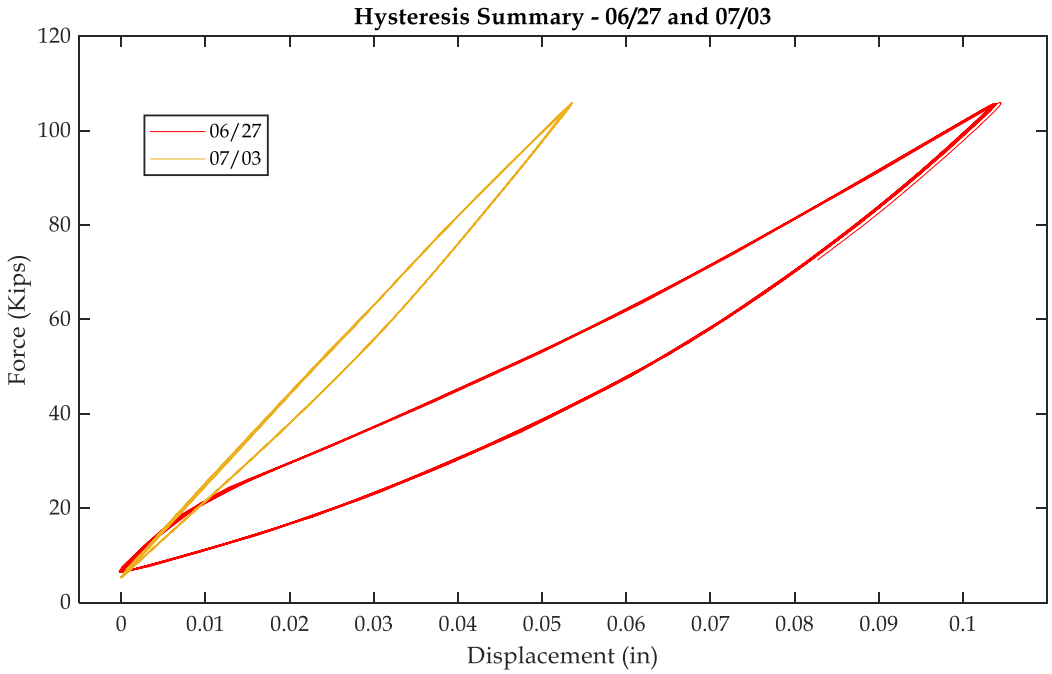

Figure 33 - Hysteresis 06/27 and 07/03

relationship between the 06/27 test period and the 07/03 test period. During the 06/27 test session, it was noted that the reaction block was rotating about the z-direction and had significant horizontal movement, so a decision was made to increase the torque applied to the anchors that clamp the reaction frame to the floor. This change is reflected in the change in slope between 06/27 and 07/03, where the increase in clamping force added significant stiffness to the overall system. This is due to the actuator previously having to displace more to achieve the same level of force, therefore, when the support was sufficiently restrained to the floor, the actuator did not have to compensate for any

additional movement. As the graphs show, the change in torque to the anchor bolts is clearly reflected in the force-displacement relationship.

The last behavioral change that should be highlighted is very subtle and is shown in Figure 34. Data from 07/03 compared to 07/10 shows a slight loss of stiffness in the

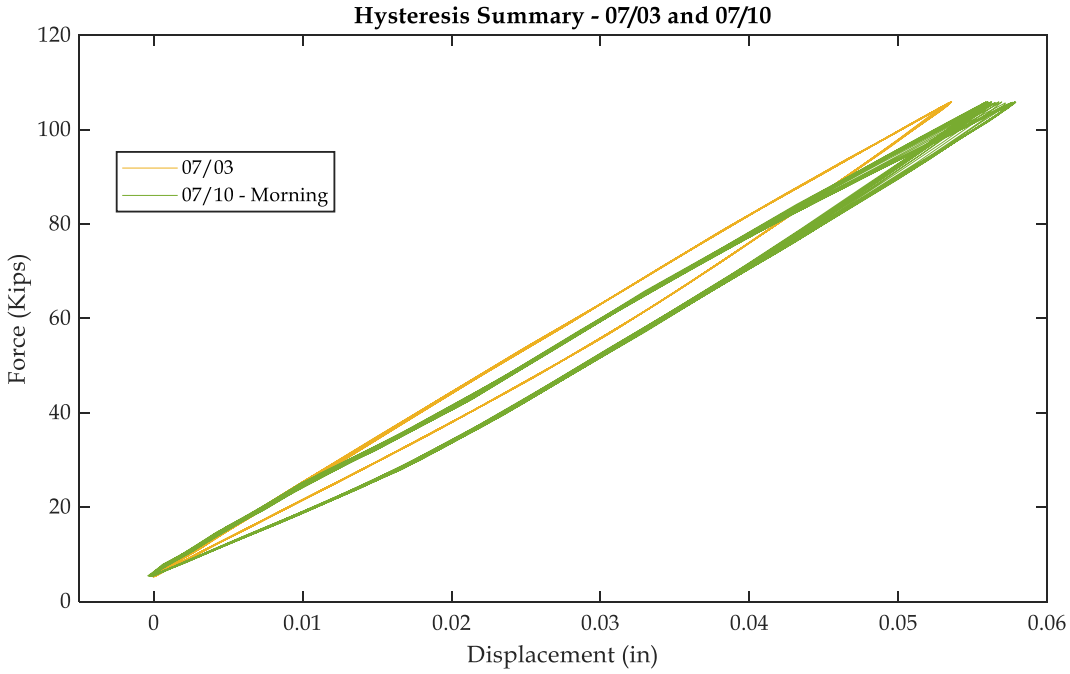

Figure 34 - Hysteresis 07/03 and 07/10

force-displacement relationship. During the 07/10 testing period the shim supports under the vertical plate became dislodged from their initial location. The test was stopped before reaching the desired level of cycles to adjust the support and improve the boundary conditions. This dislodging is reflected by the loss of stiffness as well as the fact that there is a change in behavior even across the short number of cycles shown in this plot. A zoomed in view, Figure 35, shows that while the shim is dislodging, the relationship is changing.

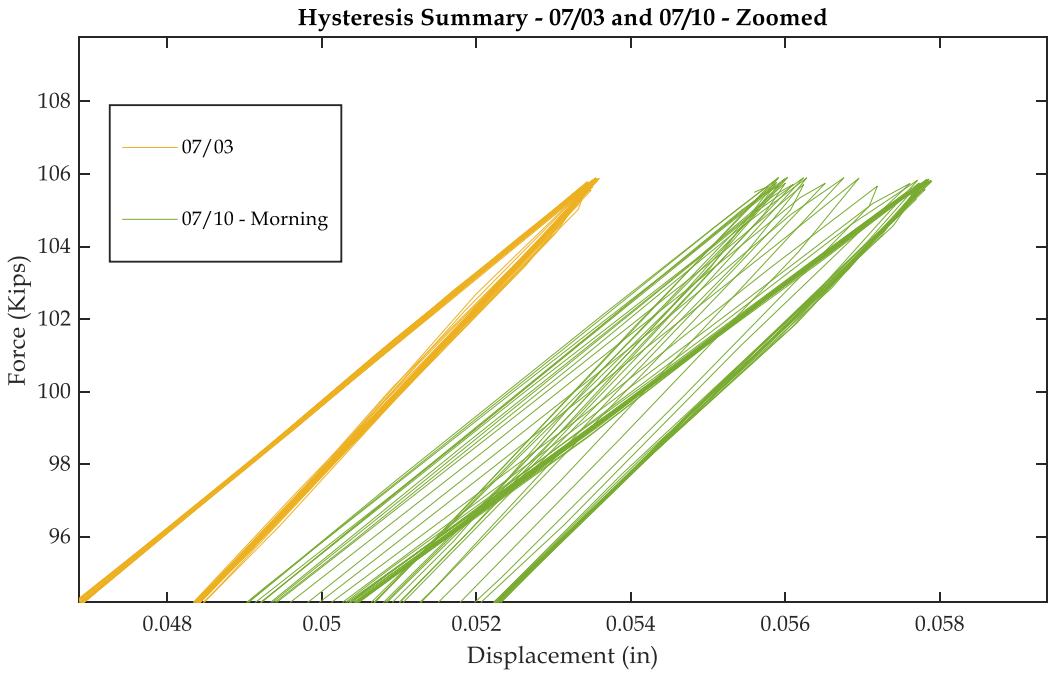

Figure 35 - Hysteresis 07/03 and 07/10 - Zoomed

This change in behavior was critical to prove that the force-displacement relationship is an effective measurement tool to identify undesirable changes in the system.

3.4 Summary

With a large-scale experimental setup, particularly one designed for fatigue testing, it is critical to ensure that there is consistency during the testing. In this study, this was accomplished using a systematic monitoring protocol to monitor the entire test setup. This protocol was developed with the design goals of consistency, reliability, and efficiency. For these reasons the characterization and structural monitoring of the test setup was done in two ways, a detailed, full characterization, in the form of the System

ID, and a representative measurement, in the form of the actuator force-displacement hysteresis.

The results from the System ID characterized the structural response of the entire test setup at critical locations. From this characterization, the behavior of the test setup was monitored and periodically checked for changes. Although there were slight differences between each characterization, the overall behavior was consistent throughout the test.

The force-displacement relationship was used as a fast way to detect changes in the behavior of the test setup. It was found that the physical changes to the test setup had a clear effect on the force-displacement relationship. These changes justify the use of this measure as a representative, quantitative, measurement of the overall system. After some initial changes near the beginning of the overall fatigue test, the force-displacement relationship reflected the consistency of the test setup over the time frame between 07/11 to 10/30.

4 FINITE ELEMENT MODELING

This chapter will discuss the need for finite element modeling of the fatigue test and setup. The chapter will then introduce the developed model of the test setup and discuss the modeling technique and assumptions made. Lastly, the results from the numerical analysis will be introduced and briefly discussed.

4.1 Finite Element Modeling

The use of finite element modeling was a powerful tool to estimate behaviors and structural responses of various components such as the specimen and test setup used in this study. A numerical model might not be a perfect representation of an actual test due to the idealistic conditions assumed in modeling, but it can still be used as a way to estimate structural behavior. With such a geometrically complex test specimen, it is important to be able to have a theoretical comparison point for the measurements being recorded. Additionally, understanding the stress distribution in this complex specimen is critical in order to maximize the efficiency of the instrumentation of the test setup. Lastly, numerical models can be used to investigate the effect of different changes to boundary conditions in the test setup and aid in decision making in terms of potential modifications to the test setup.

Although there are many benefits to having a numerical model, the results must be examined with caution. It is important to be able to distinguish whether the numerical results are true, or a close representation of reality. Often times, a complex numerical model contains sharp geometries and transitions which can result in spurious results in

the form of stress concentrations. For this reason, engineering judgement must be used when using numerical models for analysis.

4.2 Fatigue Test Model

In this study, multiple finite element models (FEM) of the specimen as well as portions of the test setup were developed and refined using ABAQUS® CAE/2017 [34]. The models were created in order to estimate stresses and strains in the specimen as well as the overall structural response of the test setup. As noted in section 2.3, the original model of the specimen [31] was used to estimate the overall stress contours to determine the locations of interest for the instrumentation. Although this model provided a good approximation to the areas of interest, an error in the modeling of the attachment plate which connects the specimen and actuator was discovered. The error resulted in a false approximation of stresses in the vertical plate which attaches the actuator to the specimen. This error was localized and did not influence the area of interest, but the decision was made to remodel the specimen to ensure that the behavior throughout was accurate. Additionally, the model was expanded to include a more detailed model of the welds in the specimen, the actuator swivel, the support bracket, the rigid floor, and the bolts throughout the test setup. The goal of this more detailed model was to create a numerical model of the test setup and understand the true behavior of the boundary conditions not just the specimen. The results of the finite element analysis (FEA) are compared to the actual measurements from the test in section 5.2 to verify the structural response of the model.

The FEM, shown in Figure 36, consists of four main parts: actuator swivel, specimen, bracket, and rigid floor. The connection specimen consists of a vertical attachment plate on the actuator side, the front-top flange, the web, the bottom flange, the back-top flange, and the vertical attachment plate on the bracket side, and welds between all of these parts. The geometry of the fabricated parts, as well as the material properties used in this FEM, are the same as those shown in Figure 9.

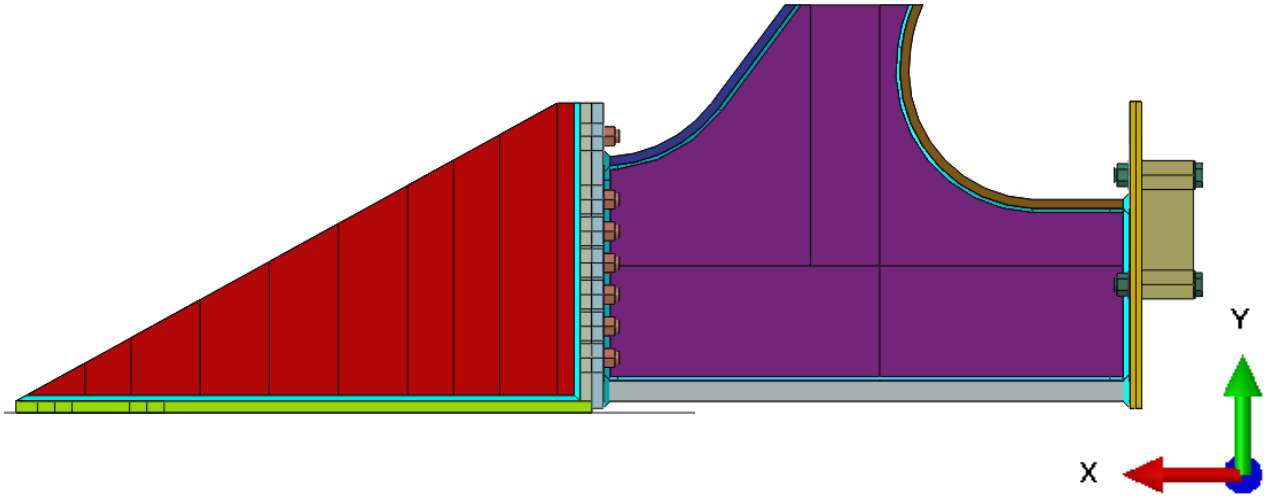

Figure 36 - Finite Element Model of Experimental Test Setup

In this study, the interaction of the different components was chosen carefully to give a realistic response. The specimen components are connected by the weld surfaces with a tie interaction. This means that the parts are not bonded to each other directly, but the weld is bonded to each of the individual parts. In addition to this, the only interaction between the individual parts is modeled with surface-to-surface contact. These interactions were chosen to simulate the most realistic transfer of stresses through the specimen, which would be through the weld itself or via contact between the various components of the model at their intersections. This modeling technique also allows for

a better estimate of the stress distribution through the weld geometry. The same approach was taken when modeling the support bracket, all forces are transferred through the welds or through part to part contact.

Further, the bolted connection of the specimen to the actuator swivel, as well of the specimen to the bracket, are simulated in the numerical model. Each bolt is modeled as a single solid part consisting of the bolt (shaft and hex-head), one washer on either end, and the hex-nut. The bolt's interactions with each individual component are modeled as surface-to-surface contact using the washer surfaces as the contact surface to the individual parts. This interaction was chosen to simulate the interaction between parts including their potential separation or loss of contact, whereas the tie constraint would simulate the components working as a unit. The last modeled interaction is between the bottom of the support bracket and the rigid floor. This interaction is modeled as a frictionless "hard" contact between the bottom surface of the support bracket and the top surface of the rigid floor. The frictionless "hard" contact interaction allows the bracket to press against the rigid floor without penetrating it or having any frictional force generated between the two surfaces.

The boundary conditions of the FEM were chosen to be representative of those present in the experimental test setup. Boundary conditions are applied at four locations in this FEM; the swivel's center of rotation, the bottom surface of the vertical attachment plate on the actuator side, the surface of the rigid floor, and the locations of the anchor holes in the bracket.

The actuator swivel is restrained from rotation about the X, Y, and Z directions and allowed to translate in the X, Y, and Z directions. These restraints were selected to simulate the swivel, which has its orientation locked in place, preventing any rotations during loading. This boundary was applied by coupling a reference point, located at the center of rotation of the swivel geometry, with the swivel, and restraining the rotations of this reference point, but allowing it to translate freely.

The bottom surface of the vertical attachment plate on the actuator side is restrained from rotation about the Z direction and restrained from translations in the Y direction. These restraints are representative of the metal shim supports that are under this vertical plate, these shims slide on top of each other while restraining any vertical (Y direction) movement and preventing rotation. This boundary was applied by coupling a reference point to the bottom surface of the vertical attachment plate and restricting the rotation about the Z direction and the translations in the Y direction of the reference point.

The bracket is restrained from translations and rotations at the location of the anchors. This is meant to simulate the near fixed-end condition created by the four anchors at the end of the bracket. This was accomplished by coupling the inner surfaces of the anchor holes to reference points located in the center of the circular holes and restraining all translations and rotations.

Lastly, the rigid floor is restrained in all directions against translations and rotations to simulate the actual floor under the test setup. This was applied by coupling

a reference point to the entire bottom surface of the rigid floor and restraining all translations and rotations.

The loading protocol is implemented in the numerical model in two steps; the pre-tensioning step, and the static loading step. The pre-tensioning step is created to simulate the application of the bolt loads generated from tightening the bolts that connect the various components together as discussed previously while the static loading step is meant to simulate the fatigue loading. These two steps were created to give a better approximation of the behavior of the test setup, including the behavior during installation (pre-tensioning step), and not just the specimen under idealized fatigue loading. Additionally, since the instrumentation, namely the strain gauges, are calibrated when the specimen is uninstalled, this will be a more representative comparison to the measured data.

As mentioned, the pre-tension step occurs first. In this step a pre-tension load is applied to the bolts, creating a clamping force on the two components that the bolt is connecting. This is meant to be consistent with the actual axial force applied to these bolts. This force was estimated by converting an applied torque of 800 ft-lb to an axial force which was then applied to each bolt in the FEM through the bolt-load option in Abaqus. The way that the bolt-load applies a force is by pulling the bolt-head and nut towards the center of the bolts, simulating a tension force on the bolt which causes it to clamp the parts that it is in contact with. Once the pre-tensioning of the bolts is completed the static loading step is performed.

In the static loading step, a 100 Kip ramp tensile load in the X direction, is applied to the actuator swivel. The load applied is equivalent to the loading range applied to the specimen during a fatigue test, from a minimum of 5 Kip to maximum of 105 Kip. The load is applied by applying a point load of 100 Kip to a reference point coupled to the swivel. The forces are then transferred from the swivel to the bolts and finally into the specimen.

The overall meshed model is shown in Figure 37. In this model, three element types were used throughout the assembly depending on the geometry and part type. The three elements used were the following; linear hexahedral elements – C3D8R, quadratic tetrahedral elements – C3D10, and linear quadrilateral elements – R3D4.

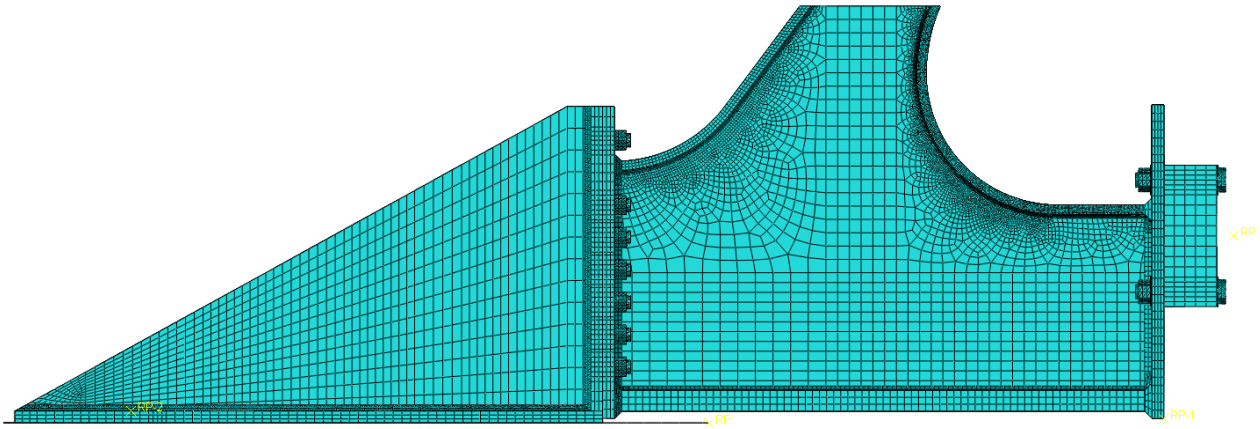

Figure 37 - Meshing of Entire Model

The most commonly used element was the C3D8R element, totaling at 226,228 elements. This element was used as the default element where the geometry was compliant with the restrictions of the Abaqus mesh generation. This element is a linear hexahedral element with eight nodes, each node having three translational degrees of freedom. Generally, the model was partitioned in such a way to allow transitions from regions of

fine mesh sizes to larger sizes. Additionally, the partitions serve to manipulate the geometry and change the mesh type in a region. The second most commonly used element was the C3D10 element, totaling at 38,525 elements. This element was primarily used in regions of complex geometry where the hexahedral mesh would not work. This element is a quadratic tetrahedral element with 10 nodes, each node having three translational degrees of freedom. Lastly, 6,240 R3D4 elements were used to model the rigid floor. This element is a rigid linear quadrilateral element with four nodes. In total the current model has 270,993 elements and the total analysis time was approximately 90 minutes using a direct solver. This mesh was the result of a meshing sensitivity analysis in which many mesh sizes and types were used to find a balance between resolution, accuracy, and analysis time.

4.3 Results – FEM

As previously noted, the finite element model used in this project went through many iterations before reaching the level of detail of the current model. It should be noted that throughout this project, the numerical model was not calibrated or adjusted to more closely match the results from the fatigue test. The fatigue test and modeling were performed simultaneously and separately, meaning the model used was a blind analysis.

The following figures will show the results from the numerical analysis using the previously described loading protocol. Figure 38 shows the overall displaced shape of the model, and Figure 39 shows the deflected shape of just the specimen portion of the model. Both deflected shaped are visually magnified by a factor of 100.

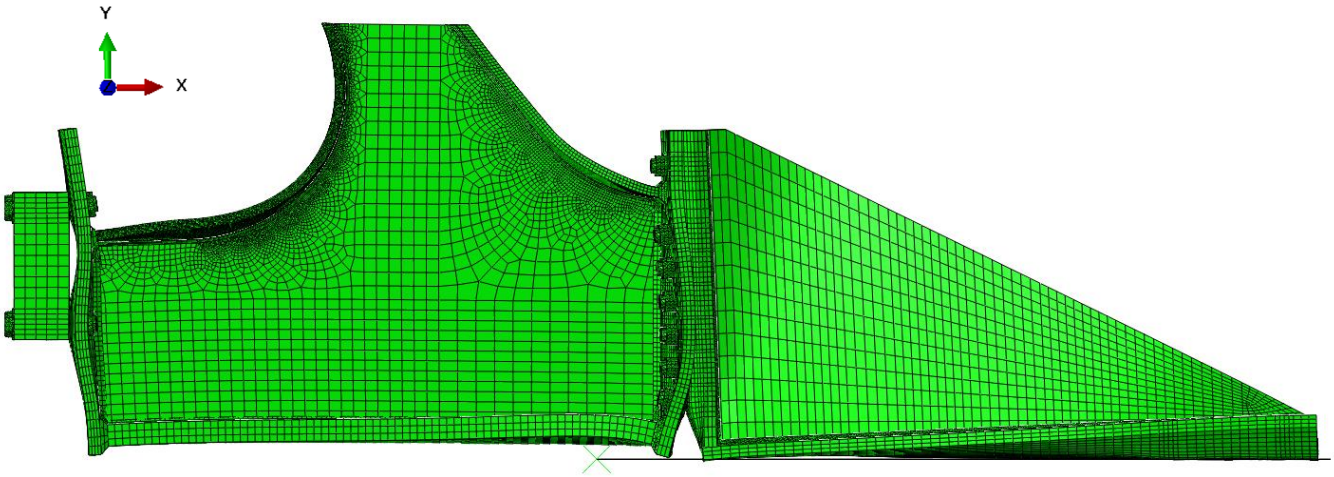

Figure 38 - FEM Deflected Shape

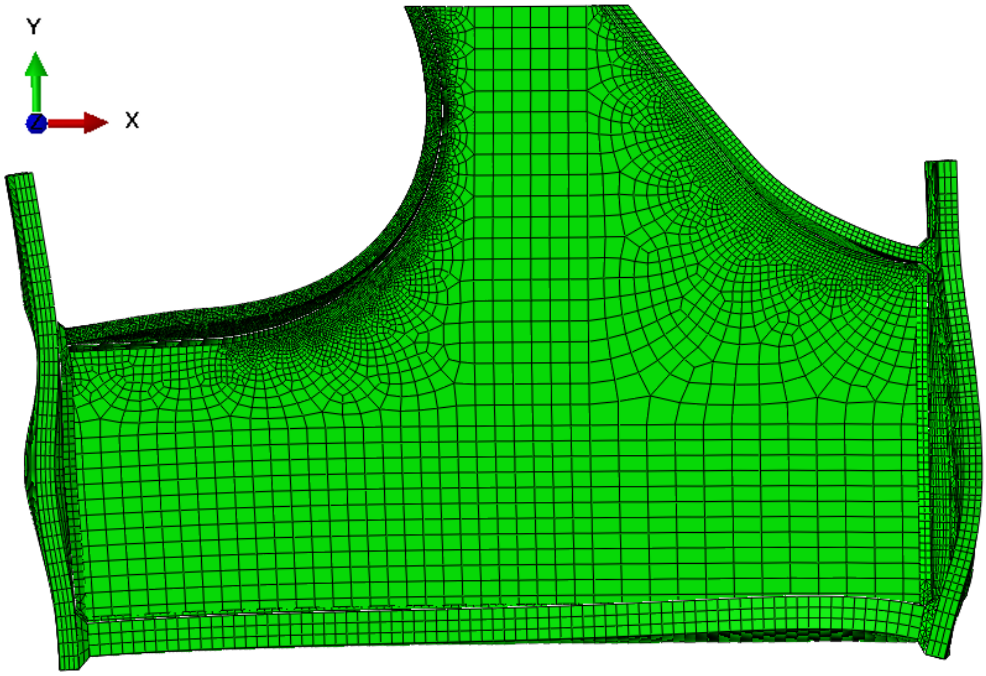

Figure 39 - FEM Specimen Deflected Shape

As a comparison, the principal stress contour of the web portion of the numerical model used in this study is shown in Figure 41 and the contour developed by HNTB during the design of the Memorial Bridge is shown in Figure 40. The magnitudes of the stresses are different, but the general shape of the contours is noted as similar.

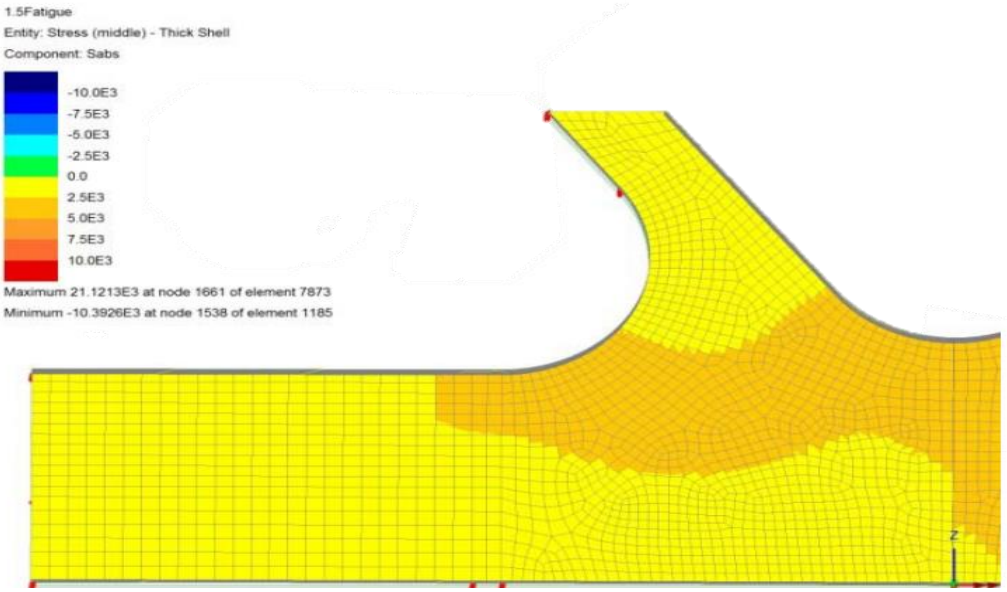

Figure 40 - HNTB Design Stress Contour

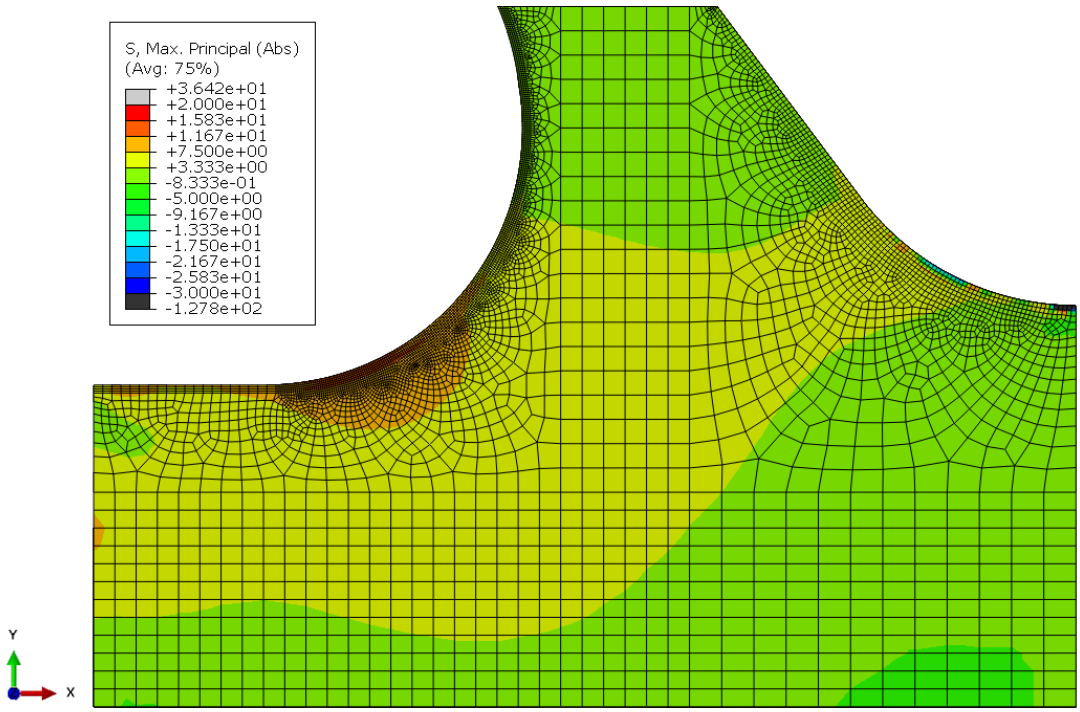

Figure 41 - FEM Web Max Principal Stress (Absolute)

Figure 42 and Figure 43 shows the absolute maximum principal stress contour in the test specimen portion of the model and the area of interest (AOI) respectively. It should be noted that some stress concentrations were located away from the area of interest, for this reason the stress contour was limited to -25 Ksi to 25 Ksi to show the relative contour without the effect of the stress concentrations in Figure 42. Additionally, the stress ranges for each of the two figures are different in magnitude despite having the same color scheme.

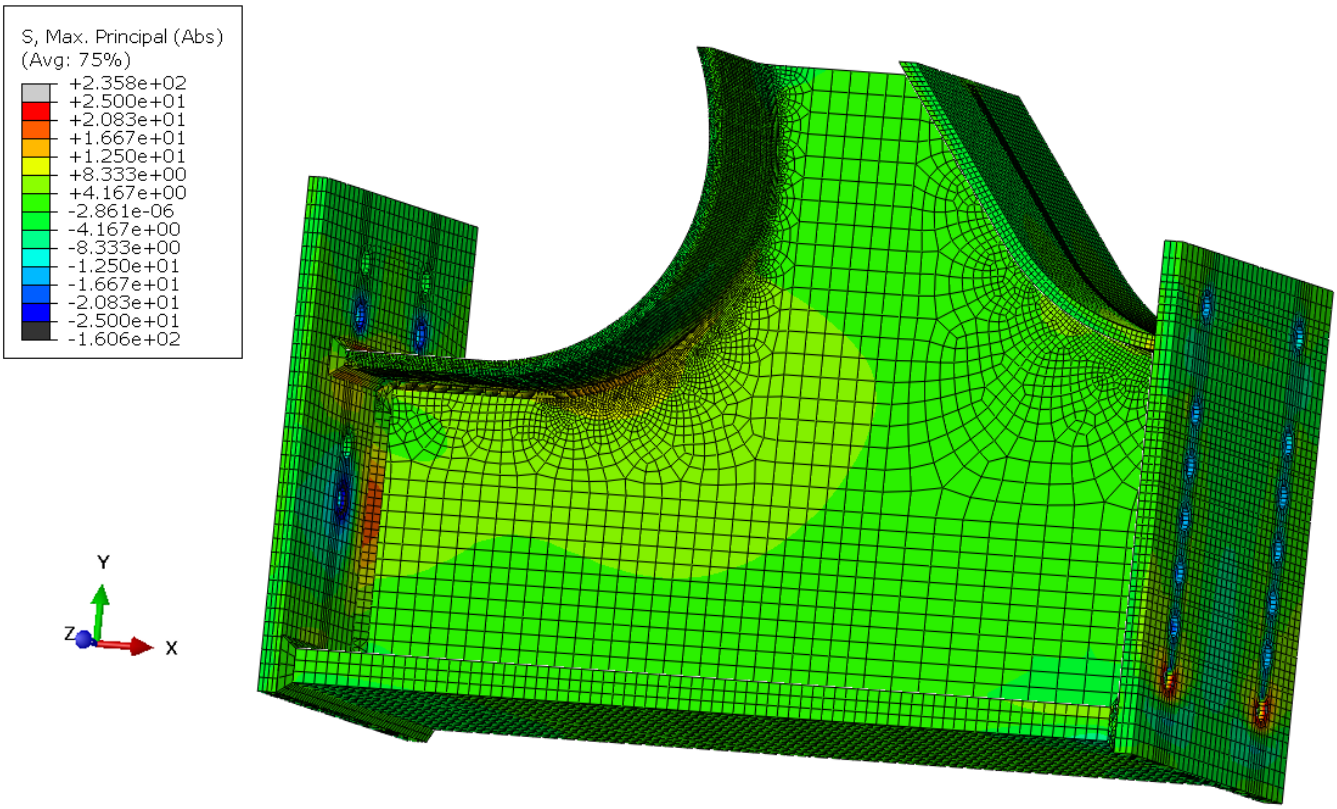

Figure 42 - FEM - Specimen Max Principal Stress (Absolute)

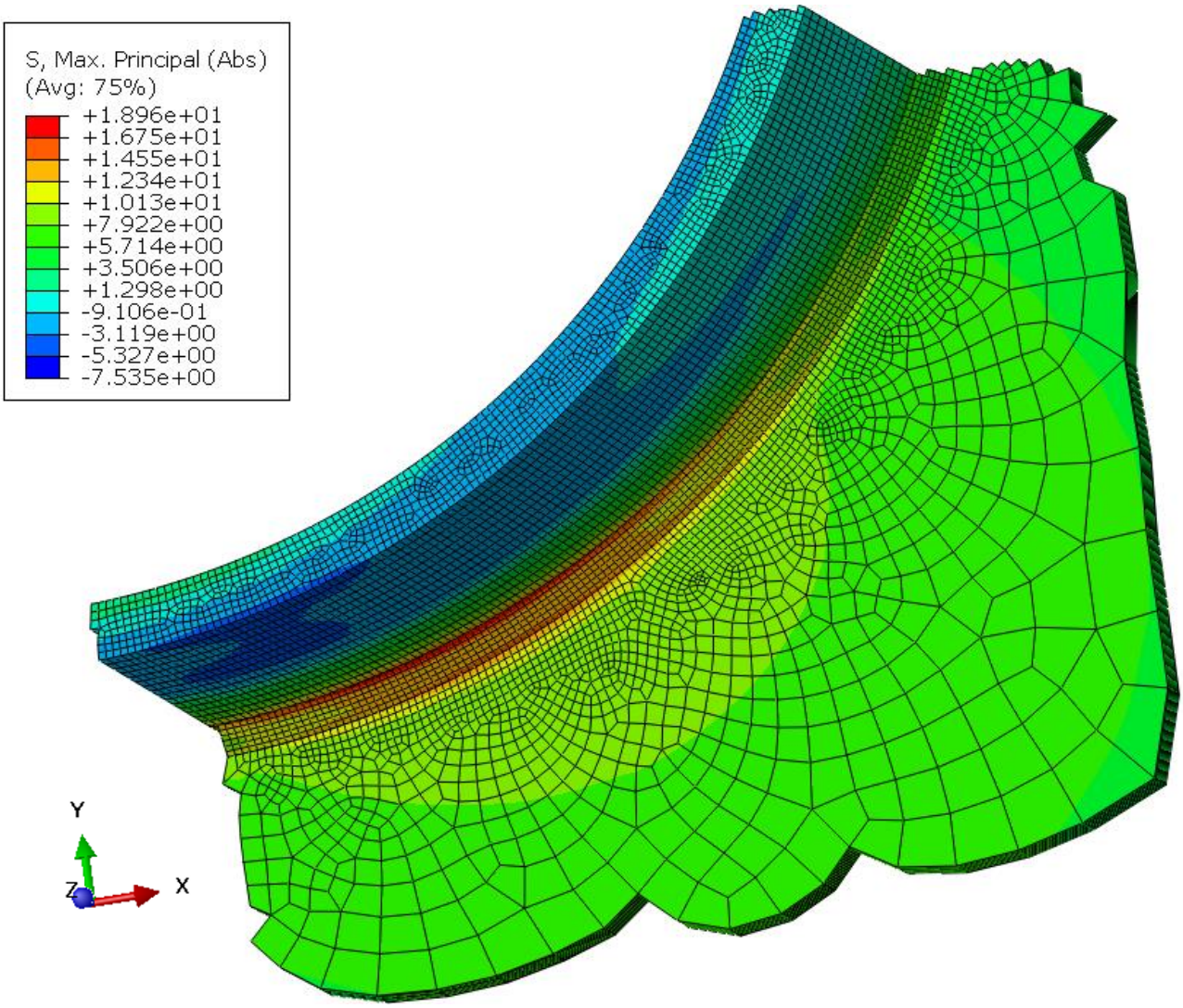

Figure 43 - FEM - AOI Max Principal Stress (Absolute)

Figure 44 and Figure 45 show the elastic strain contours in the x-direction of the overall specimen model and the area of interest respectively. In a similar fashion to the previous contours, the contour limits were set to ignore the concentrations present in areas away from the AOI in the specimen figure.

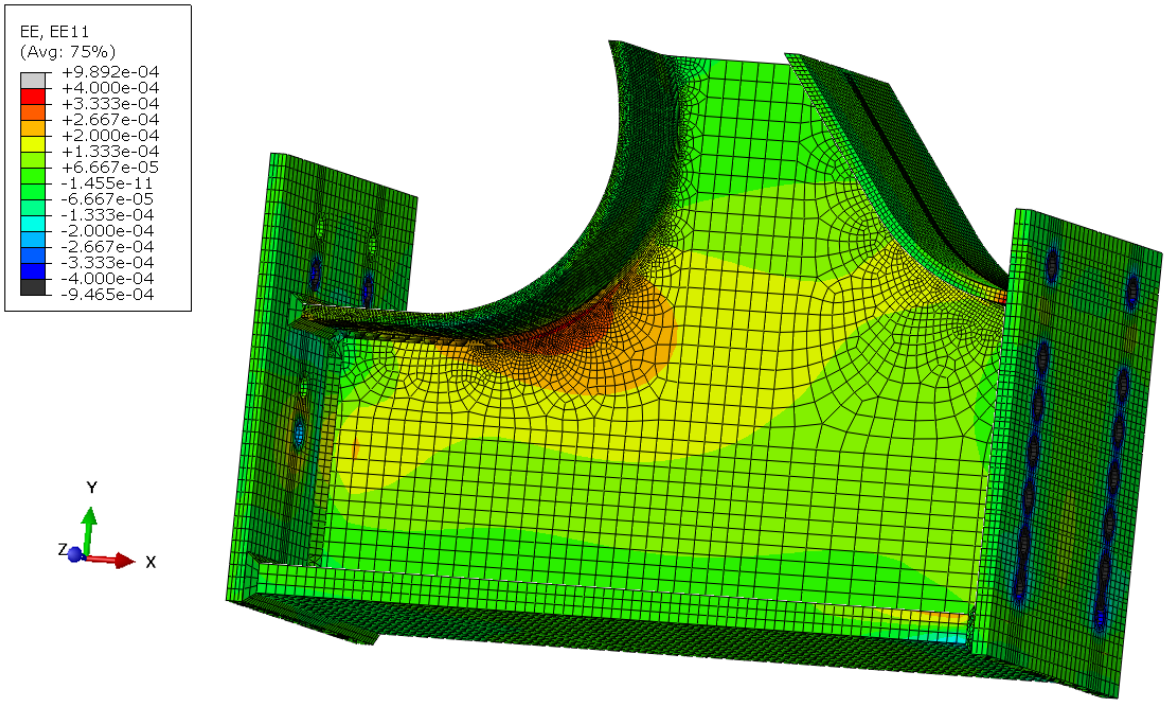

Figure 44 - FEM Specimen Horizontal Strain

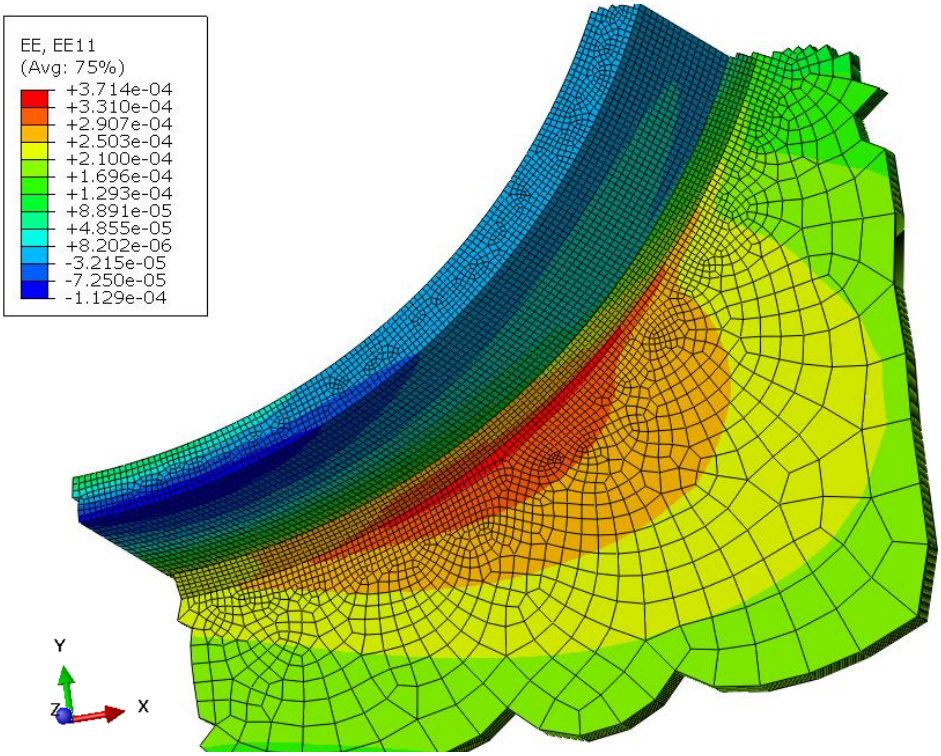

Figure 45 - FEM AOI Horizontal Strain

Finally, Figure 46 and Figure 47 show the elastic strain contours in the y-direction of the overall specimen model and the area of interest respectively, with the same caveat of limiting the contours for the specimen model to avoid concentrations.

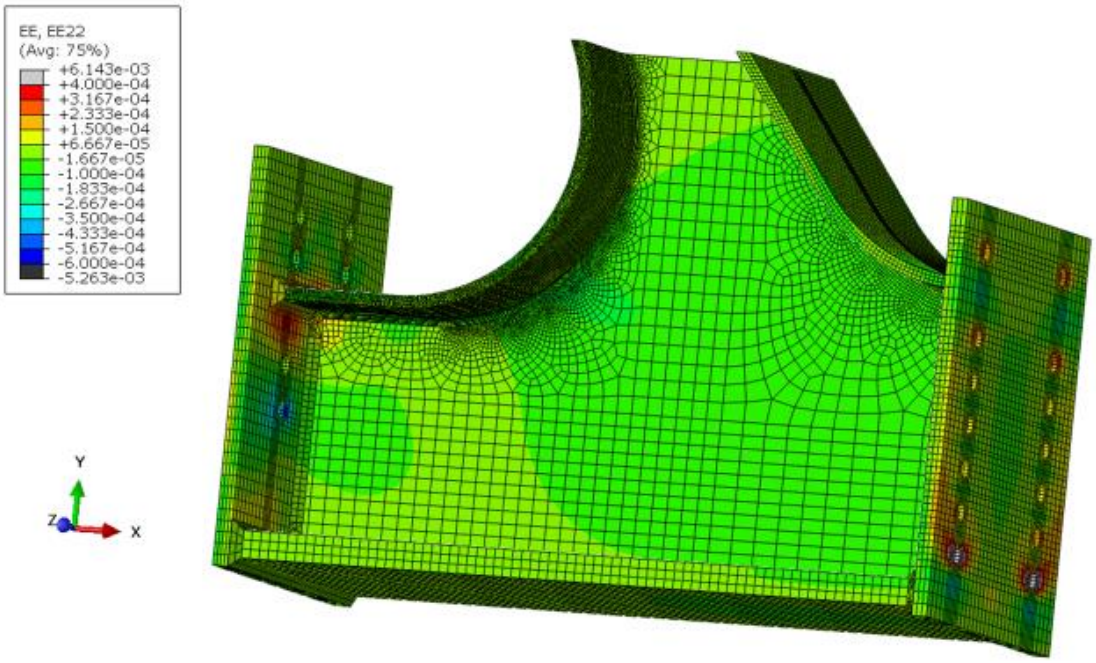

Figure 46 - FEM Specimen Vertical Strain

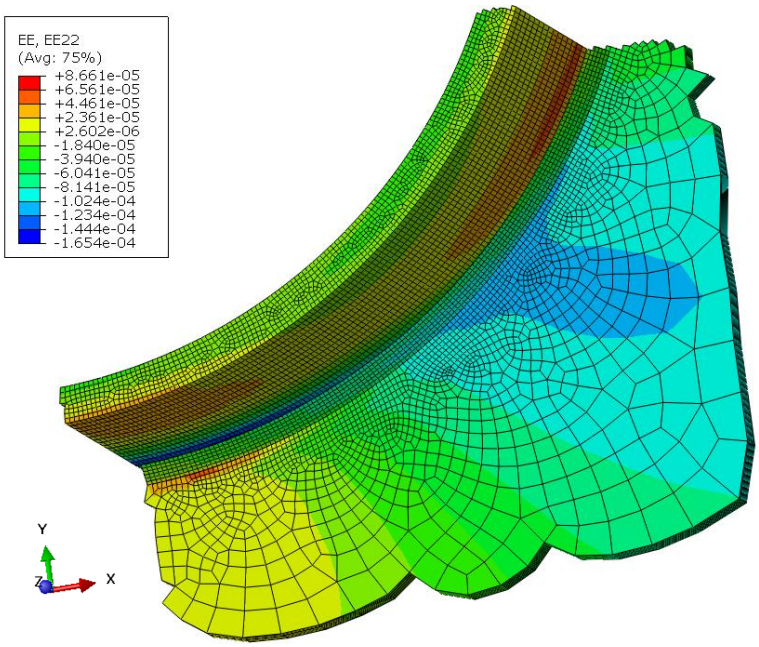

Figure 47 - FEM AOI Vertical Strain

4.4 Summary

The strains obtained from the numerical model can be compared to the measurements from the experimental fatigue test. This comparison will provide insight into how closely this model represents reality. Once the model has been verified, it can be used to estimate stresses and strains in and around the radiused fillet weld itself. This analysis will help supplement the information obtained from measurements as only strain data adjacent to the weld can be obtained experimentally.

5 FATIGUE TESTING RESULTS

This chapter will briefly reintroduce the fatigue loading protocol and reiterate the design criteria for the connection. The performance expectation will also be discussed. Next, the results from the fatigue test, in terms of measured strains from the strain gauges and the 2-D DIC in the area of interest, will be introduced and discussed. Lastly, a comparison between the measured response and the theoretical response from the numerical model will be discussed.

5.1 Introduction

The objective of the fatigue testing was to investigate the fatigue performance of the gusset-less truss connection used in place at the Memorial Bridge. Since the connection has such a unique geometry, there was no specific category for the critical fatigue location, which was the radiused weld connecting the curved top flange to the web. For this reason, the assumption was made to conservatively categorize the region of interest as fatigue category C. With this assumption, and the calculated stresses in the fatigue load case for the Memorial Bridge, the gusset-less connection is expected to have infinite life because the design stresses, approximately 4 Ksi, are well below the endurance limit of 10 Ksi for fatigue category C [1]. Therefore, to investigate the assumption, it was critical to increase the stress applied to the fatigue specimen compared to the Memorial Bridge.

The cyclic loading protocol used in this fatigue test was previously described in section 2.2, but is repeated here;

- Mean axial load applied: 55 Kip
- Cyclic amplitude: ±50 Kip
- Cyclic frequency: 3.5 Hz
- Applied function: Sine wave

With the applied loading, the numerical model predicts principal stresses of approximately 14 Ksi close to the toe of the weld. Although this stress is higher than the endurance limit for the fatigue category C, the stress predicted is better described as a hot-spot stress due to its proximity to the weld toe. Therefore, the comparison of a hot-spot stress to the S-N curves derived using nominal stresses, is considered conservative. Using this "hot-spot" stress at the weld toe and applying it to the S-N curve for the design category, the expected cycles to failure would be 1,600,000 fatigue cycles. At the time of this thesis, the specimen has undergone a total of 1,602,300 fatigue cycles.

5.2 Strain Gauge Results

The following section will present the results from the fatigue testing in terms of strain gauges in the area of interest. The strain gauge results presented will be measurements from three testing sessions spaced over the course of the overall fatigue test. The goal of showing the results in this manner is to make a comparison of the cyclic strain range applied to the specimen throughout the fatigue test. The testing periods will be labeled by the date on which they were performed;

- Test period 1: 07/17/2018, Cumulative fatigue cycles; 178,831
- Test period 2: 08/29/2018, Cumulative fatigue cycles; 880,014
- Test period 3: 10/30/2018, Cumulative fatigue cycles; 1,602,287

In terms of fatigue testing, the strain of interest is the maximum principal strain. For this reason, all comparisons to the S-N curve were using the principal strains calculated from the rosettes or obtained from the DIC. Just for the sake of comparisons, with respect to each other, the strain gauge results are shown in terms of the horizontal, diagonal, and vertical strain components.

Before the comparison between different test periods takes place, the overall structural response of the specimen in the area of interest will be presented. Figure 48 shows the horizontal strain measurements of the gauges NRW1, NRW2, and NRW4. These rosettes are the gauges that are placed along the curved weld, close to the toe of the weld. As the figure shows, the horizontal strain range increases as the measurement is taken along the weld. In other words, NRW1 had the smallest strain range while NRW4 had the largest, with 35% increase in the measured horizontal strain range between the two rosettes. Similarly, Figure 49 shows the horizontal strain components of the gauges NRW2, NRW3, and NRW5. These gauges are placed on the same path, in terms of the

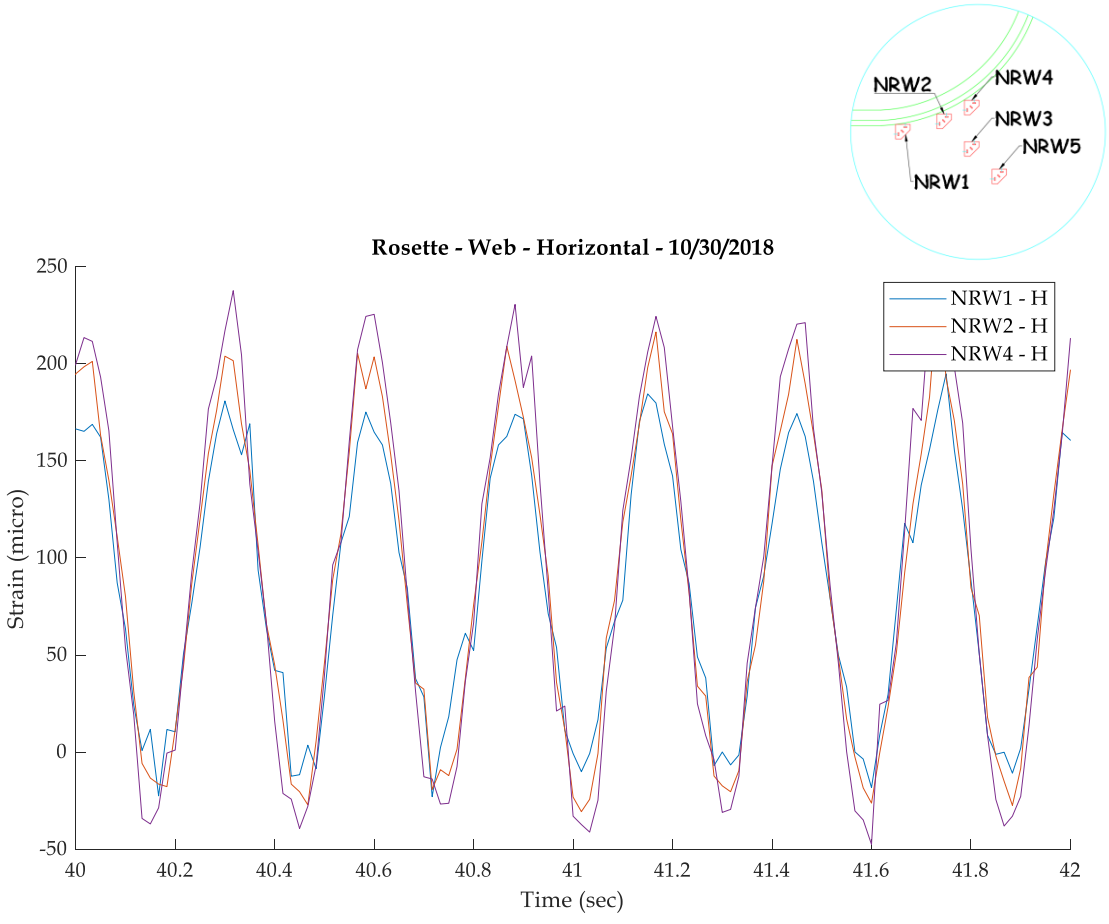

Figure 48 - Horizontal Strain Pattern Along Weld Toe

tangent from the weld toe, at varying distances from the toe of the curved weld. The pattern shown from these measurements it that as the distance from the weld toe increases, the strain range measured decreases. In this case, the reduction in the measured horizontal strain range from NRW5 compared to NRW2 is approximately 33%. Based on

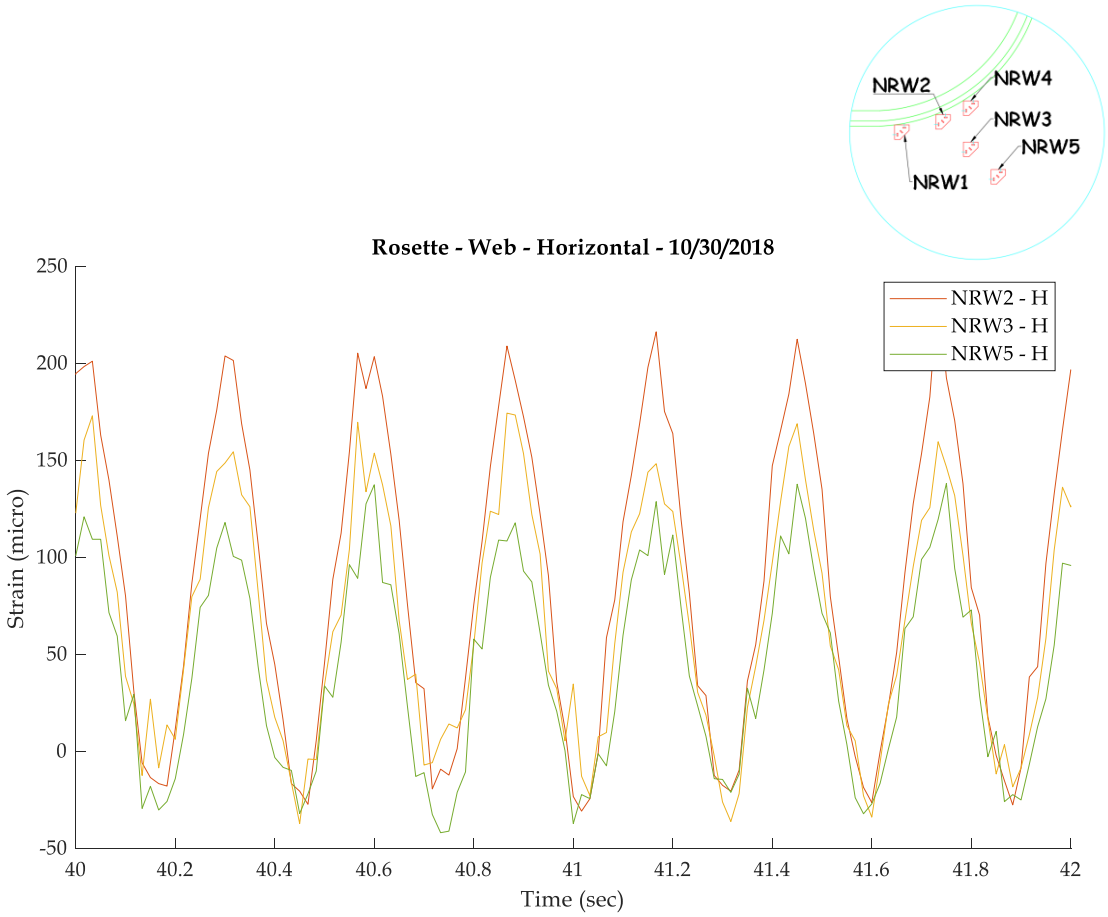

Figure 49 - Horizontal Strain Pattern Away from Weld Toe

the observed patterns, the critical location, in terms of the discrete measurements taken from the rosettes, for fatigue is NRW4. This gauge shows the highest strain range measured, as well as the highest mean strain compared to the other gauges in the area of interest. It is important to note, that this is also confirmed from the supplementary rosettes located on the South-face of the specimen. Of these rosettes, SRW4,

corresponding to the same geometric location as NRW4, is the critical gauge. It should also be noted that there are slight differences in the mean stress levels between the gauges located on the North and South faces of the specimen. Figure 50 shows a comparison between the horizontal strain component of NRW4 and SRW4. As the figure shows, the

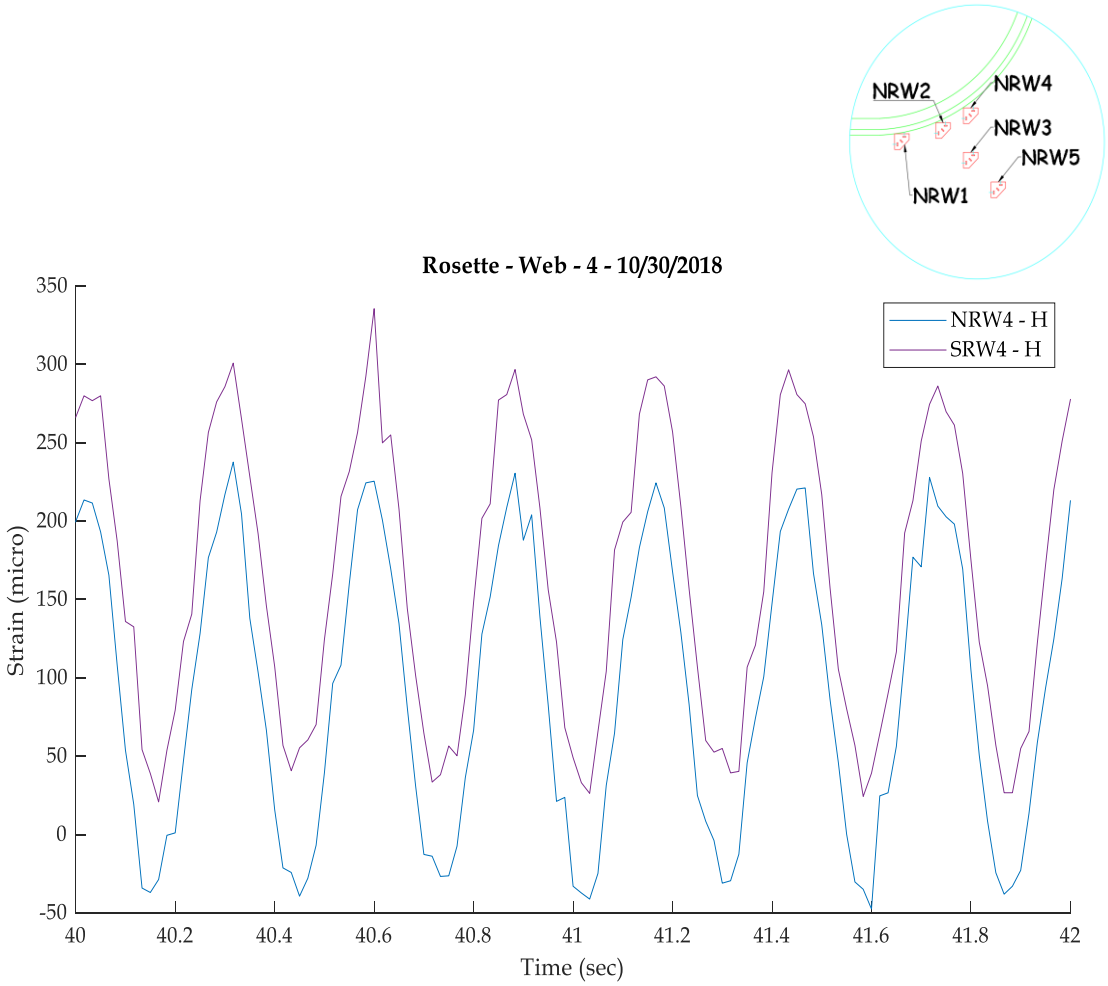

Figure 50 - North and South Comparison

magnitude of the strains measured are approximately 70 micro-strain higher different, with the South side rosette being higher. The important distinction is that the strain range is approximately identical for both gauges, there just appears to be a shift in the response based on the side that the rosette is located on. A similar pattern exists for the other rosette

comparisons between the two sides, with the shift ranging from 60 to 90 micro-strain but the range staying approximately the same.

Knowing that the critical location corresponds to NRW4, the comparison between test dates will focus on the results from this gauge. Figure 51 shows the horizontal strain

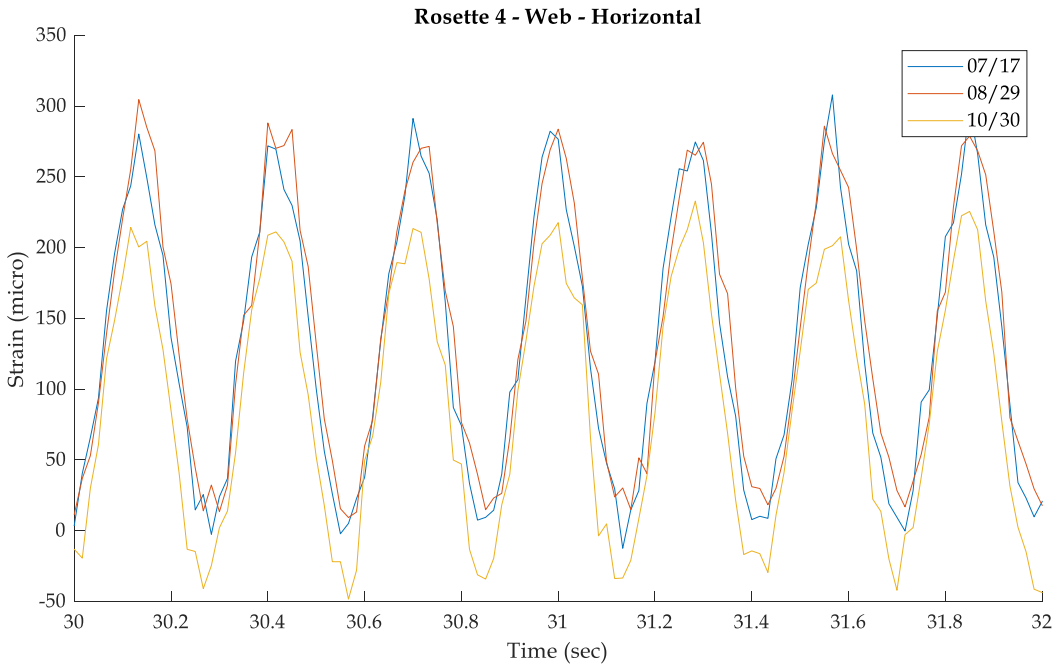

Figure 51 - Horizontal Strain, Test Interval Comparison

component of NRW4 at the three previously mentioned testing intervals. As the figure shows, the results from the first two test intervals (07/17 and 08/29) match closely, while the data from the final interval (10/30) is slightly offset from the previous. This offset is approximately 65 micro-strain, and across all horizontal components of the rosettes, the average decrease is 38 micro-strain. The average change in the range of horizontal strains is approximately 1 micro-strain, which is in the level of noise. A similar pattern can be seen in Figure 52, which shows the vertical strain component of NRW4 at the three testing

intervals. The vertical strain measured is approximately 40 micro-strain less on the final interval compared to the previous two. Across all rosettes, the average decrease in the vertical strain component is 54 micro-strain, with an average change in the vertical strain range of 6 micro-strain. This shows that there is a clear shift in the response, but the range of strains is still consistent between the tests. The pattern is similar in the final, diagonal,

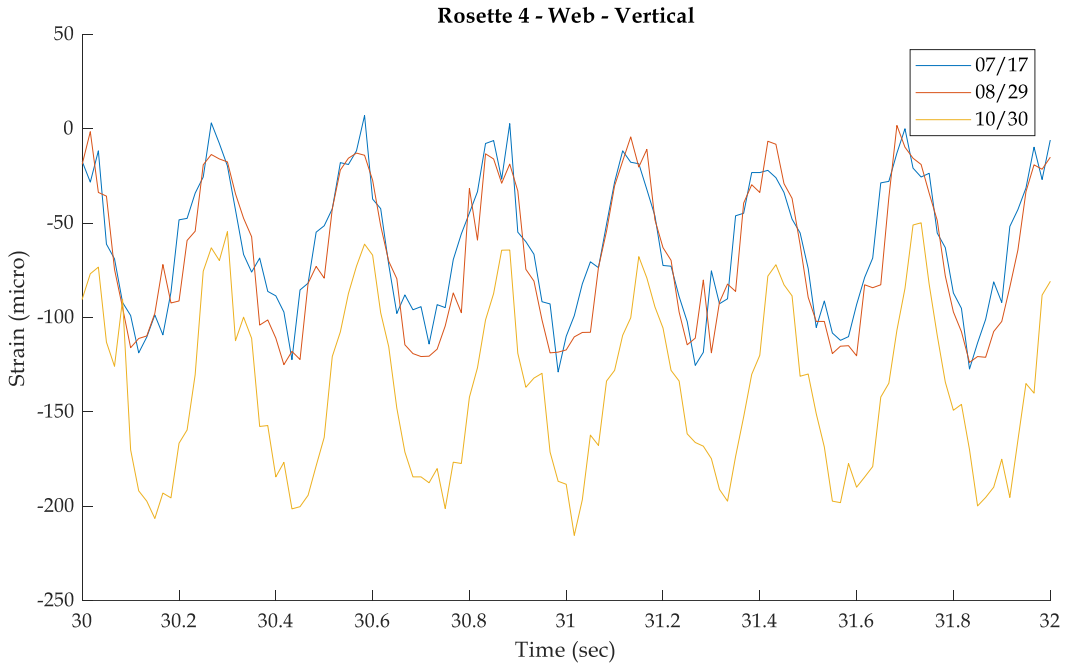

Figure 52 - Vertical Strain, Test Interval Comparison

component of NRW4, which across all rosettes has an average shift of 42 micro-strain and an average change in the strain range of 6 micro-strain. Overall there is a clear shift in the response across all the rosettes, but the range of applied strains are still consistent. In fatigue, as previously mentioned, the most influential parameter is the applied stress range, so it is very important to consistently apply the same stress range across all testing periods. Table 1 through table 5 summarize the results from the five rosettes in the area of interest across the three test periods.

Table 2 - NRW1 – Test Interval Comparison

NRW1				
Measure (με)	Date			
	07/17	08/29	10/30	Average
Max. Horizontal Strain	232	243	196	224
Min. Horizontal Strain	19	32	-15	12
Horizontal Strain Range	213	211	211	212
Mean Horizontal Strain	125	138	90	118
Max. Vertical Strain	14	2	-28	-4
Min. Vertical Strain	-60	-51	-96	-69
Vertical Strain Range	74	53	68	65
Mean Vertical Strain	-23	-24	-62	-36
Max. Diagonal Strain	186	189	140	171
Min. Diagonal Strain	-25	-19	-54	-33
Vertical Diagonal Range	211	207	193	204
Mean Diagonal Strain	80	85	43	69

Table 3 - NRW2 - Test Interval Comparison

NRW2				
Measure (με)	Date			
	07/17	08/29	10/30	Average
Max. Horizontal Strain	254	262	232	249
Min. Horizontal Strain	-9	9	-31	-10
Horizontal Strain Range	263	253	263	260
Mean Horizontal Strain	123	135	101	120
Max. Vertical Strain	2	0	-58	-19
Min. Vertical Strain	-67	-70	-128	-88
Vertical Strain Range	69	70	70	70
Mean Vertical Strain	-32	-35	-93	-53
Max. Diagonal Strain	179	166	140	162
Min. Diagonal Strain	-28	-39	-69	-45
Vertical Diagonal Range	207	205	208	207
Mean Diagonal Strain	76	64	36	58

Table 4 - NRW3 - Test Interval Comparison

NRW3				
Measure (με)	Date			
	07/17	08/29	10/30	Average
Max. Horizontal Strain	207	223	185	205
Min. Horizontal Strain	-10	10	-30	-10
Horizontal Strain Range	216	213	215	215
Mean Horizontal Strain	99	117	77	97
Max. Vertical Strain	20	34	-45	3
Min. Vertical Strain	-31	-22	-104	-52
Vertical Strain Range	50	56	59	55
Mean Vertical Strain	-6	6	-74	-25
Max. Diagonal Strain	178	187	157	174
Min. Diagonal Strain	-18	-14	-41	-24
Vertical Diagonal Range	197	201	199	199
Mean Diagonal Strain	80	87	58	75

Table 5 - NRW4 - Test Interval Comparison

NRW4				
Measure (με)	Date			
	07/17	08/29	10/30	Average
Max. Horizontal Strain	291	305	233	276
Min. Horizontal Strain	-2	17	-44	-10
Horizontal Strain Range	293	288	277	286
Mean Horizontal Strain	145	161	95	133
Max. Vertical Strain	7	-4	-48	-15
Min. Vertical Strain	-114	-120	-179	-138
Vertical Strain Range	121	116	131	123
Mean Vertical Strain	-54	-62	-114	-76
Max. Diagonal Strain	108	129	71	103
Min. Diagonal Strain	-34	-29	-78	-47
Vertical Diagonal Range	142	158	149	150
Mean Diagonal Strain	37	50	-3	28

Table 6 - NRW5 - Test Interval Comparison

NRW5				
Measure (με)	**Date**			
	07/17	**08/29**	**10/30**	**Average**
Max. Horizontal Strain	181	177	151	170
Min. Horizontal Strain	7	9	-28	-4
Horizontal Strain Range	174	168	179	174
Mean Horizontal Strain	94	93	61	83
Max. Vertical Strain	23	54	-14	21
Min. Vertical Strain	-39	-13	-83	-45
Vertical Strain Range	62	67	69	66
Mean Vertical Strain	-8	20	-49	-12
Max. Diagonal Strain	195	234	147	192
Min. Diagonal Strain	-19	13	-58	-21
Vertical Diagonal Range	213	222	205	213
Mean Diagonal Strain	88	124	44	85

In addition to the figures and tables shown here, additional plots of the strain gauge responses are shown in Appendix D.

5.3 DIC Results

This section will introduce and discuss the measurements obtained from the 2-D DIC applied to the area of interest. Unlike the previous section, only one testing period will be shown and comparisons to the strain gauge measurements will be shown. Before presenting the measurements from the post-processed images, a brief overview of the methodology used, and the parameters selected for post-processing will be provided. Firstly, the software used for the post-processing of the raw image files in this study was VIC-2D 2009 [35]. Within this software there are a few key variables that must be chosen

to provide a consistent and accurate correlation. The first is the subset size, or the area used to track the pixel movement across successive images. The size of the subset is directly related to the spatial resolution of the analysis, in which as the subset size increases, spatial resolution is lost due to the averaging effect of the subset tracking. Additionally, the step size factors into the resolution and run-time because it controls how often, in terms of pixels, the correlation is performed. If a higher step-size is chosen, the correlation will be performed less often. Next, the correlation options must be chosen in terms of interpolation, correlation criterion, and subset weights. A higher order interpolation provides more accurate results at the cost of analysis time. The correlation criterion is the statistical method to determine a match for the tracking, the default of normalized squared differences is suggested due to it not being affected by lighting changes. The subset weights determine how the movement within a subset is weighted for the analysis, either uniformly across the subset meaning that each pixel has the same effect, or center-weighted meaning as the pixels get closer to the edge of the subset their movement has less effect on the overall movement. Lastly, the strain tensor is chosen along with the filter size and type. The strain tensor defines the calculation type, while the filter options how the data is averaged and over what area. The key parameters used in this study were determined through a sensitivity analysis and are as follows;

- Subset-size – 69,
- Step-size – 8,
- Interpolation - Optimized 8-tap

- Correlation criterion – Normalized squared differences
- Subset weights – Gaussian weights (center-weighted)
- Strain tensor – Lagrange
- Strain filter size – 33
- Strain filter type – Decay filter

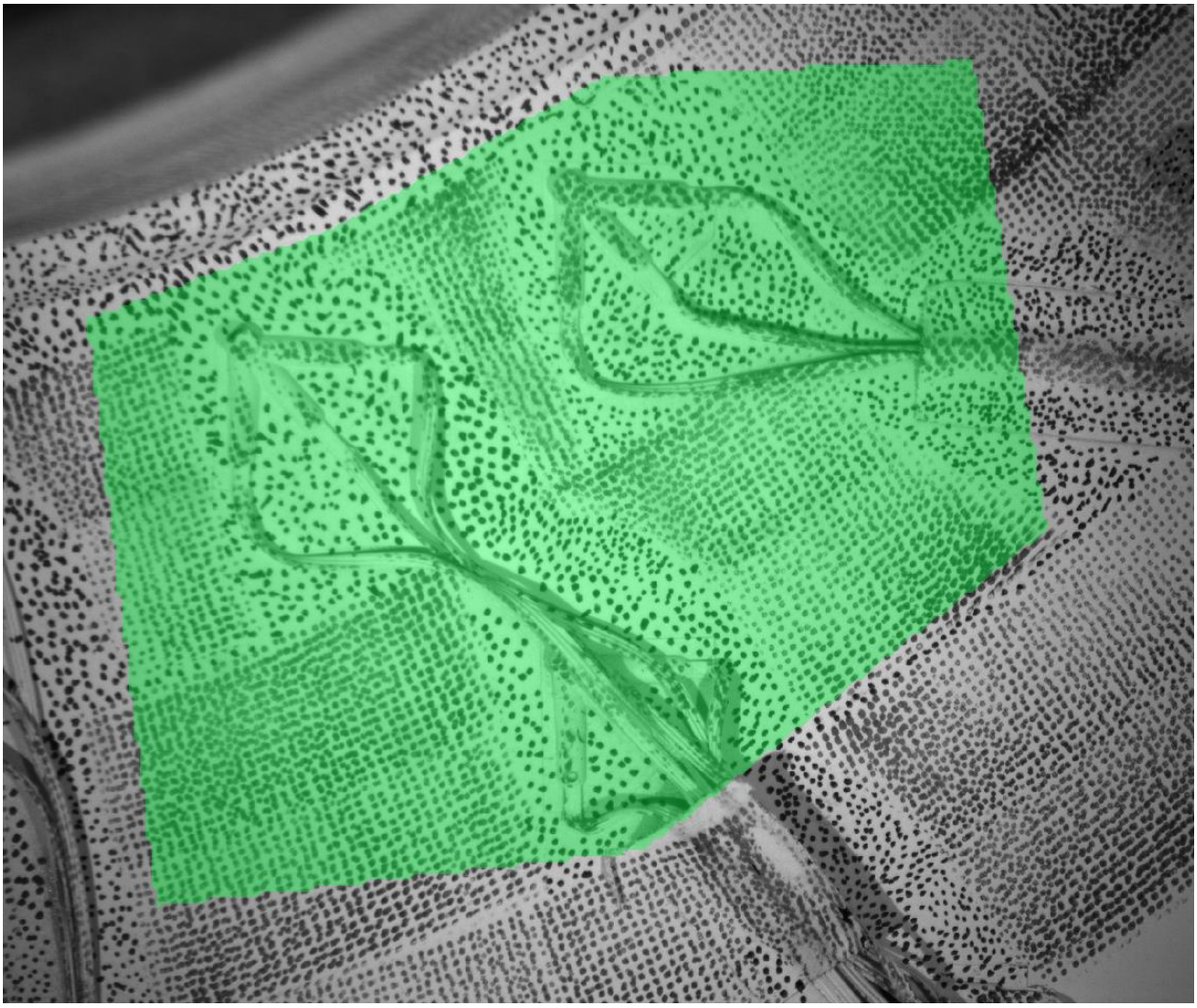

Figure 53 - Analysis Area of Interest - DIC

Figure 53 shows the defined area of interest, shaded in green, in the VIC-2D software. Note that the area of interest that was defined performs an analysis on or around the

strain gauges and their wires, for this reason, care must be taken in extracting data away from these regions to avoid any false measurements stemming from loose wires or out-of-plane geometry caused by the raised surfaces of the strain rosettes, their coating and

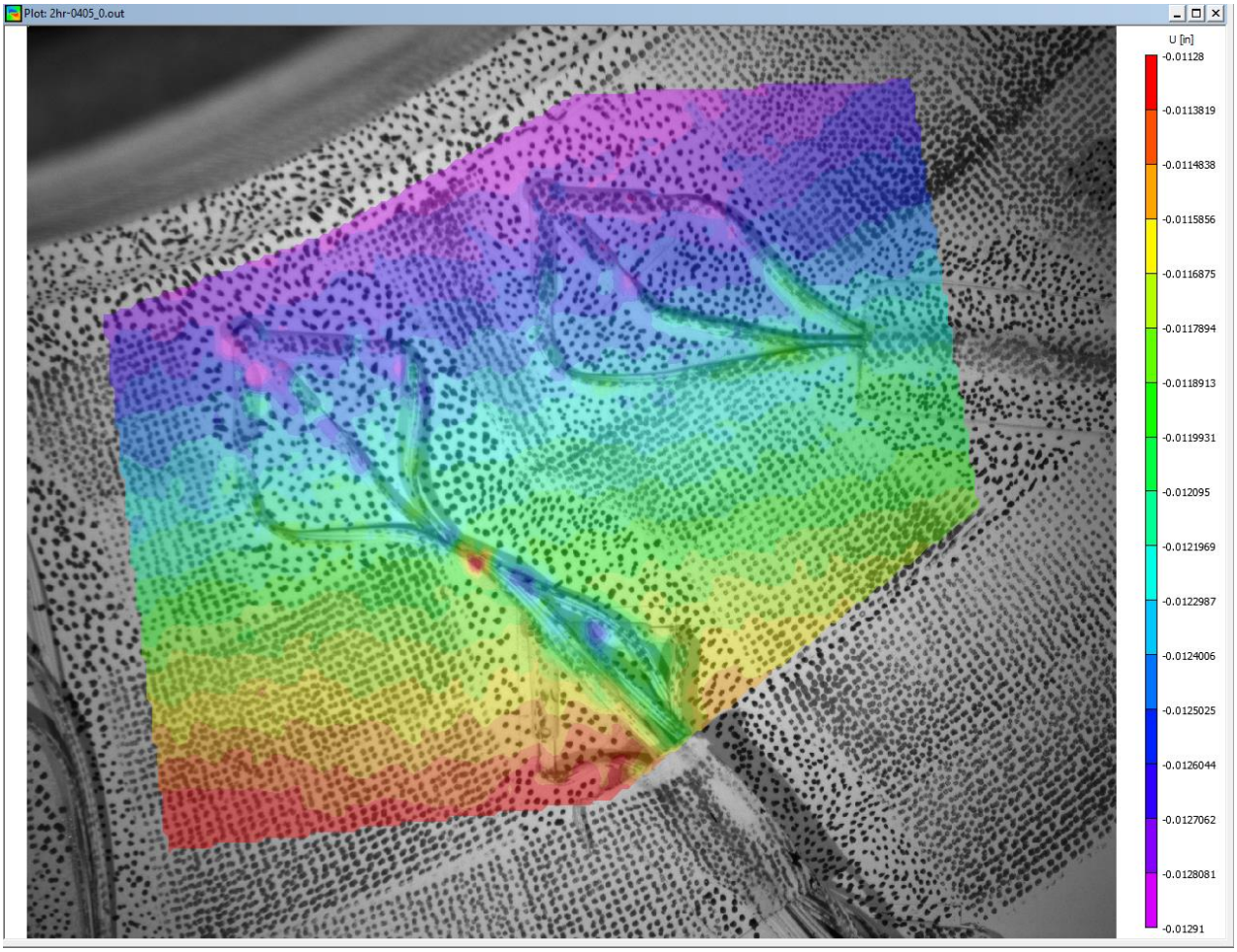

Figure 54 - Horizontal Displacement DIC Contour

backing plates. Figure 54 shows a sample contour, in this case the horizontal displacement from an image during the cyclic loading. Note the point on the strain gauge wire in which the contour has a discontinuity. This is likely due to the out-of-plane geometry of the wire as well as the lack of speckle pattern applied to the wire. This causes the program to be unable to accurately track that area. Figure 55 shows the locations of extraction points DIC 1 through DIC 5 along the curved weld and Figure 56 shows the

plots principal strain at each location. These locations will be used for comparison between the DIC and the finite element model in section 5.4.

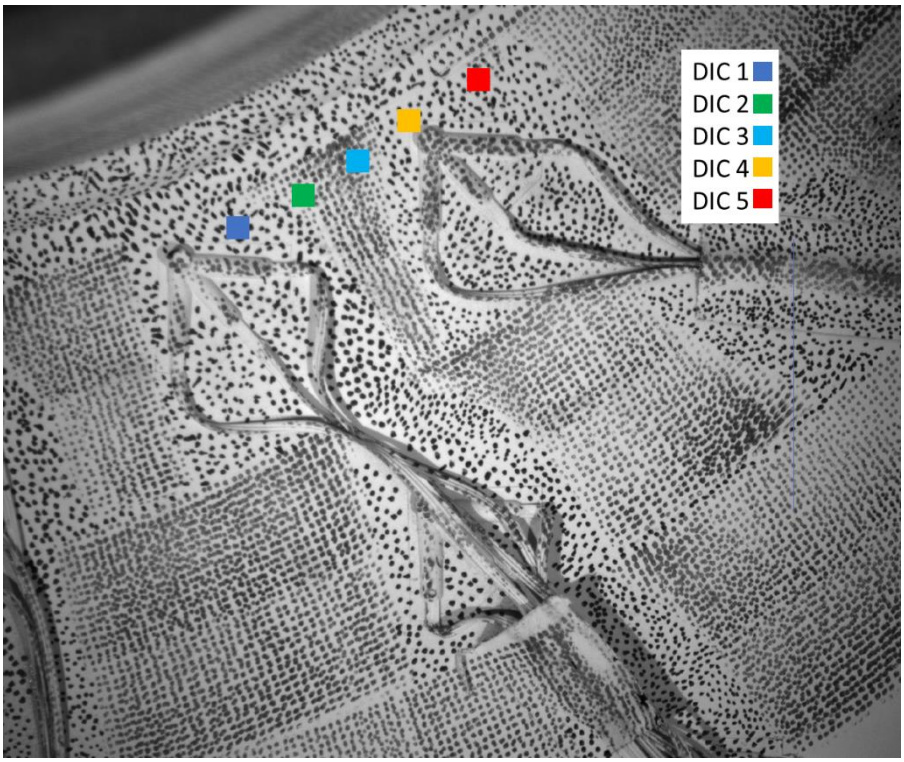

Figure 55 - DIC Comparison Locations

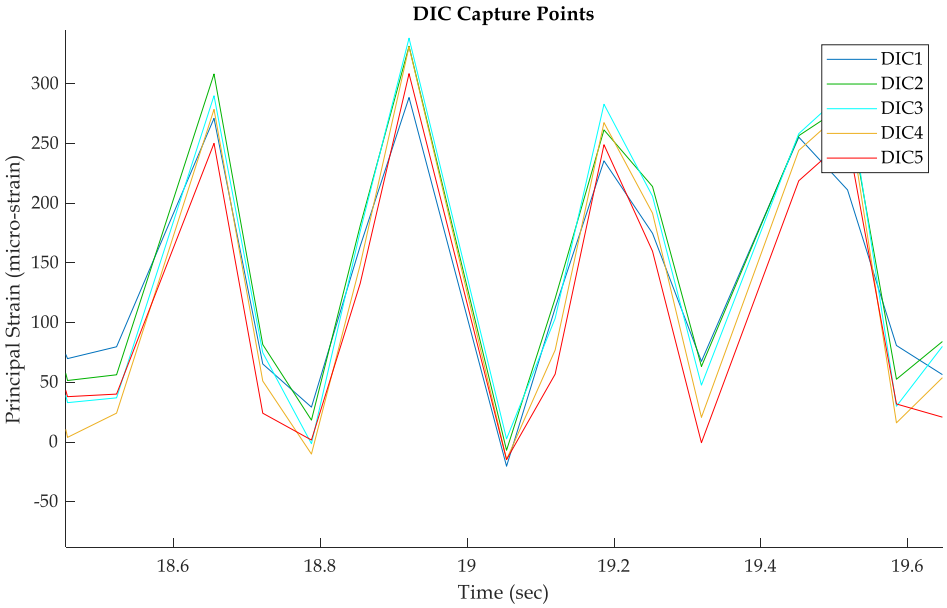

Figure 56 - DIC Response Along Weld

5.4 Measurement Comparison

This section will present the comparison between the measured response from the 2-D DIC and two of the relevant strain gauges. This comparison is provided to verify the two measurements against one another, but mainly to verify the strain measurements from the 2-D DIC since the strain gauges generally provide a more reliable measurement. If the DIC matches closely to the strain gauges, it shows that the measured response of the DIC is accurate. Additionally, comparisons between both measured responses, from the DIC and the strain gauges, will be compared to the results of the numerical model.

Table 7**Error! Reference source not found.** shows the comparison of principal strains measured from strain gauges NRW2 and NRW4, and points from the DIC analysis near the base of the rosette. As the table shows, the DIC measurements match the strain gauge measurements well. It should be noted that the verification using NRW3 was not done due to the wires obstructing the base of the rosette where the DIC measurement would be taken.

Table 7 - DIC and Strain Gauge

Location	Data Source	Max Principal Strain (με)
NRW2	**DIC**	249
	NRW2	268
	Difference	7.6%
NRW4	**DIC**	296
	NRW4	301
	Difference	1.6%

The next comparison is between the numerical model and the strain rosettes, shown in Table 8. The locations of the strain rosettes were identified in the numerical model and the principal strain of the surface element corresponding to that location was captured. The table shows that there is some variability in the comparison, but the overall measured response matches the FEA results, with an average difference of 6.4%. It should also be noted that this model has not been calibrated to match the response, as previously mentioned, it is a blind model.

Table 8 - Strain Gauges and FEA

Location	Data Source	Max Principal Strain (με)	Equivalent Stress (Ksi)
NRW1	**Strain Gauge**	236	6.84
	FEA	250	7.26
	Difference	6.2%	-
NRW2	**NRW2**	268	7.76
	FEA	296	8.59
	Difference	10.7%	-
NRW3	**NRW3**	236	6.84
	FEA	242	7.02
	Difference	2.6%	-
NRW4	**NRW4**	301	8.72
	FEA	298	8.65
	Difference	0.8%	-
NRW5	**NRW5**	227	6.57
	FEA	200	5.80
	Difference	11.8%	-

The final comparison is between the DIC locations 1-5, and the FEA results. Using the same method as the strain gauge comparison, the locations of the DIC points were identified in the numerical model and the principal strain was extracted. The comparison, Table 9 shows that there is some variability but the DIC matches closely to the numerical results from the FEA, with an average difference of 3.7%.

Table 9 - DIC and FEA Comparison

Location	Data Source	Max Principal Strain (με)	Equivalent Stress (Ksi)
DIC 1	**DIC**	309	8.96
	FEA	317	9.20
	Difference	2.7%	-
DIC 2	**DIC**	315	9.13
	FEA	320	9.28
	Difference	1.7%	-
DIC 3	**DIC**	335	9.73
	FEA	316	9.15
	Difference	5.9%	-
DIC 4	**DIC**	338	9.81
	FEA	312	9.05
	Difference	7.8%	-
DIC 5	**DIC**	307	8.90
	FEA	305	8.86
	Difference	0.5%	-

5.5 Summary and Discussion

In summary, the two experimental results were compared to one another and were found to have a similar behavior. It should be noted that since the comparison was limited to two strain rosette locations, it is difficult to draw conclusions about the measurements compared to one another. Comparisons were also made between the FEA and the strain rosettes. This comparison showed there was some variation between the calculated response of the FEA and the measured response from the strain rosettes, but the overall difference was 6.4% on average. Lastly, a comparison between the DIC measurements and the FEA was performed. This comparison showed a relatively close match between the two, with an average difference of 3.7%.

In terms of fatigue testing results, the measured strain in the specimen indicate that the corresponding stresses are below the theoretical endurance limit for the design fatigue category as expected. Since the model is matching the response well, the stresses can be extrapolated to the weld using the numerical results. Based on this extrapolation the maximum principal stress applied near the toe of the weld is approximately 14 Ksi. As previously mentioned, the predicted fatigue life of this specimen, considering the design assumptions and the 14 Ksi applied stress, was 1,600,000 cycles. In terms of damage, in this study, fatigue failure, or damage, is defined as a visible crack. These cycles have been applied and no damage has been detected in the specimen. There are a few potential conclusions that can be drawn from these results;

1. Using the hot-spot stress close to the toe of the weld to predict life using the AASHTO S-N curves, which were derived for the nominal stress, is not an appropriate method to predict life for this scenario.
2. The design assumption of a category C fatigue detail was conservative, and the endurance limit of the actual fatigue specimen may be higher than expected.

6 RESIDUAL STRESSES

This chapter will focus on the investigation of residual stresses with regards to the gusset-less connection fatigue sample. A brief overview of the importance of residual stresses regarding fatigue will be provided and the locations of interest will be introduced. Additionally, the hole-drilling strain gauging method will be discussed along with the measurement procedure and instrumentation used in this study. Next, the calculation method will be introduced. Finally, the residual stress results will be shown and discussed.

6.1 Importance of Residual Stresses

Residual stresses are complex, sometimes difficult to measure, and often overlooked in terms of civil engineering applications, but they have a significant influence in fatigue performance nonetheless. As previously mentioned, the variables with the largest effect on fatigue performance are the stress range, the mean stress, and the initial stress state, or the residual stresses. Among those, the mean stress and residual stresses have a comparable influence on the performance. It is often said that the residual stresses can be thought of, in terms of fatigue performance, as an addition to the mean stress state. Since the residual stresses are present in the material, the actual mean stress state that the material is in is the sum of the mean applied stress and the residual stress from fabrication.

In most cases, at least when using the AASHTO LRFD Bridge Code [20] it is considered acceptable to overlook the residual stresses. Since the S-N curves used for the

fatigue design of welded steel were empirically created using weld test data it is mentioned that residuals were considered, without measurement, because all test samples would have similar levels of residual stress. Therefore, it is implied that the residual stresses are built into the S-N Curve. This is acceptable when the design matches the assumption made in the making of the code, but for complex and innovate designs such as the Gusset-less connection, those assumption may not hold true. Specifically, the residual stress state of the Gusset-less connection is unique due to the cold-bending of the flanges as well as the multi-pass welds that were used to fabricate this built-up member, and finally the sand-blasting and metallization to coat the steel.

Given the complex nature, as well as the varying sources, of the residual stresses, it was decided to investigate multiple locations along the fatigue specimen. The exact locations will be shown in section 6.4 when discussing the results of the residual stress measurements. Another important decision made was to take the measurements while the specimen was installed into the test setup as well as before the specimen was installed. This was done for three reasons;

1. The installed scenario would be more representative of the actual stress state of the Gusset-less connection.
2. This would decrease the chances of effecting the results of the fatigue test by potentially altering the test setup during multiple installations of the specimen.
3. Taking measurements before and after bolting can show the effect of the bolting on the residual stresses.

When the measurements are taken with the specimen loaded, due to the bolting and dead-loads, the measurement taken are better described as the total stress state rather than the residual stress state.

6.2 Hole-Drilling Method

The method used to measure the residual stresses in this study was the Hole-Drilling, Strain Gauging method. In this method, a specialized strain rosette is attached to the specimen and a small hole is drilled in the center of this gauge, making it a "semi-destructive" method due to relatively small defect introduced. The removal of material creates a free surface allowing the residual stresses to be locally relieved and the adjacent strain surface relieved is measured with the strain rosette. The surface strains relieved at the location of the gauges are then mathematically converted to residual stresses through geometric and material relationships. This mathematical relationship will be explained in detail in section 6.3, but it is important to note that this method assumes a linear-elastic relationship.

Within the hole-drilling method, there are a few different types of analysis, each with their own assumptions and limitations. The most common variants are the through-hole analysis and the blind-hole analysis. The through-hole analysis, as the name suggests, is a method where the hole is drilled completely through the thickness of the specimen. The main drawback of this method is that it is limited to "thin" workpieces where the exact thickness is limited by the geometry of the strain gauge used. This is due to the geometric relationship between the stresses measured at a depth and the strain

relieved at the surface. As the hole depth increases, the influence of the stresses in the workpiece are less and less on the strain measured at the surface. The other method is the blind-hole analysis, where a shallow, relative to the overall thickness, hole is introduced, and surface strain measurements are taken incrementally with respect to the depth. This method is limited to "thick" workpieces, where the thickness allowed is dictated by the strain gauge geometry. The blind-hole analysis allows the user to compute a stress profile that varies with depth. Due to the relatively large thickness of the specimen, and the non-uniform nature of the residual stresses, the blind-hole analysis was used in this study.

The drilling operation was performed with the RS-200 Milling Guide from Micro-Measurements. The overall configuration, shown in Figure 57, consists of four main components; the milling-guide base assembly, a microscope, a high-speed air turbine,

Figure 57 - Drilling Assembly

and an adjustable, depth-setting, micrometer. In addition to these main components there are additional parts to aid in the drilling process such as nylon collars, a spring assembly, and lighting assembly.

The strain rosettes used in this study were the EA-XX-062RE-120 and the CEA-XX-062UL-120, shown in Figure 58 [36].

GAGE PATTERN AND DESIGNATION Insert Desired S-T-C No. in Spaces Marked XX. See Note 1.		RES. IN OHMS	DIMENSIONS (inch / millimeter)					
			GAGE LENGTH	GRID CTR'LINE DIA.	TYPICAL HOLE DIA. Min.	TYPICAL HOLE DIA. Max.	MATRIX Length	MATRIX Width
EA-XX-062RE-120 EA-XX-062RE-120/SE		120 ± 0.2% 120 ± 0.4%	0.062 1.57	0.202 5.13	0.06 1.5	0.08 2.0	0.42 10.7	0.42 10.7
			Most widely used RE pattern for general-purpose residual stress measurement applications.					
CEA-XX-062UL-120	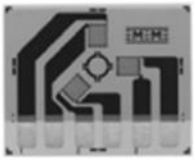	120 ± 0.4%	0.062 1.57	0.202 5.13	0.06 1.5	0.08 2.0	0.50 12.7	0.62 15.7
			Fully encapsulated with large copper-coated soldering tabs. Same pattern geometry as 062RE pattern.					

Figure 58 - Strain Rosette Information [36]

The strain gauges were wired in a quarter-bridge configuration using the same strain recording devices mentioned in section 2.3. Both rosette types have the same gauge geometry and pattern, the difference is that the EA gauge is not encapsulated and does not have copper solder tabs which reduces the overall size of the rosette. With these gauges, the assumption of a "thick" workpiece is valid if the thickness is a minimum of 5.13 mm. The acceptable range of hole diameters is between 1.5 mm and 2.12 mm [30] and the suggested hole-depth is 2 mm, with strain measurements taken in 0.05 mm depth increments [37]. It should be noted that only the first 1 mm of depth is used for stress calculations, but the behavior of the strain profile is of interest for determining if the

uniform analysis can be performed instead of the non-uniform analysis. With these geometric limitations, the diameter of the tungsten carbide inverted-cone cutting head used was 1.6 mm. When using the plunging method, this results in a hole diameter of approximately 1.66 mm. When using the orbital method, the measured hole diameter was approximately 2.05 mm. It should be noted that the offset of the cutting head was not measured, it was adjusted using trial and error until the desired hole diameter was achieved.

A general procedure [37] for performing residual stress measurements with the RS-200 milling guide is as follows;

1. Prepare the surface of the workpiece for the strain gauge and the milling guide. This consists of sanding an area that will be large enough for the specialized strain rosette and the three swivel pads for the milling guide. After sanding, the area should be cleaned with a degreaser.
2. Attach the specialized rosette at the location of interest. The method for attaching the rosette is the same as listed in section 2.3, the only difference is that care should be taken to align the grids of the rosette with the directions of interest.
3. Test that the strain rosette is functioning, and the strains are zeroed.
4. Position the milling-guide base assembly such that the center of the journal hole is approximately centered over the strain rosette. Once it is in a

satisfactory position mark the locations of the swivel pads on the workpiece.

5. Adhere the swivel pads to the workpiece.
6. After bonding the swivel pads, level the milling guide such that the guide is perpendicular to the workpiece surface while keeping the guide as close to the surface as possible. Note: on curved surfaces care should be taken to ensure that it is as close to perpendicular as possible.
7. Use the microscope assembly to align the cross-hairs with the target on the specialized strain rosette. Great care should be taken to ensure that the cross-hair of the microscope is in the center of the target on the rosette. Any eccentricity can have a significant effect on the stress calculations.
8. At this point, the strain rosette should be checked again to ensure that no wires became disconnected during the installation process. Once the drilling has begun any measurement error can render the results useless.
9. Install a new tungsten carbide cutter into the air-turbine collet. At this point the cutter should be offset from the center the appropriate distance to create the desired hole diameter while using the orbital drilling method[1]. If the plunging method[2] is used, the cutter should be centered.

[1] The orbital drilling method uses an offset cutting head. There are two steps in the drilling process; 1) advancing to the desired depth increment and 2) rotating the turbine one full revolution within the journal hole. This allows the cutter to remove material with the sides instead of the face, resulting in a cleaner cut.
[2] The plunging method uses a centered cutting head. The cutting is done in one step by advancing the cutting head to the desired depth. This results in a rougher cut.

10. Install the anti-rotation adapter and micrometer over the journal hole. The micrometer should be adjusted to read zero-depth.
11. Insert the air-turbine into the journal hole and position the nylon collar such that the cutting head is just above the gauge. It is easiest to lower the turbine assembly into the hole until contact with the rosette is made and then pull it back out very slightly before tightening the collar.
12. With the turbine in place, install the spring assembly and attach the air supply to the turbine.
13. Establish "zero-depth", or the depth setting of the micrometer at which the cutting head cuts through the gauge backing but not the workpiece surface. This should be done by supplying the air-turbine with air while advancing the turbine downward, very slowly, with the micrometer. Great care should be taken to use the smallest micrometer increments possible to ensure minimal drilling of the workpiece surface. This is a critical step because the calculations are highly dependent on the depth of the hole with respect to the surface when the strains relieved are measured.
14. Once zero-depth is established, the strains should be recorded and noted as the strain measured before any material removal.
15. While powering the turbine, advance the micrometer the appropriate increment, being sure to rotate the turbine within the journal hole after an increment. Note: when using the orbital drilling method, the desired

measurement increment should be sub-divided into smaller increments in which the drill is orbited.

16. Once the appropriate depth increment is reached, stop the air flow to the turbine and allow ~10 seconds before recording the strain for ~10 seconds and noting the current hole depth based on the micrometer.
17. Repeat step 15 and 16 until the desired hole depth is achieved.
18. Remove the turbine assembly and use the microscope assembly to visually inspect the hole, making a note of the final diameter.
19. Remove the strain rosette by lifting a corner with a blade and then peeling it back by hand. This step serves as a check on the bond strength of the gauge to ensure there was no significant debonding.

The procedure is designed to produce accurate and consistent measurements of the surface strains relieved from the drilling process while also checking for any potential errors in the experiment. Generally, the biggest source of error is the skill of the operator [38] performing the hole-drilling and measurement operations, therefore great care should be taken in this procedure.

6.3 Blind-Hole Residual Stress Calculations

In this research, as previously stated, the method for measuring residual stresses is the blind-hole method. Within the blind-hole method, the calculations are carried out assuming a non-uniform stress distribution through the thickness using the integral method. The conversion between measured strains relieved on the surface, in proximity

to the drilled hole, and stresses through the depth of the hole is dependent on many factors. Some of the more prominent factors are listed here; the geometry of the strain gauge used, the geometry of the drilled hole, the material properties of the workpiece, and the analysis method used.

The first step in these calculations is to convert the measured strain vectors, from the different rosette grids, into combination strain vectors which serve to simplify the calculations and work in a local coordinate system. Figure 59 shows the layout of the grids on the strain rosette.

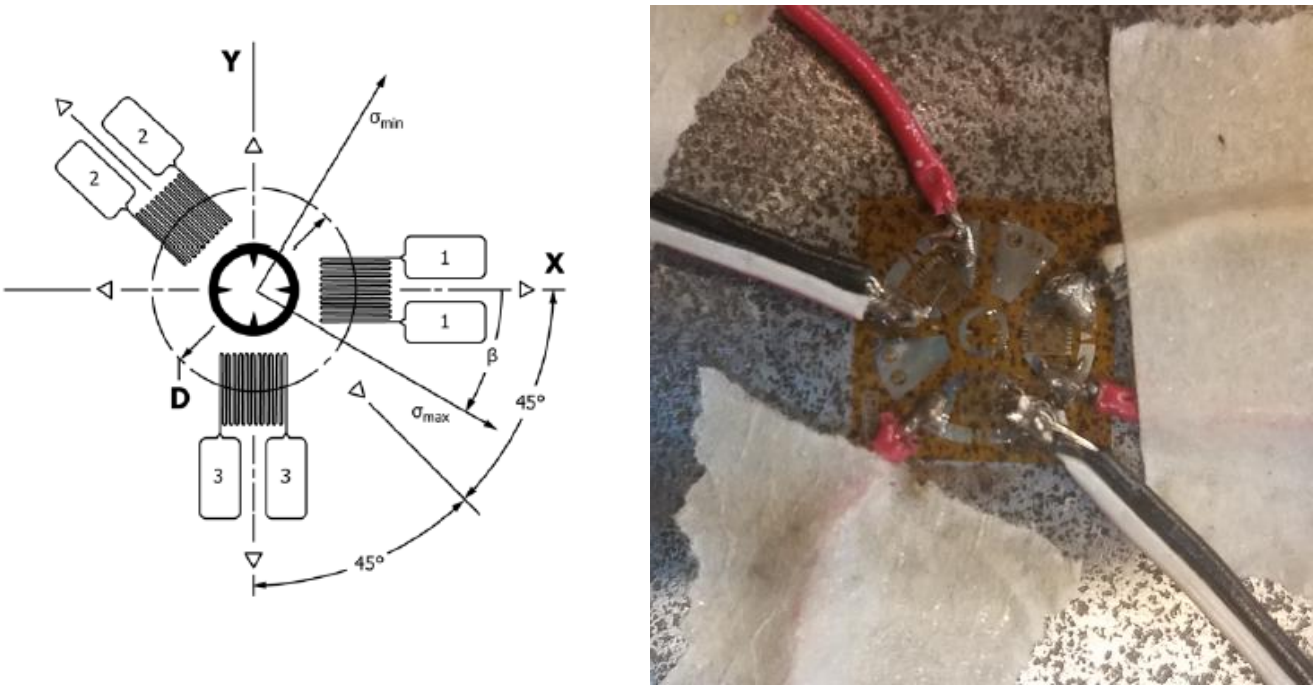

Figure 59 - Residual Stress Strain Rosette - (a) Layout Diagram [30], (b) Example Rosette

Using the strains corresponding to the numbered gauge directions shown above, the following combination strain vectors are calculated with the equations [30];

$$p_j = isotropic\ (equi - biaxial) strain = (\varepsilon_3 + \varepsilon_1)_j/2 \quad (1)$$

$$q_j = 45° \; shear \; strain = (\varepsilon_3 - \varepsilon_1)_j/2 \tag{2}$$

$$t_j = xy \; shear \; strain = (\varepsilon_3 + \varepsilon_1 - 2\varepsilon_2)_j/2 \tag{3}$$

In equations *1-3* it is important to note that the strains that are used at a generic position *k* in the vector are the cumulative strain after drilling to a hole depth corresponding to step *k*. Additionally, the raw strain data must be manipulated to ensure at zero-depth the strains are zero. Once the combination strain vectors are calculated, the standard errors in the combination strains should be estimated using equations *4-6 [30]*;

$${p_{std}}^2 = \sum_{j=1}^{n-3} \frac{\left(p_j - 3p_{j+1} + 3p_{j+2} - p_{j+3}\right)^2}{20(n-3)} \tag{4}$$

$${q_{std}}^2 = \sum_{j=1}^{n-3} \frac{\left(q_j - 3q_{j+1} + 3q_{j+2} - q_{j+3}\right)^2}{20(n-3)} \tag{5}$$

$${t_{std}}^2 = \sum_{j=1}^{n-3} \frac{\left(t - 3t_{j+1} + 3t_{j+2} - t_{j+3}\right)^2}{20(n-3)} \tag{6}$$

Where n = the total number of data points for the strain vector. These standard errors will be used to create a smoothing criterion later.

The next step in the calculations is manipulating the calibration matrices and the combination strain vectors depending on the number and depth of increments used in the drilling. The calibration matrices were derived from finite element work and standardized for the common rosette geometries [30]. These matrices, represented visually in Figure 60 [30], relate the surface strain relieved during the drilling to a unit

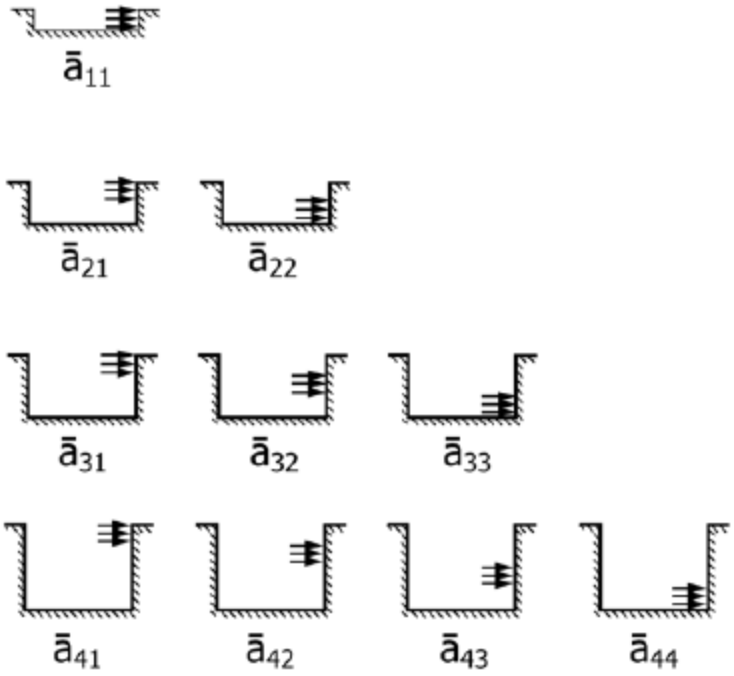

Figure 60 - Representation of Calibration Matrix [30]

stress present through at hole depth increment. In other words, a_{44} is the surface strain relieved due to a unit stress acting on the fourth increment of a hole four increments deep. In the ASTM standard, the calibration matrices are 20x20 lower triangular matrices, with each of the 20 increments corresponding to 0.05mm of depth for the rosettes used in this study for a total of 1mm of analysis. Therefore, if the depth increments, in terms of number of increments and depth per increment, used in the experimental measurement do not match the assumptions of the matrices, either the matrices need to be adjusted or the strain vectors need to be adjusted. In the case of fewer increments than the matrix, the rows of the matrix must be summed appropriately, which would be the equivalent of assuming that there is a unit stress across the depth of the summed increments. For example, assume the matrix used is the 4x4 matrix shown in Figure 60 but the hole drilled was drilled in two equal depth steps which drilled to the same final depth as the four

increments assumed by the matrix. In this case the summation of a_{21} and a_{22} would be the equivalent of a_{11} for the new matrix, the summation of a_{41} and a_{42} would be the equivalent of a_{21} for the new matrix, and the summation of a_{43} and a_{44}would be the equivalent of a_{22} for the new matrix. This manipulation changes the size of the matrix to the appropriate size for the input data set. In the other case, when the depth increments are smaller than the matrix assumes, the strain at the correct depth increments must be interpolated from the original data. After manipulation, the calibration matrices should be a lower triangular matrix with the same characteristic length as the combination strain vector. In addition to manipulating the calibration matrices for size, they must be scaled by a factor equal to the square of the diameter of the drilled hole divided by the square of the assumed diameter for the matrix, in this study the assumed diameter for the matrix is 2mm and the actual drilled hole diameter is variable. Once the calibration matrices and strain vectors are properly manipulated, the stresses at each depth can be calculated through the integral method using equations 7-9 [30];

$$\left(\bar{a}^T\bar{a} + \alpha_p c^T c\right)P = \frac{E}{1+v}\bar{a}^T p \tag{7}$$

$$\left(b^T\bar{b} + \alpha_Q c^T c\right)Q = E\bar{b}^T q \tag{8}$$

$$\left(b^T\bar{b} + \alpha_T c^T c\right)T = E\bar{b}^T t \tag{9}$$

Where; $\bar{a}$ = calibration matrix for isotropic stresses

$\bar{b}$ = calibration matrix for shear stresses

α = regularization factor for respective stress P, Q, or T.

c = tri-diagonal "second derivative" matrix for Tikhonov regularization

P = uniform isotropic stress

Q = uniform 45° shear stress

T = uniform x-y shear stress

These equations can be solved for the stress vectors P, Q, and T respectively. It is important to note that since the integral method is known to be numerically ill-conditioned as the number of increments increase, regularization is generally required. As the equation above shows, regularization is done using a regularization matrix c and a corresponding regularization coefficient α. The matrix c is a tri-diagonal matrix in which the size is the same as the calibration matrix, the first and last row are zeros, and other than the first and last row, all rows have [-1 2 -1] centered on the diagonal [30]. The amount of regularization must be optimized using the α term, which is generally limited to numbers between 10^{-4} and 10^{-6} [30], in an iterative process to minimize the misfit between the unregularized strains and the calculated stresses. The misfit vectors are calculated using the following equations [30];

$$p_{misfit} = p - \frac{1+v}{E}\bar{a}P \tag{10}$$

$$q_{misfit} = q - \frac{1}{E}\bar{b}Q \tag{11}$$

$$t_{misfit} = t - \frac{1}{E}\bar{b}T \tag{12}$$

Using the misfit vectors, the mean squares should be calculated as follows;

$$p_{rms}{}^2 = \frac{1}{n}\sum_{j=1}^{n}(p_{misfit})_j{}^2 \tag{13}$$

$$q_{rms}{}^2 = \frac{1}{n}\sum_{j=1}^{n}(q_{misfit})_j{}^2 \tag{14}$$

$$t_{rms}{}^2 = \frac{1}{n}\sum_{j=1}^{n}(t_{misfit})_j{}^2 \tag{15}$$

Now a comparison must be made between the mean square of the misfits and the standard errors, calculated in equations 1-3, of the combination strain vectors. If the values for the mean square of the misfit is within 5% of the value of the standard error of the combination strains, the calculated stresses from equations 7-9 are acceptable. If the values are more than 5% different, the regularization coefficient must be adjusted as follows;

$$(\alpha_P)_{new} = \frac{p_{std}{}^2}{p_{rms}{}^2}(\alpha_P)_{old} \tag{16}$$

$$(\alpha_Q)_{new} = \frac{q_{std}{}^2}{q_{rms}{}^2}(\alpha_Q)_{old} \tag{17}$$

$$(\alpha_T)_{new} = \frac{t_{std}{}^2}{t_{rms}{}^2}(\alpha_T)_{old} \tag{18}$$

With the new regularization coefficient, the stresses must be recalculated, and this process is repeated until the difference is less than 5%. Once the stresses are accepted, they can be converted back to cartesian coordinates as follows [30];

$$(\sigma_x)_j = P_j - Q_j \tag{19}$$

$$(\sigma_y)_j = P_j + Q_j \tag{20}$$

$$(\tau_{xy})_j = T_j \tag{21}$$

As part of this thesis, a MATLAB code was developed for these calculations and can be seen in Appendix E.

6.4 Results – Residual Stresses

This section will introduce the preliminary results of the residual stress measurements performed on the gusset-less fatigue specimen. A total of six measurements were taken on the gusset-less fatigue specimen, five of those measurements were on specimen one, which was the one tested for fatigue, and one of those measurements was on specimen two, which has not been tested or used for any purpose as of this time. In addition to measurements on the fatigue specimen, measurements were taken on a variety of other metal samples, but the focus of this section will be on the measurements taken on the fatigue specimen. Before introducing the data from the fatigue specimen, data will be presented in order to show a verification of the methods used in this study.

As previously mentioned, residual stresses are complex and often overlooked, especially in civil engineering applications. For this reason, especially when experience is very limited, it is important to verify the methods that are used in order to gain confidence in the results. In this study, there were two primary things that needed to be verified. The first was the drilling method, based on the initial measurements, which appeared to be high, concern was raised about inducing stresses locally during the drilling. This could potentially alter the measurements and result in spurious stresses throughout the thickness. With that in mind, two measurements were taken on a sample of annealed steel, one measurement used a plunging drilling method, which is thought to be more damaging to the material, and the other measurement was performed with the orbital method. Figure 61 shows the relieved strains measured throughout the drilling process using the plunging method, with a 1.66mm hole diameter, to a depth of 2mm

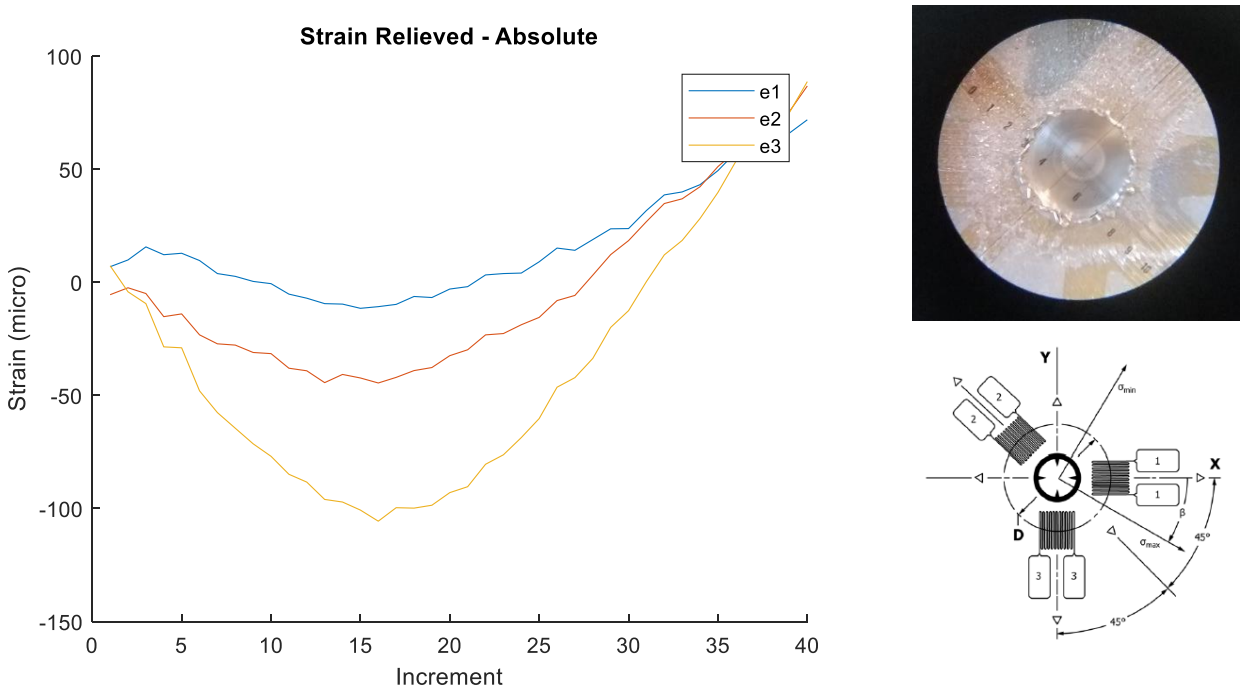

Figure 61 - Annealed Steel - Plunging

with 40 equally spaced increments. Figure 62 shows the relieved strains measured throughout the drilling process using the orbital method, with a 2.05mm hole diameter, to a depth of 2mm with 20 increments in the first 1mm and 10 increments in the last 1mm. It should be noted that the orientation of the legs of the rosette that correspond to strain gauge 1 and 3 are switched between the two different methods. As the graphs shows the behavior is very similar for the first 20 increments and then it starts to deviate, where the

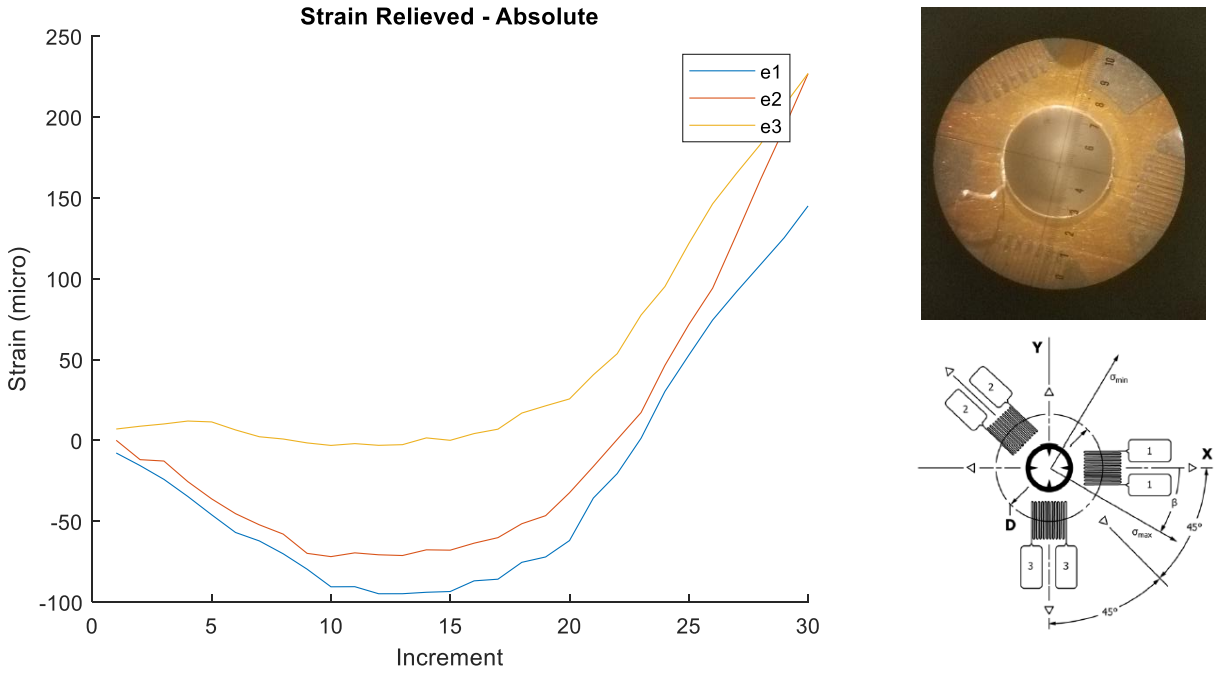

Figure 62 - Annealed Steel - Orbital

orbital method is measuring a higher strain relieved. This deviation could just be the actual variation, due to the general variability of residual stresses, or another likely explanation is the fact that with a larger hole diameter, there is more material removed, leading to a greater strain relieved. Regardless, since the first 1mm was closely matching, and that is the data used for the calculations, the stresses should be similar. Based on this

experiment, it was concluded that the drilling method was not inducing significant strains during the measurement procedure.

The next verification was regarding the calculation method. Since the calculation for non-uniform residual stress profiles can be complex, ensuring the developed MATLAB code was properly calculating the stresses was a challenge. To accomplish this verification, a few data sets, and the corresponding stress profiles were provided by Dr. Gary Schajer, a professor of mechanical engineering at the University of British Columbia. Using these data sets, and the code developed in this research, the stress profiles were calculated and compared to those calculated by Dr. Schajer, using the H-Drill software he developed for residual calculations. Figure 63 shows one of the comparisons made between the two calculated stress profiles. The stress vectors shown with a dashed line are those calculated from the H-Drill software, and the stress vectors shown with the solid lines are those calculated with the code developed in this research. As the figure shows, the stresses are in very good agreement, even with the highly non-uniform nature of the stresses. This verification, along with the verification of the drilling methods, provided confidence in the methodology used to measure and calculate the residual stresses in the gusset-less fatigue specimen.

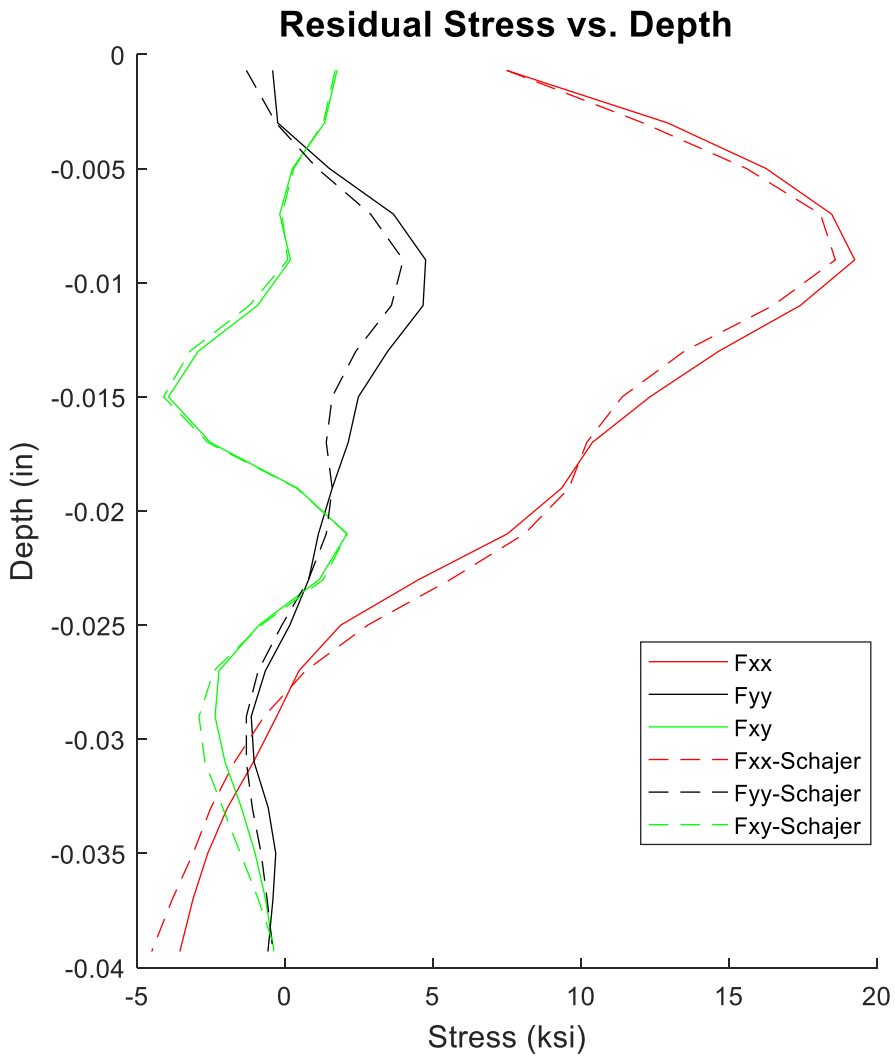

Figure 63 - Calculation Verification

As stated above, residual stress measurements were performed on the gusset-less fatigue specimen a total of six times, varying the location of the measurement along the top-flange, the loading state of the specimen, and the cumulative fatigue cycles. All measurements were performed away from the edge of the top-flange and away from the web. Of the six holes drilled on the gusset-less specimen, three will be presented here.

Figure 64 shows the location of the first measurement on the bottom side of the top flange. The hole drilled was 1.66mm in diameter and used the plunge method with 10 increments

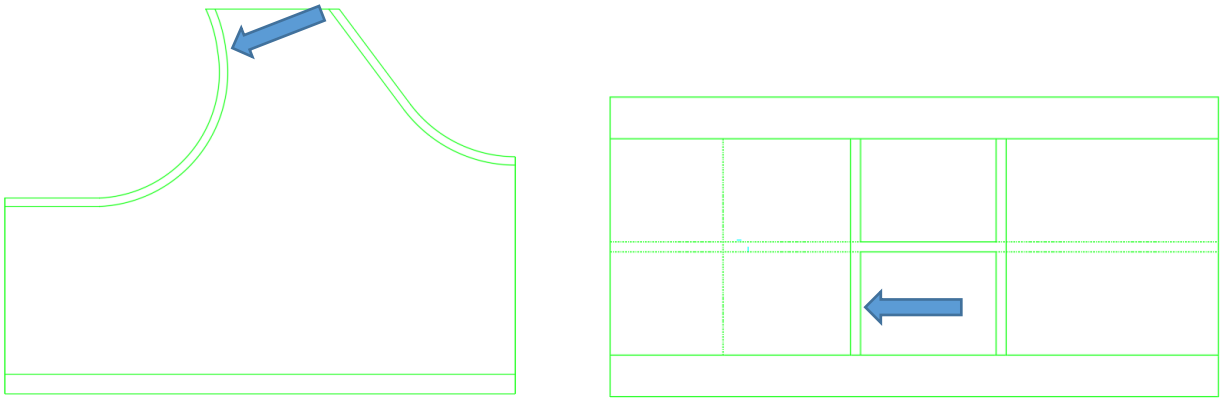

Figure 64 - Residual Hole Location 1 - Elevation (left), Plan View (right)

of 0.20mm for a total depth of 2mm. The specimen was not installed into the test fixture

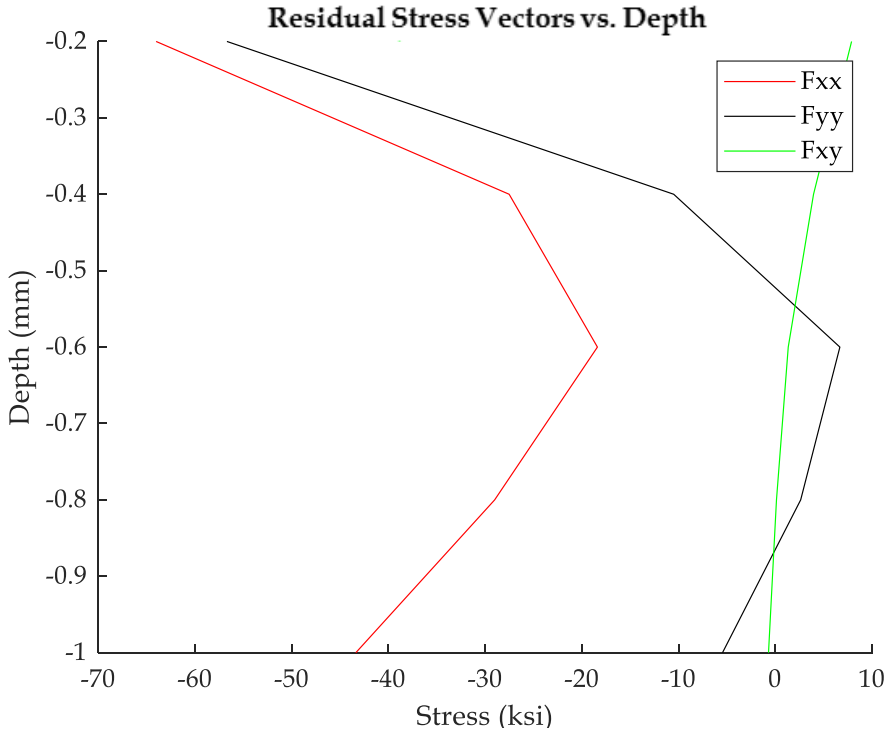

Figure 65 - Residual Stress Profile - Location 1

at the time of measurement and no fatigue testing had been performed on the specimen.

Figure 65 shows the calculated stress profile through the analysis depth. The coordinate system corresponding to the stresses shown is related to the orientation of the strain rosette grids, where the x-axis is aligned with grid 1 and corresponds to the direction of 'Fxx', and the y-axis is aligned with grid 3 and corresponds to the direction of 'Fyy'. In this case the y-axis is tangent to the curve radius of the flange at the measurement location and the x-axis is perpendicular to the curve. As the stress profile shows, there is a high compressive residual stress in the x- and y-directions on the surface which decreases in magnitude with depth before beginning to increase again. The shear stress is approximately zero through the depth. Since the calculated values exceed the 70% of the yield stress, which is the limitation of this method, the results should only be used as a qualitative measure.

The next measurement location is shown in Figure 66. The hole drilled was 1.66mm in diameter and used the plunge method with 20 increments of 0.10mm for a total depth of 2mm. The specimen was installed into the test fixture at the time of measurement, meaning a bolt load was applied but no external load from the actuator.

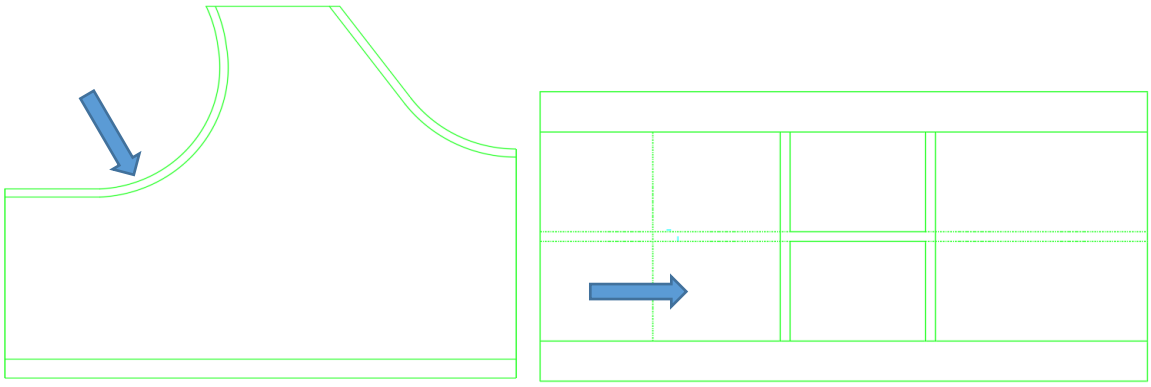

Figure 66 - Residual Hole Location 2 - Elevation (left), Plan View (right)

At this point, approximately 250,000 load cycles had been cumulatively applied to the specimen.

Figure 67 shows the calculated residual stress profile through the analysis depth.

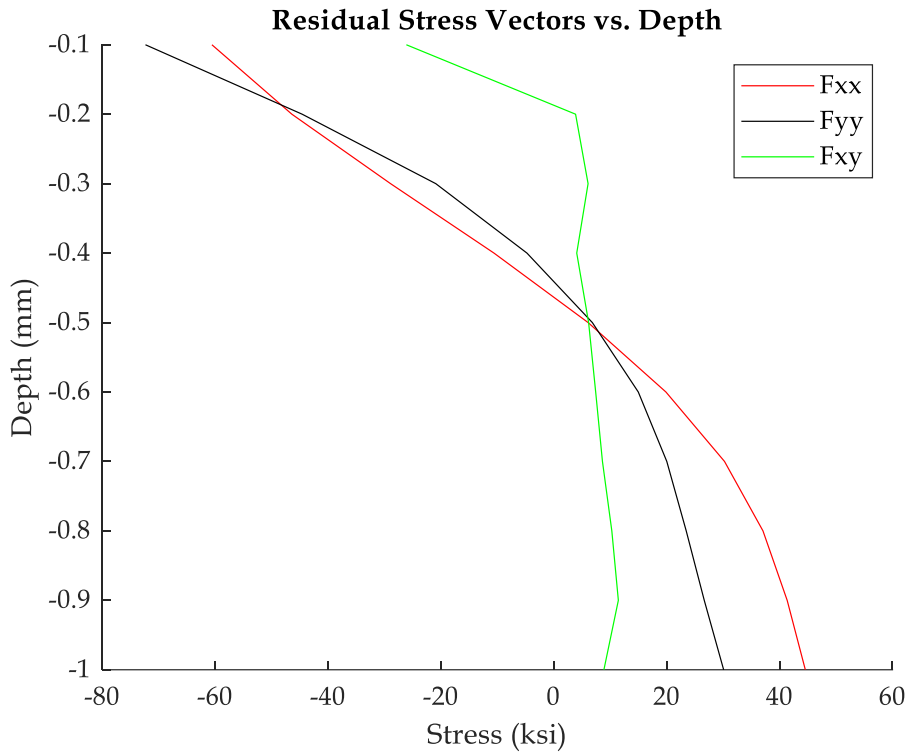

Figure 67 - Residual Stress Profile - Location 2

The orientation of the coordinates for this location are the same as the previous location. The stress profile from this measurement show a similarly high compressive residual stress at the surface in both the x- and y-direction. This compressive stress transitions to a tensile stress as the depth increases. As for the shear stress, at the surface it is compressive in nature before quickly transitioning to tensile and staying relatively consistent through the remainder of the depth. Once again, the stresses calculated have

exceeded the yield limit of the material and therefore should only be used as a qualitative assessment of the residual stress state.

The last hole location is shown in Figure 68. The hole drilled was 2.05mm in diameter using the orbital method with 20 increments of 0.05mm for the first 1mm and 10 increments of 0.10mm for the last 1mm, making a total hole depth of 2mm. At the time of drilling the specimen was installed into the test fixture and approximately 1,600,000 load cycles had been cumulatively applied to the specimen. Figure 69 shows the calculated residual stress profile for the final hole location. The coordinates for this measurement are the same as the previous measurements.

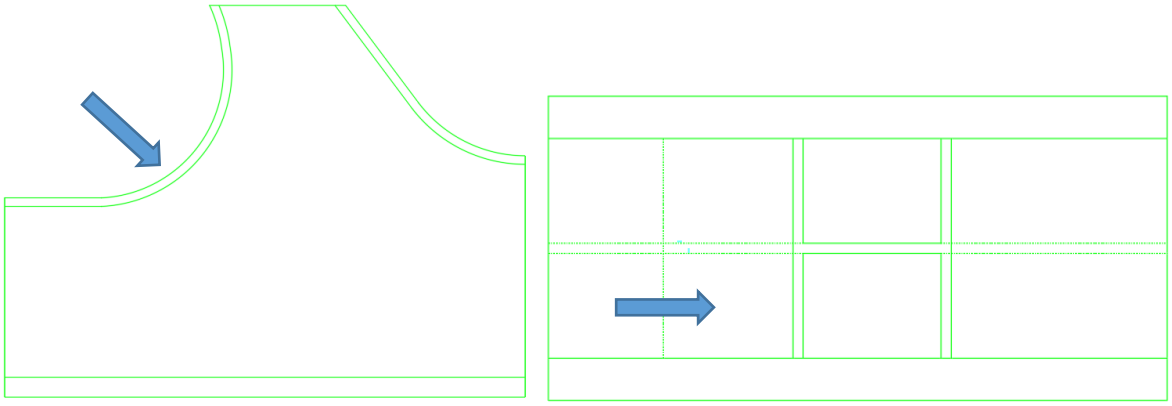

Figure 68 - Residual Hole Location 3 - Elevation (left), Plan View (right)

The x- and y-stresses at the surface are compressive in nature and increase in magnitude through the first few depth increments, before fluctuating around -20 ksi in the x-direction, and zero in the y-direction. The shear stress at the surface is tensile in nature and gradually transitions to compression as the depth increases. This stress profile appears to be highly non-uniform, which could be a result of the increased number of depth increments. Since the calculations are known to be numerically ill-conditioned as the number of depth increments increases, and inversely, the depth per increment decreases, it is a potential source of error in the calculations. Once again, the stresses calculated exceed the 70% yield criterion as one point in the profile, so the results must be used qualitatively.

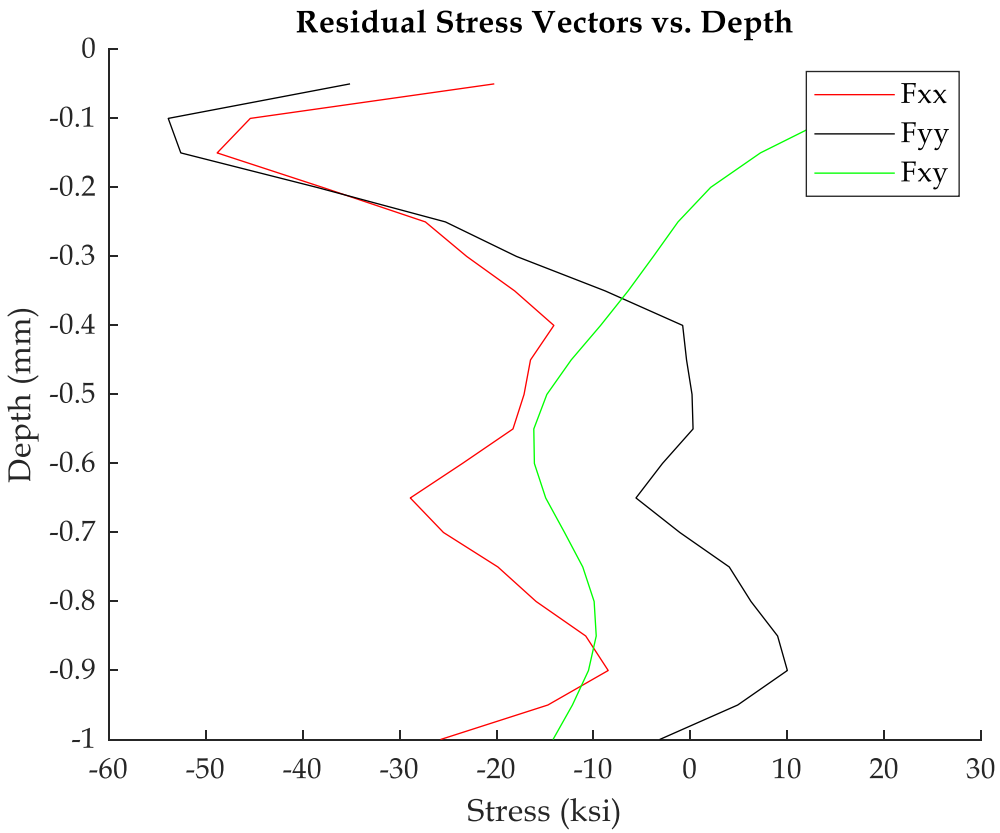

Figure 69 - Residual Stress Profile - Location 3

In addition to the measurements presented in this section, additional measurements will be presented in Appendix F. Based on the results shown here, the measurements obtained using the hole-drilling method are to be used as a qualitative tool to estimate the behavior of the residual stresses with depth. Although they are qualitative, the general profile is close to what is expected in a steel sample which has undergone sand-blasting [39]. With that in mind, the residual stresses at the surface, which is generally the critical fatigue location, are high in magnitude and compressive in nature. In terms of fatigue, this is considered beneficial for fatigue performance, since a fatigue crack that initiates in an area of compressive stress, residual or otherwise, will not propagate.

7 SUMMARY, CONCLUSIONS, AND FUTURE WORK

This chapter will summarize the work from this thesis including the results from the fatigue testing and the residual stress. Next, there will be a section listing the overall conclusions made from the work presented in this thesis. Lastly, future work is discussed regarding this project.

7.1 Summary

The objective of this research was to investigate the fatigue performance of the Gusset-less truss connection used in place on the Memorial bridge. To investigate the performance, a scale-model of the connection was designed and fabricated in a previous research [31]. In addition to the scaled-connection, a test setup for an experimental fatigue test was designed given the limitations of the current UNH Structural Engineering Laboratory [31]. In this work, adjustments were made to the original test setup to correct undesirable behavior. These adjustments were in the form of providing additional rigidity to the reaction block by adding concrete and adding a steel shim support under the tip of the specimen to restrain vertical movement. Modifications were also made to the original instrumentation plan [31] with the addition of 2-Dimensional Digital Image Correlation (DIC).

Given that the infrastructure available for this fatigue test was limited, the test setup was not traditional. With that, there were concerns about ensuring consistency across multiple testing periods in a high-cycle fatigue test. For this reason, an approach to monitoring the response of the fatigue test specimen and the overall setup was

developed in this work. The protocol that was presented is a systematic method that combines visual and physical inspections, along with periodic, full characterizations of the structural response of the test setup through a System Identification (System ID). The System ID method used in this study captures the structural response at key locations along the test setup using DIC measurements along with LVDTs. In addition to the periodic characterization provided by the System ID, the actuator force-displacement relationship was used to quickly indicate if there has been a change in the overall response of the system.

In this work several finite element models (FEM) of the test setup were developed and refined. The final model used in this study is a detailed, blind, model with the objective of capturing the structural response of not only the fatigue specimen, but the test setup as well. This model underwent a mesh sensitivity study and was refined until the response was acceptable.

During this work the Gusset-less fatigue specimen was tested with the presented fatigue loading. The structural response was captured through strain gauges and DIC measurements. The response of these measurements was also compared to the numerical model to check the validity of the model. In terms of loading the specimen in fatigue, a life prediction was estimated using the design assumptions and the specimen was loaded to the expected number of cycles to failure, which was 1,600,000 cycles. No damage was detected in the test specimen.

Lastly, an investigation of the residual stress state of the fatigue specimen was carried out. In this study, the hole-drilling method was applied to measure the near surface residual stresses in the top-flange of the fatigue specimen. The drilling methods used were verified against one another to ensure that the effect of the drilling on the residual stresses was not significant. Additionally, a MATLAB code was developed for the calculations, using the integral method, of the residual stresses. These calculations were compared to the output of the software H-Drill [40] and found to produce the same results.

7.2 Conclusions

Based on the work presented in this thesis, the following conclusions are presented;

- The monitoring protocol developed in this study provides a way to ensure consistent behavior across a high-cycle fatigue test in which the test is performed in multiple testing intervals. [Section 3.1]
- The System ID was used to characterize the response at key locations along the test setup. The responses across different testing periods were compared, and the average change in response was approximately 5%. [Section 3.2]
- The actuator force-displacement relationship was used as an indicative measurement between System IDs in this study. It was found that the relationship could reliably indicate a change in the test setup based on the change in the response. [Section 3.3]

- Based on the results from the System IDs, supplemented by the force-displacement relationship, it is shown that the overall response of the test setup was consistent across the high-cycle fatigue test. [Section 3.4]
- Comparisons between all forms of measurement were performed. The displacements measured with DIC matched closely with the LVDT response in the System ID. [Section 3.2]
- The principal strains measured with DIC matched closely with the measurements from the strain gauges, but the comparison was limited to two gauges. [Section 5.4]
- The principal strains measured with DIC and the strain gauges were compared to the numerical model. It was found that the average difference between the DIC and the model was approximately 3.7%. The average difference between the strain gauges and the model was approximately 6.4%. This suggests that the model is matching the measured response relatively well, but further refinement is needed. [Section 5.4]
- Under the most conservative assumptions, using a hot-spot stress of 14 Ksi at the toe of the weld, the AASHTO S-N curve, and a category C fatigue detail, the connection has been tested and the results show that the design expectations are exceeded. As a reference, the highest stress measured at the Gusset-less connection on the Memorial bridge is 6 Ksi, therefore the assumption of infinite life is confirmed. [Section 5.5]

- Given the assumptions regarding the fatigue life, further research is needed to appropriately categorize the Gusset-less connection in terms of fatigue details to be able to apply the S-N curves and estimate life. [Section 5.5]
- The residual stresses were investigated in the top-flange of the fatigue specimen. The stresses indicate a compressive stress at the surface of the specimen, which is consistent with the residual stress profile of a sand blasted metal. The magnitude of the stresses was higher than the theoretical limits of the calculation method and therefore must be used qualitatively, not quantitatively. [Section 6.4]

7.3 Future Work

After finishing the work in this thesis, the following recommendations are presented for future work relating to this study;

- Additional research is needed to categorize, or develop a fatigue category, based on a curved weld loaded for fatigue.
- The energy, based on the strain gauges in the critical fatigue area, should be quantified and monitored to indicate damage in the area.
- The numerical model used in this study should be calibrated to match the measured response from the experiment more closely.
- Once the model is calibrated, multiple damage scenarios to the weld should be modeled to see the response of a damaged weld.
- Damage should be induced, based on the results of the modeling, to the fatigue specimen to create a more severe fatigue detail.

- Once damage is induced, the specimen should be tested to failure and the crack propagation should be studied.
- Residual stresses should be investigated in other locations, besides the top-flange, on the test specimen.
- An investigation into the residual stresses caused by metalizing on the Memorial bridge should be explored.
- Destructive testing should be performed at multiple locations along the test specimen to better understand the stresses through the thickness.

REFERENCES

1. Contractors, H.C.A.W., *Portsmouth Memorial Bridge Replacement: An Exploration of Truss Design without Gusset Plates*. 2013: New York.
2. Instruments, N. *Measuring Strain with Strain Gages*. White Papers 2016; Available from: http://www.ni.com/white-paper/3642/en/#top.
3. Group, V.P., *Fatigue Characteristics of Micro-Measurements Strain Gages*, in *Tech Note*. 2010.
4. D. A. Skolnik, W.J.K., J. W. Wallace, *Instrumentation For Structural Health Monitoring: Measuring Interstory Drift*, in *World Conference on Earthquake Engineering*. 2008: Beijing, China.
5. Instruments, N. *Measuring Position and Displacement with LVDTs*. White Papers 2018; Available from: http://www.ni.com/white-paper/3638/en/.
6. Bing, P., et al., *Two-dimensional digital image correlation for in-plane displacement and strain measurement: a review.* Measurement Science and Technology, 2009. **20**(6): p. 062001.
7. Aktan, A.E., et al., *Structural identification for condition assessment: experimental arts.* 1997. **123**(12): p. 1674-1684.
8. F. Catbas, T.K.-C., A Emin Aktan, *Structural Identification of Constructed Systems*, in *Structural Identification of Constructed Systems*, T.K.-C. F. Catbas, A Emin Aktan, Editor.
9. Pan, Q., *System identification of constructed civil engineering structures and uncertainty*. Vol. 68. 2007: Citeseer.
10. Dutt, A., *Effect of Mesh Size on Finite Element Analysis of Beam*. Vol. 2. 2015.
11. *Abaqus/CAE User's Guide*, ed. D. Systèmes. 2011, Providence, RI, USA.
12. Choi, C.K. and H.G. Kwak, *The effect of finite element mesh size in nonlinear analysis of reinforced concrete structures.* Computers & Structures, 1990. **36**(5): p. 807-815.
13. Liu, Y., *Effects of Mesh Density on Finite Element Analysis*. Vol. 2. 2013.
14. *Fatigue (Material)*. 2018 [cited 2018; Available from: https://en.wikipedia.org/wiki/Fatigue_(material).
15. Campbell, F.C., *Elements of MEtallurgy and Engineering Alloys*. 2008: ASM International.
16. Transportation, O.D.O., *Structure Project Manager Seminar - Fatigue Analysis*. 2005.
17. Dong, P., *A structural stress definition and numerical implementation for fatigue analysis of welded joints.* International Journal of Fatigue, 2001. **23**(10): p. 865-876.
18. Fisher, J. and B. T. Yen, *FATIGUE STRENGTH OF STEEL MEMBERS WITH WELDED DETAILS*. Vol. 14. 1977. 118-129.
19. Fisher, J.W., *EVALUATION OF TYPICAL WELDED BRIDGE DETAILS FOR FATIGUE DESIGN* 1973.
20. *AASHTO LRFD bridge design specifications*. 2008: Fourth edition with 2008 interim revisions. Washington, D.C. : American Association of State Highway and Transportation Officials, [2008] ©2007.

21. Socie, D.F., *Fatigue of Welds*. 2014: efatigue.com.
22. Kamaya, M. and M. Kawakubo, *Mean stress effect on fatigue strength of stainless steel.* International Journal of Fatigue, 2015. **74**: p. 20-29.
23. Kumbhar, S. and R. Tayade, *A Case Study on Effect of Mean Stress on Fatigue life*. 2014.
24. Susmel, L., R. Tovo, and P. Lazzarin, *The mean stress effect on the high-cycle fatigue strength from a multiaxial fatigue point of view.* International Journal of Fatigue, 2005. **27**(8): p. 928-943.
25. Wehner, T. and A. Fatemi, *Effects of mean stress on fatigue behaviour of a hardened carbon steel.* International Journal of Fatigue, 1991. **13**(3): p. 241-248.
26. Fatemi, A., *Fatigue Tests and Stress-Life (S-N) Approach*. 2014: efatigue.com.
27. University, I.S., *Fatigue Life Evaluation*.
28. Fatemi, A., *Residual Stresses and Their Effects On Fatigue Resistance*. 2014: efatigue.com.
29. S. Schajer, G. and C. O. Ruud, *Practical Residual Stress Measurement Methods*. 2013. 1-27.
30. International, A., *ASTM E837-13a, Standard Test Method for Determining Residual Stresses by the Hole-Drilling Strain-Gage Method*. 2013, ASTM: West Conshohocken, PA.
31. Fischer, F., *DESIGN AND FABRICATION OF A SPECIMEN AND EXPERIMENTAL SETUP FOR FATIGUE TESTING OF A GUSSET-LESS BRIDGE CONNECTION*, in *Civil and Environmental Engineering*. 2018, University of New Hampshire.
32. Corporation, M.S., *Series 244 Hydraulic Actuators*.
33. Corporation, M.S., *MTS Series 793 Tuning and Calibration*.
34. Corp., D.S., *ABAQUS.* 2013.
35. Solutions, C., *VIC-2D 2009.* 2009.
36. Group, V.P., *Special Use Sensors - Residual Stress Strain Gauges.* 2018.
37. Group, V.P., *Measurement of Residual Stresses*

by the Hole-Drilling Strain Gage Method*. 2010.
38. Gary S. Schajer, P.S.W., *Practical Residual Stress Measurement Methods*, in *Practical Residual Stress Measurement Methods*, G.S. Schajer, Editor. 2013, John Wiley & Sons.
39. Lestari, S., *Residual Stress Measurements of Unblasted and Sandblasted Mild Steel Specimens Using X-Ray Diffraction, StrainGage*

Hole Drilling, and Electronic Speckle Pattern Interferometry (ESPI) Hole Drilling Methods, in *Civil Engineering*. 2004, University of New Orleans.
40. Schajer, G.S., *H-Drill Hole-Drilling Residual Stress Calculation Program*.
41. MicroMeasurements, *General Purpose Strain Gages - Linear Pattern*. 2018.
42. Correlated Solutions, I., *Minimizing Noise and Bias in 3-D DIC.*
43. Simonsen, M., *Strain Tensors and Criteria in Vic*. 2018, Correlated Solutions, Inc.: Correlated Solutions Knowledge Base.

APPENDICIES

APPENDIX A – INSTRUMENTATION

This appendix will provide additional information regarding the instrumentation. This will include the data sheets [41] for the strain gauges used and a mathematical background on the digital image correlation.

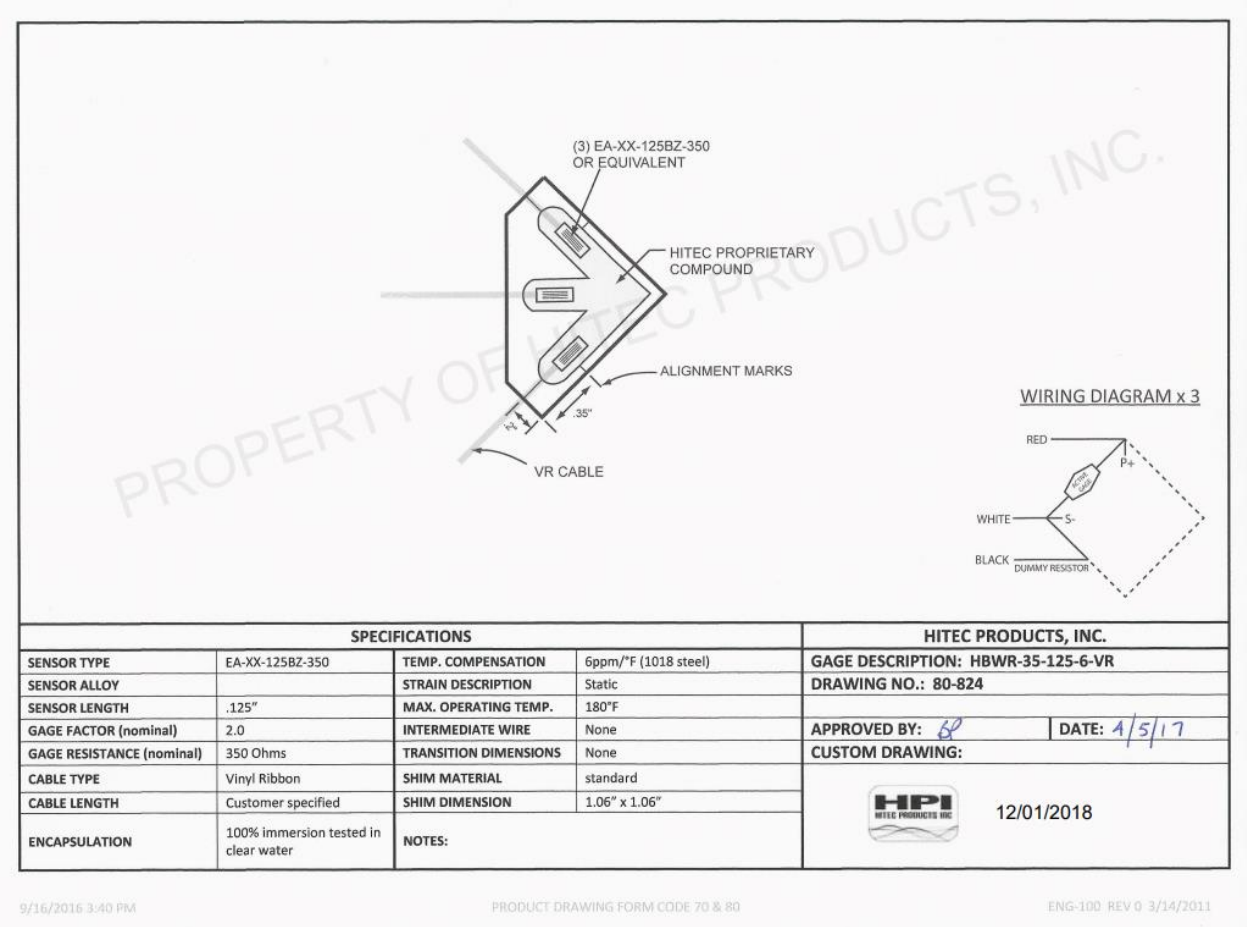

SPECIFICATIONS				HITEC PRODUCTS, INC.
SENSOR TYPE	EA-XX-125BZ-350	TEMP. COMPENSATION	6ppm/°F (1018 steel)	GAGE DESCRIPTION: HBWR-35-125-6-VR
SENSOR ALLOY		STRAIN DESCRIPTION	Static	DRAWING NO.: 80-824
SENSOR LENGTH	.125"	MAX. OPERATING TEMP.	180°F	
GAGE FACTOR (nominal)	2.0	INTERMEDIATE WIRE	None	APPROVED BY: BP DATE: 4/5/17
GAGE RESISTANCE (nominal)	350 Ohms	TRANSITION DIMENSIONS	None	CUSTOM DRAWING:
CABLE TYPE	Vinyl Ribbon	SHIM MATERIAL	standard	
CABLE LENGTH	Customer specified	SHIM DIMENSION	1.06" x 1.06"	HPI HITEC PRODUCTS INC 12/01/2018
ENCAPSULATION	100% immersion tested in clear water	NOTES:		

9/16/2016 3:40 PM PRODUCT DRAWING FORM CODE 70 & 80 ENG-100 REV 0 3/14/2011

Figure 70 - Strain Rosette Data Sheet

MICRO MEASUREMENTS
A VPG Brand

125UW

General Purpose Strain Gages—Linear Pattern

GAGE PATTERN DATA

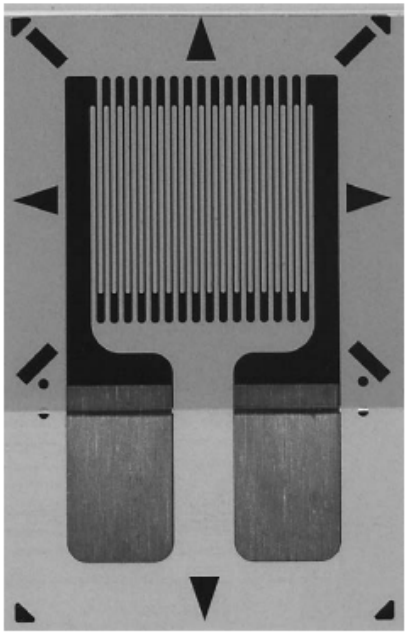

actual size

GAGE DESIGNATION See Notes 1, 2	RESISTANCE (OHMS) See Note 3	OPTIONS AVAILABLE
CEA-XX-125UW-120	120 ±0.3%	P2, SP35
CEA-XX-125UW-350	350 ±0.3%	P2, SP35
W2A-XX-125UW-120	120 ±0.6%	
W2A-XX-125UW-350	350 ±0.6%	

DESCRIPTION

General-purpose gage. Exposed solder tab area 0.10 x 0.07 (2.5 x 1.8 mm). See also 125UN pattern.

Pb-free Available

RoHS* COMPLIANT

GAGE DIMENSIONS

Legend
ES = Each Section
S = Section (S1 = Section 1)
CP = Complete Pattern
M = Matrix

inch
millimeter

Gage Length	Overall Length	Grid Width	Overall Width	Matrix Length	Matrix Width
0.125	0.325	0.180	0.180	0.42	0.27
3.18	8.26	4.57	4.57	10.7	6.9

GAGE SERIES DATA — See Gage Series datasheet for complete specifications

Series	Description	Strain Range	Temperature Range
CEA	Universal general-purpose strain gages.	±5%	–100° to +350°F (–75° to +175°C)
W2A IPX8S Rated	For water-exposure applications. Based on the CEA Series with Option P2 pre-attached cables, W2A strain gages are fully enclosed with a silicone rubber coating and tested to 10 GΩ insulation resistance, 1 meter water depth, 30 minutes duration. Other requirements can be addressed on demand.	±3%	–60° to +180°F (–50° to +80°C)

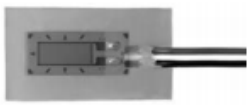

Example of the W2A construction:

IPX8S Rated

Note 1: Insert desired S-T-C number in spaces marked XX.
Note 2: W2A leadwires are attached with lead-free solder and are RoHS compliant.

* CEA gages with Option P2 are not RoHS compliant.

Technical Data References: SEARCH our website using the document number.
11506 – Gage Series; **11507** – Optional Features

Figure 71 - Uniaxial Strain Gauge Data Sheet [40]

The following section will provide a mathematical background on the DIC correlation. In VIC-2D the first step in measurement is dividing the image into a grid of subsets. The subsets serve to divide the image and create unique blocks of pixels used for tracking. Within the subset, a gray value for each of the pixels is assigned as a value from 0 (black) to 100 (white) based on the speckle pattern captured. Once the gray values are assigned for the subsets on the reference image, the correlation can begin on the successive images.

The correlation attempts to track the movement of the subsets in the deformed images compared to the reference image. This is done through a correlation function which used a statistical relationship, one example of which is the sum of squared differences. What the correlation function does is compare the gray values of each pixel within the subset of the reference image against the image that has been displaced by a value of u and y, which correspond to the horizontal and vertical displacements. This comparison is repeated at multiple u and y values until the difference in the gray values are minimized according to the sum of squared differences, or whatever correlation criterion are selected. Figure 72 is the generalized equation for the tracking performed in the DIC program VIC-2D [42].

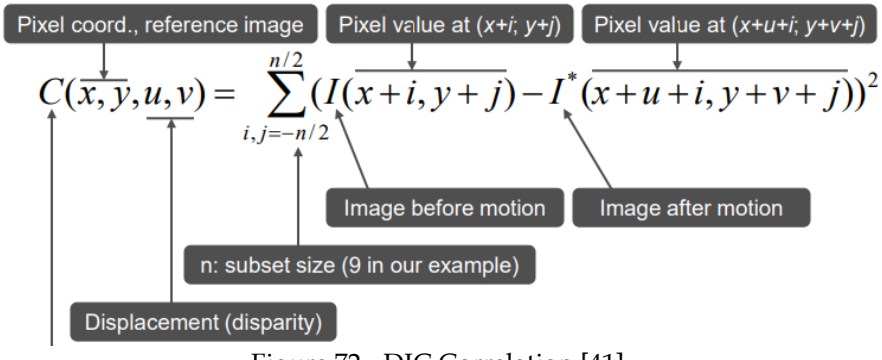

Figure 72 - DIC Correlation [41]

Once the displacement is calculated, the strain can be derived assuming various tensors. The choices in VIC-2D are Lagrange, Hencky, Euler-Almansi, and Log Euler-Almansi. The default, and the tensor used in this study was the Lagrange strain tensor. Figure 73 [43] shows the equations used to calculate the strain using the Lagrange strain tensor.

$$e_{xx} = \frac{\partial u}{\partial x} + \frac{(\frac{\partial u}{\partial x})^2 + (\frac{\partial v}{\partial x})^2}{2}$$

$$e_{yy} = \frac{\partial v}{\partial y} + \frac{(\frac{\partial u}{\partial y})^2 + (\frac{\partial v}{\partial y})^2}{2}$$

$$e_{xy} = \frac{\frac{\partial u}{\partial y} + \frac{\partial v}{\partial x} + \frac{\partial u}{\partial x}\frac{\partial u}{\partial y} + \frac{\partial v}{\partial x}\frac{\partial v}{\partial y}}{2}$$

Figure 73 - Lagrange Strain Equations [42]

With the directional strain calculated, the principal strains are derived using the Mohr's circle relationship.

APPENDIX B – TEST TRACKING

This Appendix will present a data table of all the tests run during the work of this thesis. Additionally, a data sheet used to monitor the fatigue test will be shown and some examples of filled out data sheets will be presented.

Table 10 - Test Tracking History

Date	Session	Time Started	Time Ended	Test Cycles	Cumulative Cycles	System ID performed?	Test Description	Notes
6/20/2018	Night	-	-	5000	5000	No	Short initial test to gather data for DOT meeting	
6/21/2018	Afternoon	-	-	5000	10000	No	Demonstration test for DOT meeting	
7/3/2018	Night	-	-	25200	35200	No	2-hour test	No significant change noted from start to finish
7/7/2018	Afternoon	-	-	6700	41900	No	Planned 4-hour test, stopped early	Specimen tip support became free after 30 minutes, no instability was noted. The test was stopped to reevaluate the setup. The temperature intelock activated after the pressure was released in the pump. The DIC software also closed after starting the test.
7/10/2018	Morning	-	-	14444	56344	Yes	Planned 4-hour test, stopped early	Support under specimen tip moved significantly in the opposite direction as last noted. The test was stopped when one of the supports was close to coming out.
7/10/2018	Afternoon	-	-	10368	66712	No	Planned 4-hour test, stopped early	The pump interlocked due to the temperature limit. The test lasted for 49 minutes and the final temperature was 137F.
7/11/2018	Afternoon	-	-	25782	92494	No	Planned 2-Hour test	Test ran for full 2-hours, the temperature was close to the limit at the end of the test. Shims under South side of specimen tip were moving vertically, steel shims will be added for the next test.
7/12/2018	Morning	-	-	13582	106076	No	Planned 2-Hour test, stopped early	Temperature interlock was activated after 1 hour. The shims on the South side were very stable with minimal vertical movement. The shims on the North side will be replaced with steel shims.
7/13/2018	Morning	10:02	-	21191	127267	No	Planned 2-Hour test, stopped early	Temperature interlock after 1 hour 41 minutes. The temp. started at 88F and ended at 134F
7/16/2018	Morning	10:24	12:28	25782	153049	No	Planned 2-Hour test	Test ran for full 2-hours. Temp started at 97F and ended at 130F. The temperature seemed to stagnate at 130F since around 1 hour into the test all the way until the end. It was noted that the water temp. was lower than normal (60F compared to 70F as "normal").

7/17/2018	Morning	10:11	12:15	25782	178831	Yes	Planned 2-hour test	Test ran full 2 hours. South side shim became loose and was adjusted after 16minutes of testing. There was visible twisting at the tip and the shim will need to be adjusted for the next test. Temperature was stable at 130F with a water temp of 60F
7/18/2018	Morning	10:14	14:20	51610	230441	No	4-hour test	Test ran full 4-hours. Temperature was stabil around 130F for the majority of the test. The water temp. started at 65F and stabilized at 60F for the majority of the test.
7/19/2018	Morning	07:05	08:26	17054	247495	No	Planned 8-hr test	Test ran 1hr and 20 minutes. Water temp started at 65F and fluctuated between 65F and 69F. The oil temp. was 135F when the pump interlocked.
7/20/2018	Morning	-	-	12880	260375	No	Planned 8-hr test	Test ran for just over 1 hour. The water temp started at 65 and fluctuated between 69F and 75F during the test. The oil temp. was 135F when the pump interlocked.
8/3/2018	Morning	-	-	2182	262557	No	Planned 8-hr test	Temp interlock after 10 minutes
8/8/2018	Morning	-	-	1462	264019	No	Planned 8-hr test	Stopped test for tuning purposes.
8/10/2018	Afternoon	-	-	15000	279019	No	Tuning of Actuator	Tuned actuator to fix odd behavior due to lowering pressure. Pressure increased to 3000 PSI at the pump.
8/15/2018	Morning	10:52	12:56	25782	304801	No	2-Hour test	2-Hr test using the building cold water (75F) with a 1/2 hp pump on the inlet side. Oil temp. was stable at 111F for the duration of the test.
8/15/2018	Afternoon	13:04	17:08	51612	356413	No	4-hour test	4-Hr test using the building cold water (75F) with a 1/2 hp pump on the inlet side. Oil temp. was stable at 111F for the duration of the test.
8/16/2018	Morning	07:36	16:09	103225	459638	No	8-hour test	8-Hr test using the building cold water (75F) with a 1/2 hp pump on the inlet side. Oil temp. was stable at 111F for the duration of the test.
8/17/2018	Morning	-	-	154920	614558	No	12-Hour Test	12-hour test using building cold water. The first 6-hour interval ran smoothly but on the ramp to zero force the pump interlocked due to a lower limit. This means the specimen went into compression briefly. The test was restarted for the next 6 hour interval. The interlocked occured again at the same point in the test. Some ringing in the bottom of the hysteresis and force-command was observed.

8/20/2018	Afternoon	-	-	51612	666170	Yes	4-hour test	4-hour test. Temp. was stable. Shims were changed before this test. One shim under the south side tip became loose after approximately 40 minutes into the test. Ringing was still present, tuning will be performed.
8/21/2018	Morning	-	-	77460	743630	No	6-Hour test	6-hour test. Shims were replaced on the south side of the specimen tip before test, this reduced the ringing and the vertical movement. No tuning was performed.
8/23/2018	Morning	-	-	6708	750338	No	4-hour test stopped early	4hr test stopped early due to shim movement
8/23/2018	Morning	-	-	51630	801968	No	4-hour test	4hr test, odd behavior on SRW1H approximately half-way through the test. The gage began fluctuating and the strain gradually increased with significant fluctuations. The gage may have had a loose wire where a previous repair was made from damaged wires.
8/28/2018	Morning	09:00	11:05	26482	828450	No	2-hour test	2-Hour test, shims were changed after the test to reduce the twisting of the specimen. An additional 700 cycles were performed while adjusting shims.
8/28/2018	Afternoon	-	-	25782	854232	No	2-hour test	2-hour test, new shims worked well. No problems during testing period.
8/29/2018	Morning	08:45	10:49	25782	880014	No	2-hour test	2-hour test, no problems during testing period.
8/29/2018	Afternoon	-	-	51630	931644	No	4-hour test	4-hour test, DIC restarted once. Some grinding of the concrete was observed under south side specimen tip shims.
9/2/2018	Morning	-	-	25782	957426	No	2-hour test	2-hour test, anchor bolts were tightened before test. Using new chilled water pump, oil temp seemed stable around 113F. SRW1-D had an offset from it's "normal" strain range, this was fixed after the test by moving the wire.
9/2/2018	Afternoon	-	-	25782	983208	No	2-hour test	2-hour test, chilled water pump used. The oil temp. rose to 123F from 113F over the course of the 2 hours, some adjustments to the pump speed should be made.
9/3/2018	Afternoon	-	-	25782	1008990	No	2-hour test	2-hour test, chilled water pump adjusted to stabilize oil temp at 113F.
9/4/2018	Morning	-	-	25782	1034772	No	2-hour test	2-hour test, normal operation
9/4/2018	Afternoon	-	-	25782	1060554	No	2-hour test	2-hour test, after test bolts were tightened. Actuator bolt was over torqued.

9/24/2018	Morning	-	-	30089	1090643	No	2.5-hour test	Actuator bolt was replaced, 2.5hr test was run. DIC computer shut down after approximately 2-hours due to problem with plug.
9/25/2018	Morning	-	-	25782	1116425	No	2-hour test	First 2-hour test of the day. No problems noted
9/25/2018	Afternoon	-	-	25782	1142207	No	2-hour test	Second 2-hour test of the day. No problems noted.
9/26/2018	Morning	-	-	30089	1172296	No	2.5-hour test	2.5-hour test run. No problems noted.
9/27/2018	Morning	-	-	25782	1198078	No	2-hour test	2-hour test. No problems noted.
10/1/2018	Morning	-	-	30090	1228168	No	2.5-hour test	2.5-hour test run. No problems noted.
10/1/2018	Afternoon	-	-	25872	1254040	Yes	2-hour test	2-hour test. Wires were moved and one of the strain gauges was offset in terms of magnitude. This will be adjusted before next test.
10/10/2018	Morning	-	-	30090	1284130	No	2.5-hour test	2.5-hour test run. SRW1-D wire was moved and caused an offset in measured strain. Adjusted back to normal after test was completed.
10/11/2018	Morning	-	-	30090	1314220	No	2.5-hour test	2.5-hour test. No problems noted.
10/11/2018	Morning	-	-	30090	1344310	No	2.5-hour test	2.5-hour test. No problems noted.
10/12/2018	Morning	-	-	25872	1370182	No	2-hour test	2-hour test. LVDT bumped at 1hour 20m. Into test, offset is present after this point.
10/15/2018	Morning	-	-	30090	1400272	No	2.5-hour test	2.5-hour test. No problems noted.
10/16/2018	Morning	-	-	30090	1430362	No	2.5-hour test	2.5-hour test. No problems noted. Horz. Bolts tightened after test.
10/17/2018	Morning	-	-	30090	1460452	No	2.5-hour test	2.5-hour test no problems noted.
10/18/2018	Morning	-	-	30090	1490542	No	2.5-hour test	2.5-hour test no problems noted.
10/18/2018	Morning	-	-	25782	1516324	Yes	2-hour test	2-hour test, the specimen tip was rocking out of plane more than normal, shim support was replaced and system ID was performed after this test.
10/24/2018	Morning	-	-	30090	1546414	No	2.5-hour test	2.5-hour test with new shim support. No problems noted.
10/26/2018	Morning	-	-	30091	1576505	No	2.5-hour test	2.5-hour test no problems noted.
10/30/2018	Morning	-	-	25782	1602287	No	2-hour test	2-hour test, no problems during testing period. Final test before damage is introduced.

Testing Checklist

Session #		Name of Inspector(s):		Uploaded
Morning☐ Afternoon ☐ Night☐		Date:		☐
Start Time				
Stop Time				
Setup pictures are Taken Before the Test ☐		Expected # of Cycles:		
Setup Pictures are Taken After the Test ☐		Executed # of Cycles:		

Strain Gauges	Y	N	Description
Strain Gauges File Name and Path			
Inspect Attachment			
Sampling Rate Frequency: 60 Hz			
Record strains for ~10 seconds while actuator is off to ensure gages are functioning			

DIC	Y	N	Description
DIC File File Name and Path			
Lights are on and Check Saturation			Note: DIC display should NOT show red on the screen
Lens Caps are off			
Check Cameras Locations			
Sync Mode: Auto			
VIC-3D Integration: Speckle mode			
Capture Mode: Flex Capture			30000ms=1 image 80ms=30s, 1170000ms=1 image

Specimen (Take Pictures and Inspect)	Y	N	Description
Shims			
Support at Tip			
Bolts and Anchors for Loosening or Damage			
Inspect Specimen			
Inspect Bracket			
Inspect Reaction Block			

Actuator	Y	N	Description
MTS Specimen Number			
Inspect Hydraulic Lines			
Inspect for Oil Leak, and Note Temperature			
MTS Controller Software: '100Kip.cfg : Force Tuning Only-3hz'			
Check Tuning Parameters to ensure they have not been changed P-Gain:1.70 I-Gain:0.190			
Define force limits (480kN and -5kN respectively)			
Define force feedback error limits			
Open test procedure			
Check Cyclic load protocol			
Set-point: 55kip			
Cyclic Amplitude: +/- 50kip			

Figure 74 - Test Tracking Data Sheet - Front

LVDT		Y	N	Description
LVDT File Name and Path				
Test if Working				
Channel #	Channel Name			Channel Location
1				
2				
3				
4				

Notes

Figure 75 - Test Tracking Data Sheet - Back

APPENDIX C – SYSTEM ID

In this appendix, additional figures from the System ID will show the individual comparisons at each point of the System ID as well as the horizontal displacements at each location of the system relative to each other.

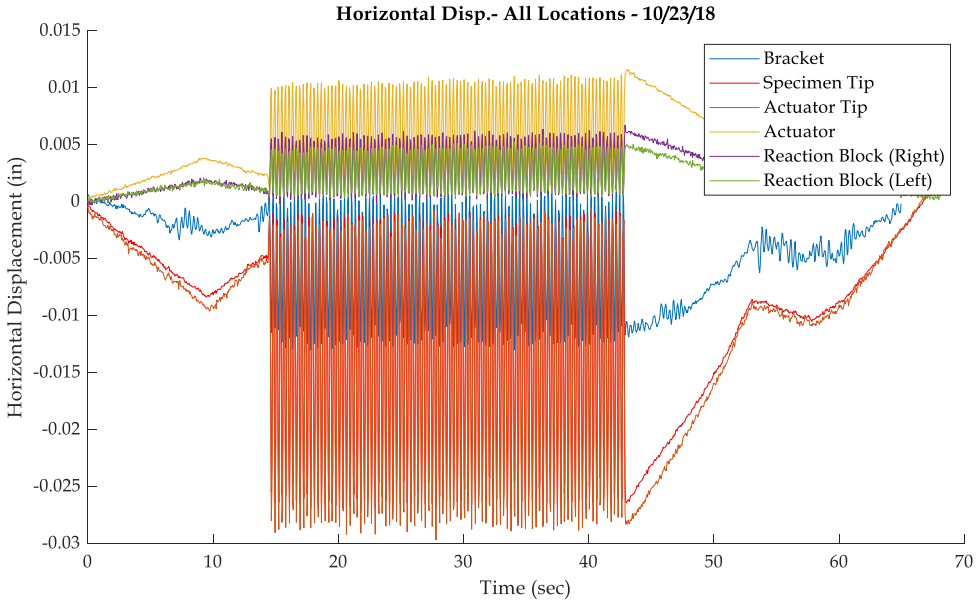

Figure 76 - Horizontal Displacements - All Locations

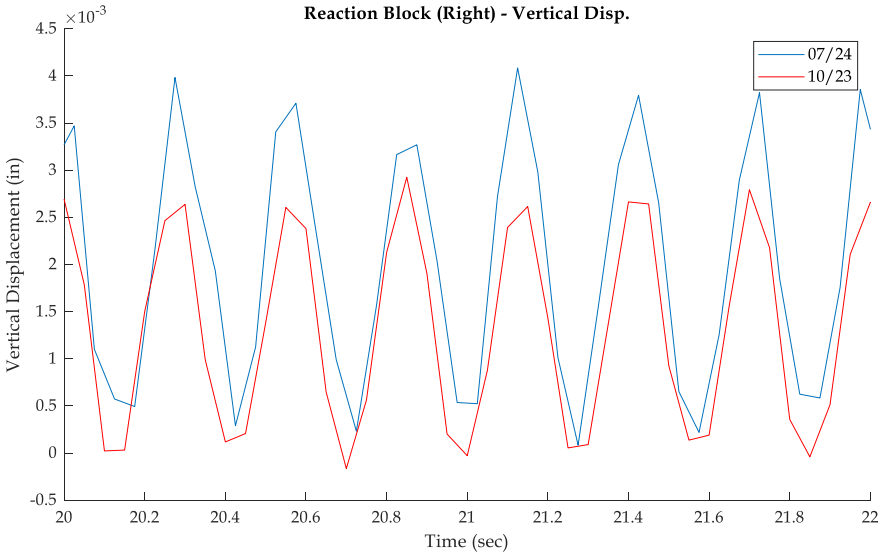

Figure 77 - Reaction Block Right - Vertical Displacement

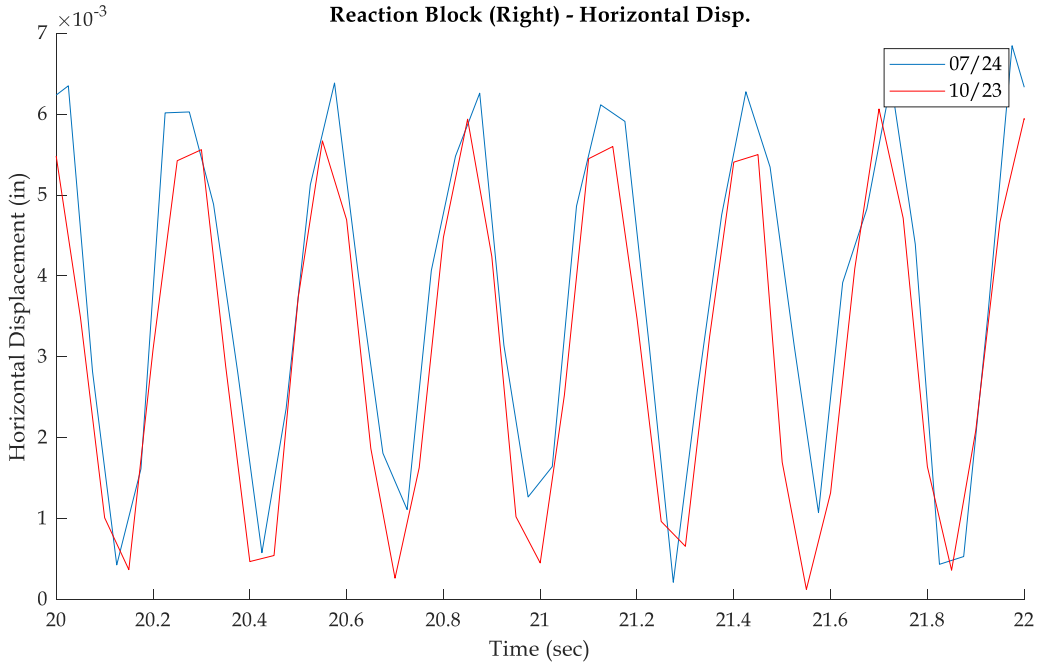

Figure 78 - Reaction Block Right - Horizontal Displacement

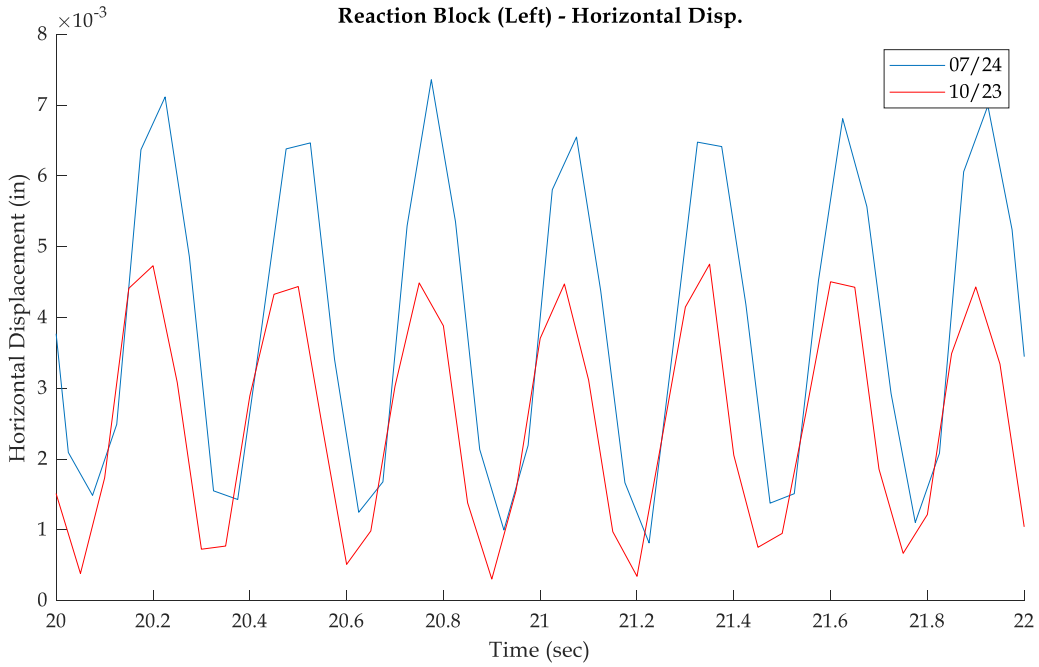

Figure 79 - Reaction Block Left - Horizontal Displacement

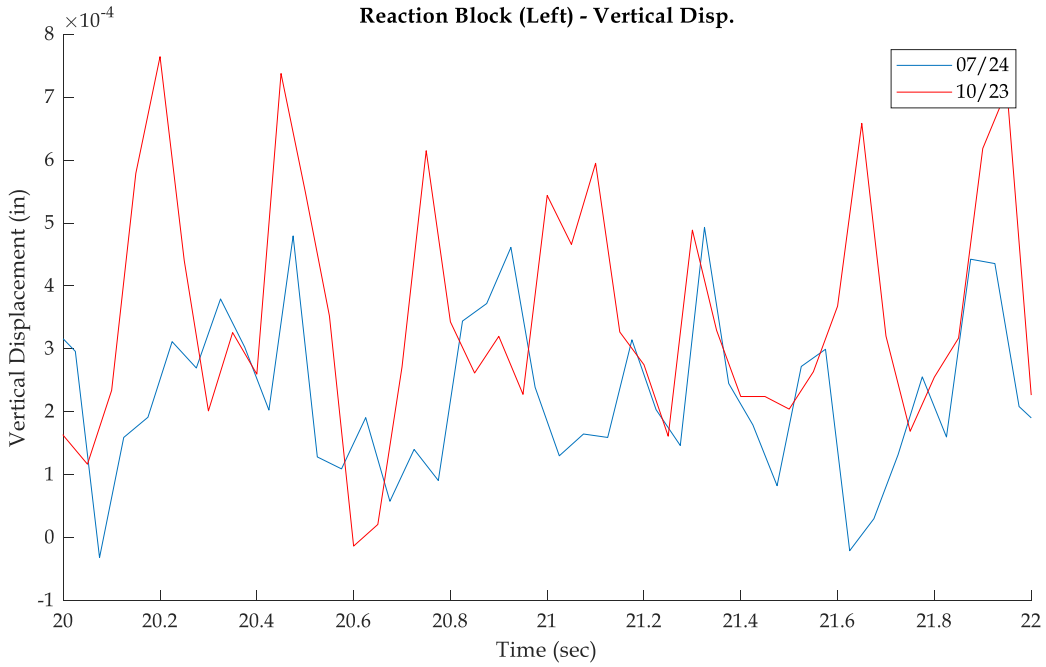

Figure 80 - Reaction Block Left - Vertical Displacement

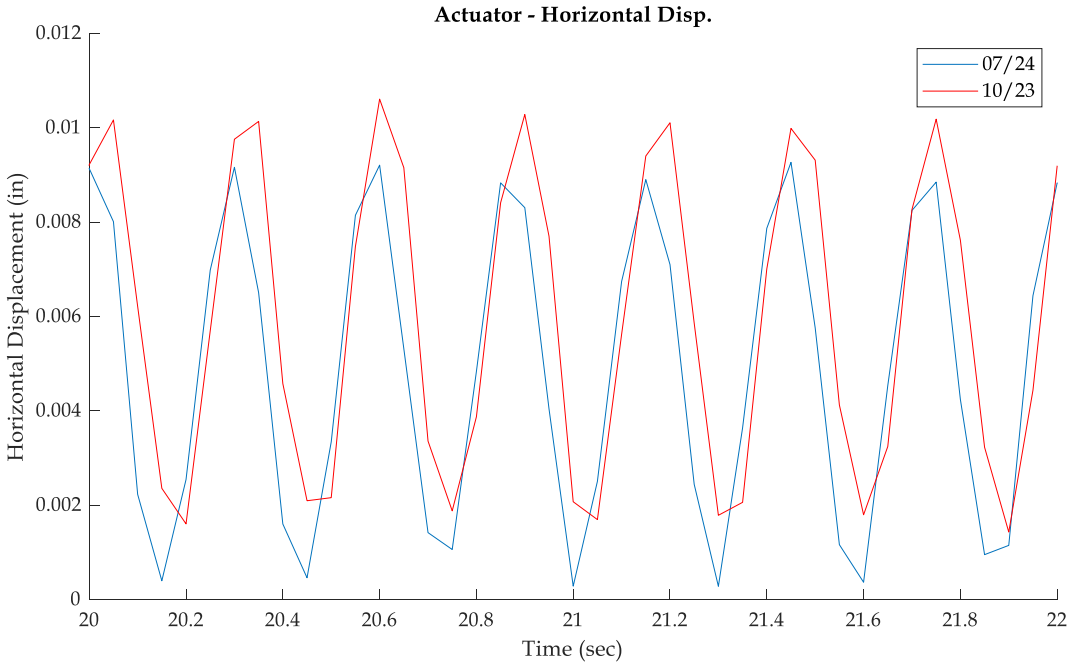

Figure 81 - Actuator - Horizontal Displacement

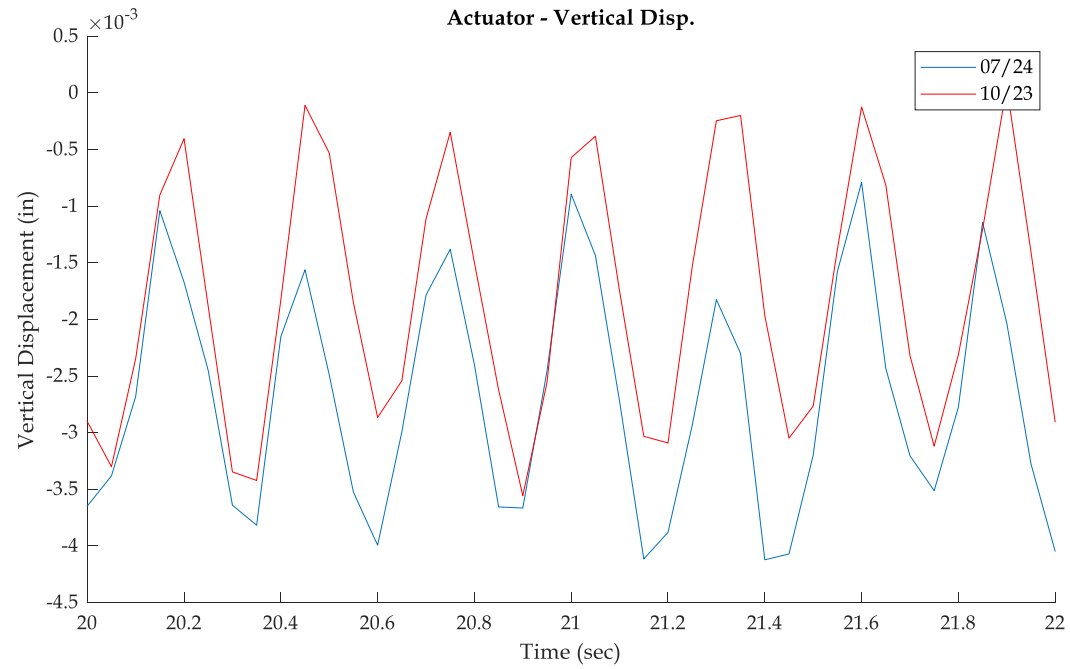

Figure 83 - Actuator - Vertical Displacement

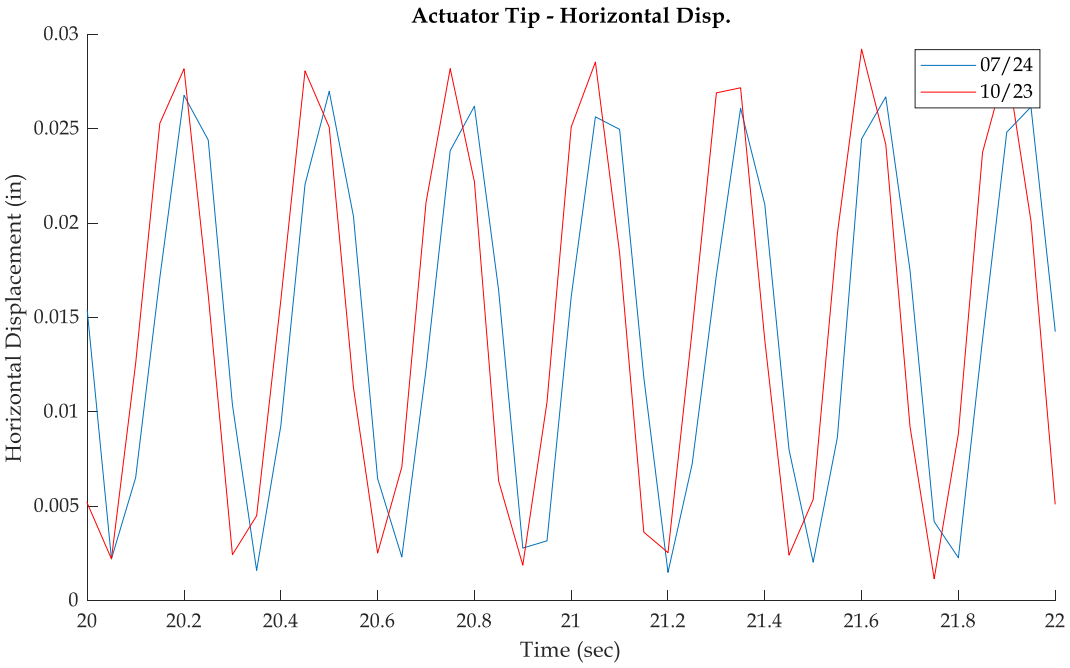

Figure 82 - Actuator Tip - Horizontal Displacement.

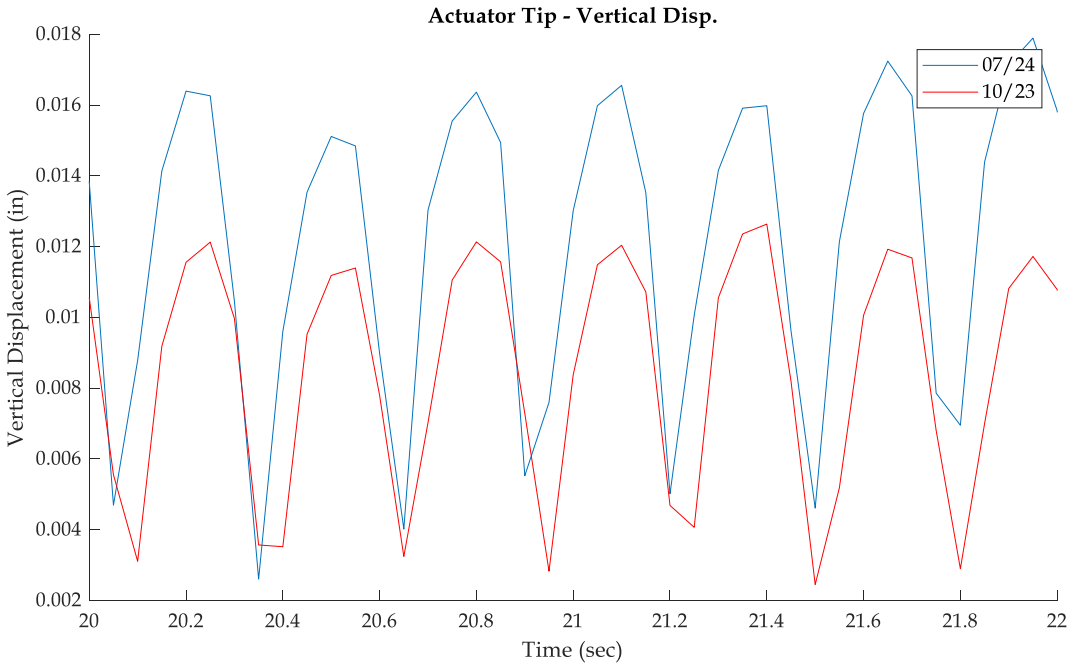

Figure 85 - Actuator Tip - Vertical Displacement

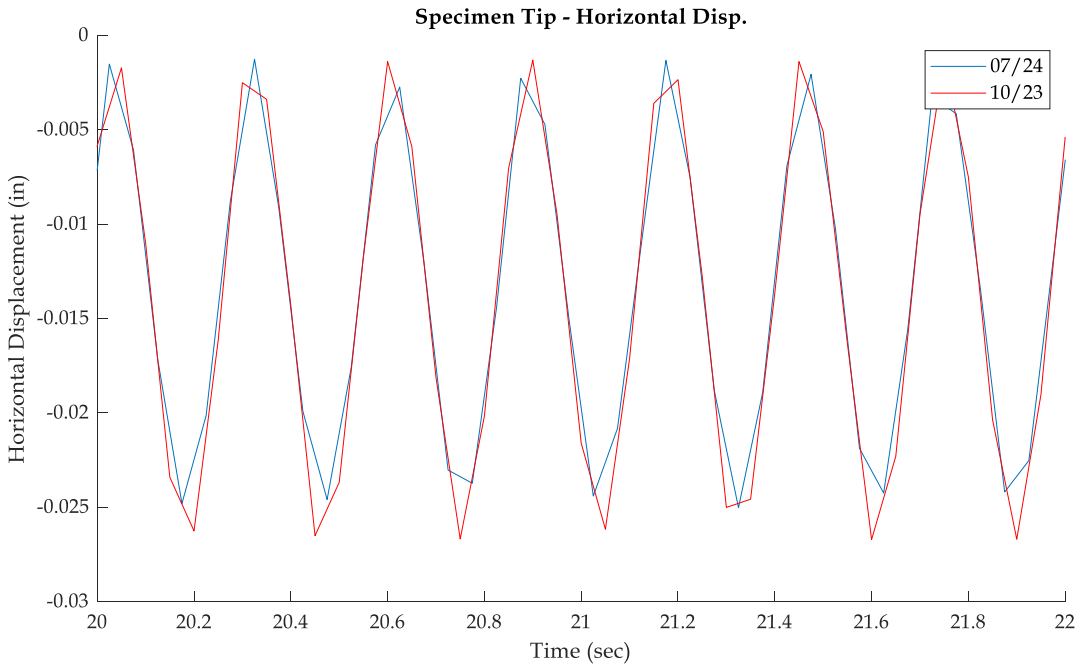

Figure 84 - Specimen Tip - Horizontal Displacement

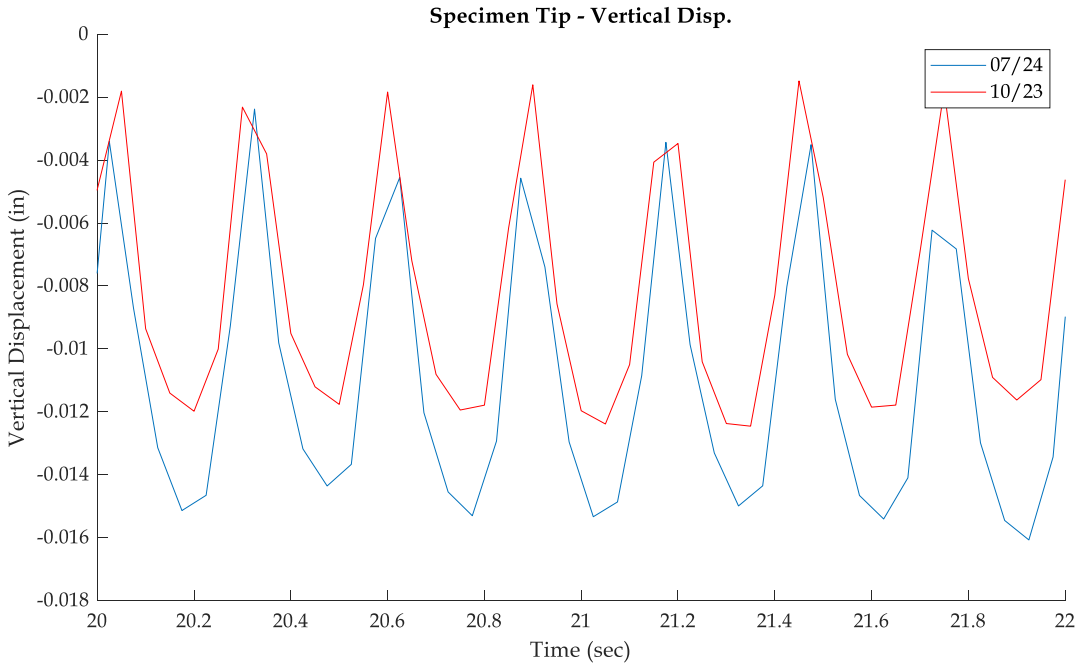

Figure 87 - Specimen Tip - Vertical Displacement

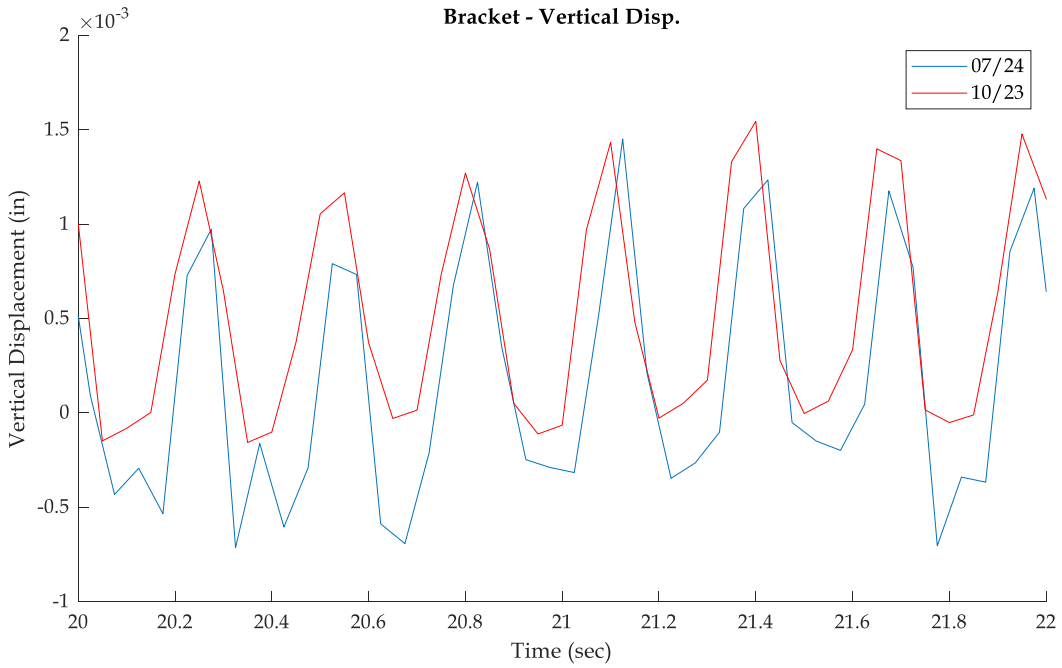

Figure 86 - Bracket - Vertical Displacement

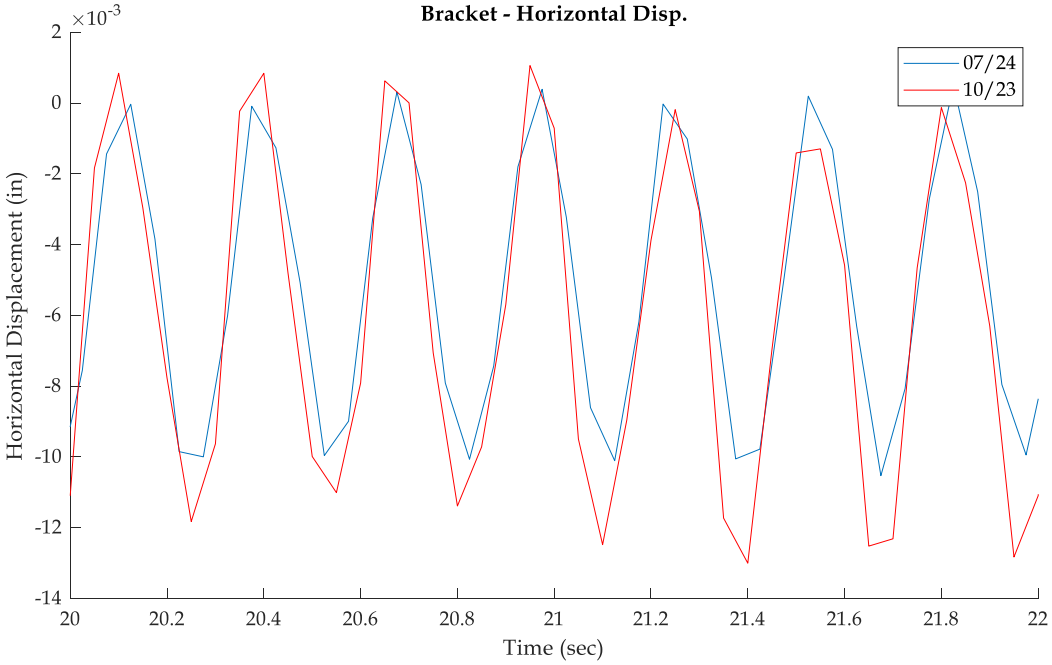

Figure 88 - Bracket - Horizontal Displacement

APPENDIX D – FATIGUE RESULTS

In this appendix, additional plots of the strain gauge response from the fatigue testing will be presented. The figures shown will show all comparisons between the three testing windows discussed in chapter 5.

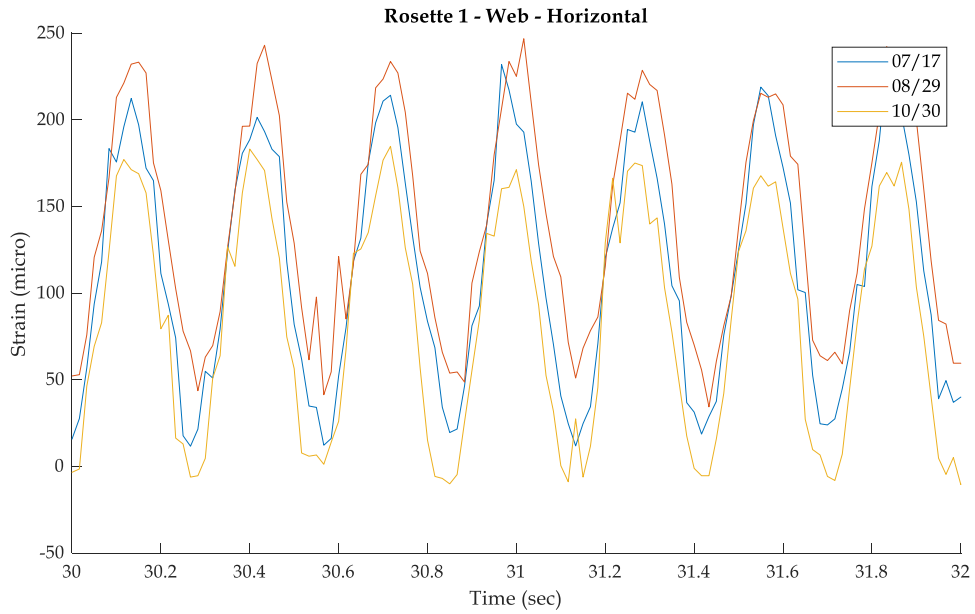

Figure 90 - NRW1 - Horizontal

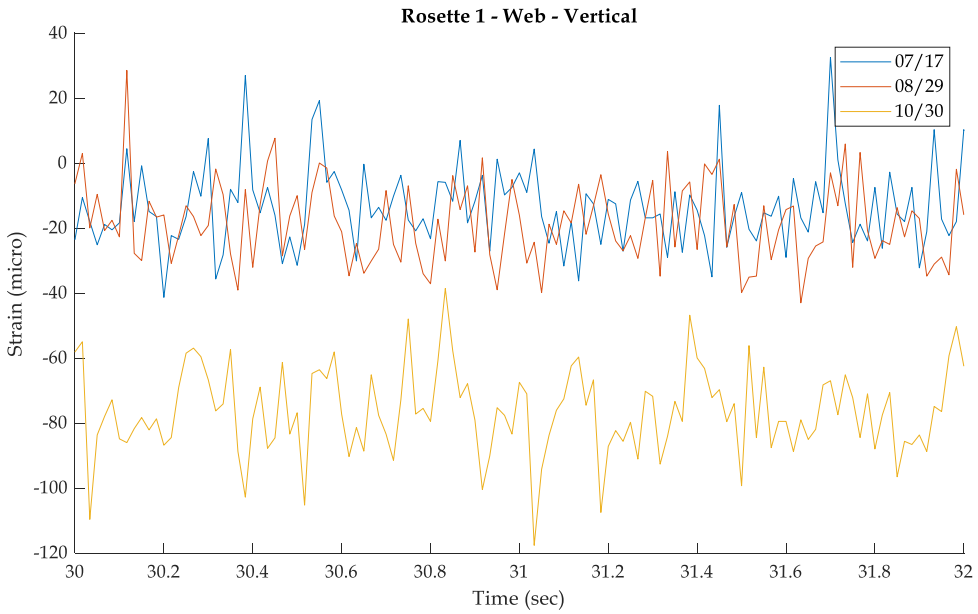

Figure 89 - NRW1 - Vertical

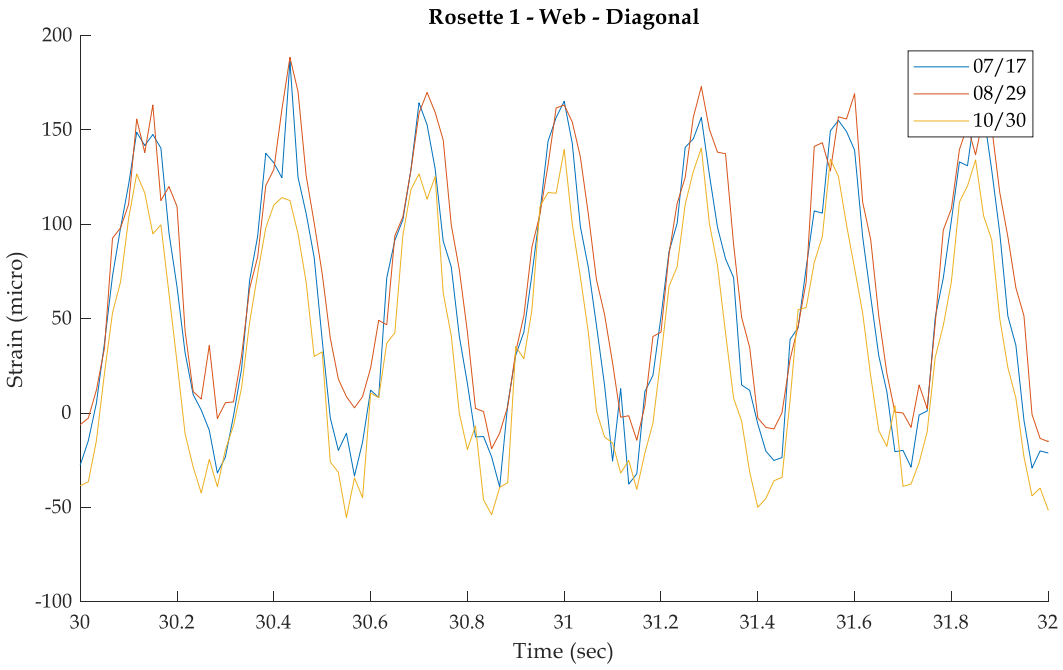

Figure 91 - NRW1 - Diagonal

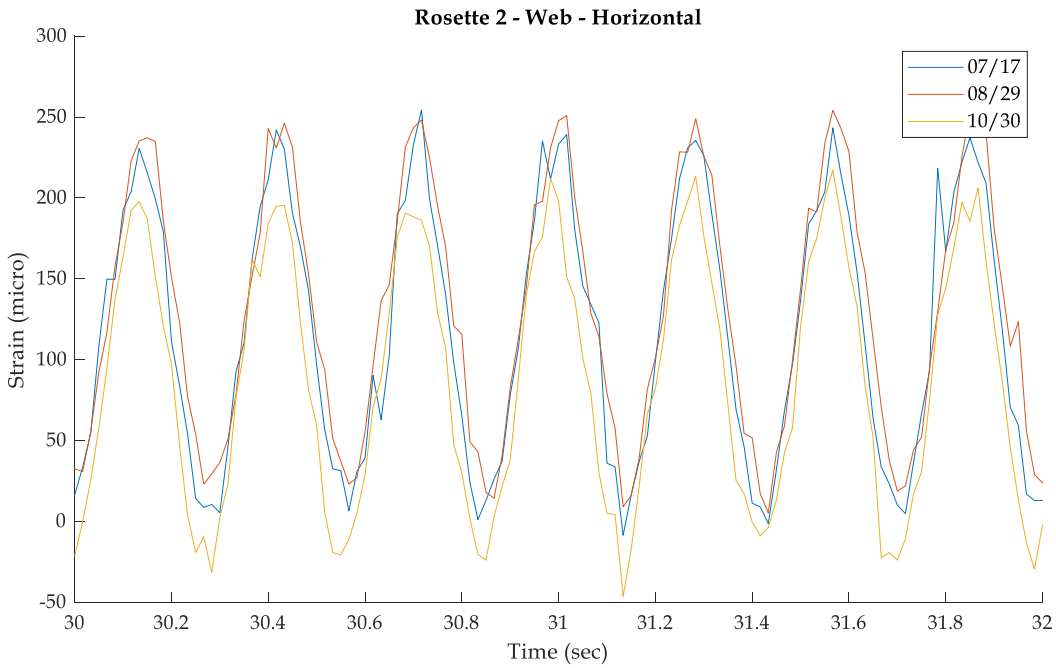

Figure 92 - NRW2 - Horizontal

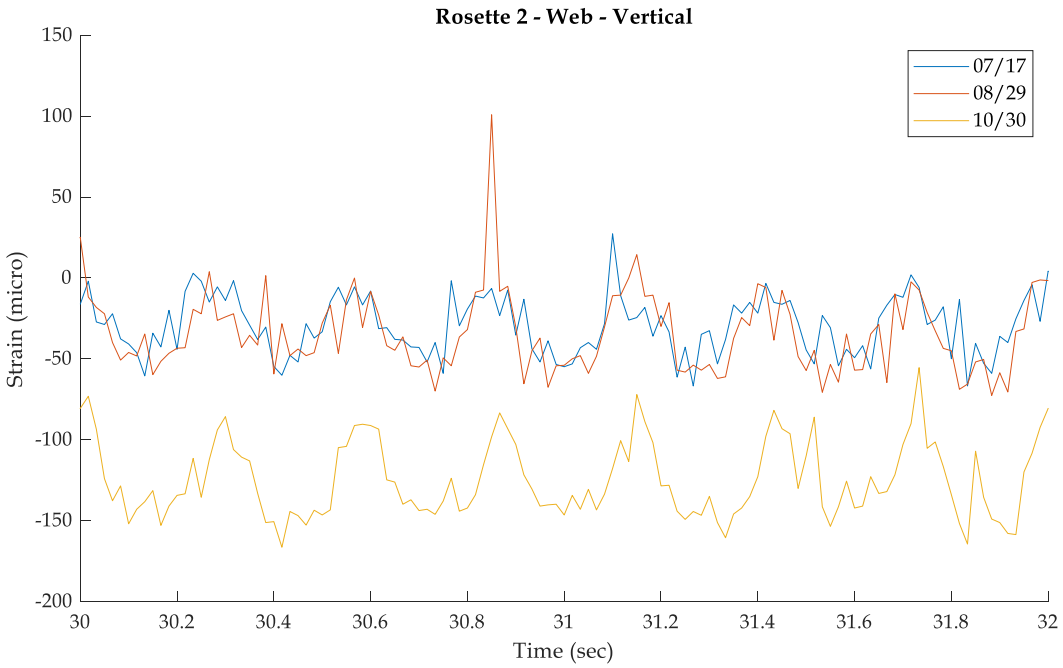

Figure 93 - NRW2 - Vertical

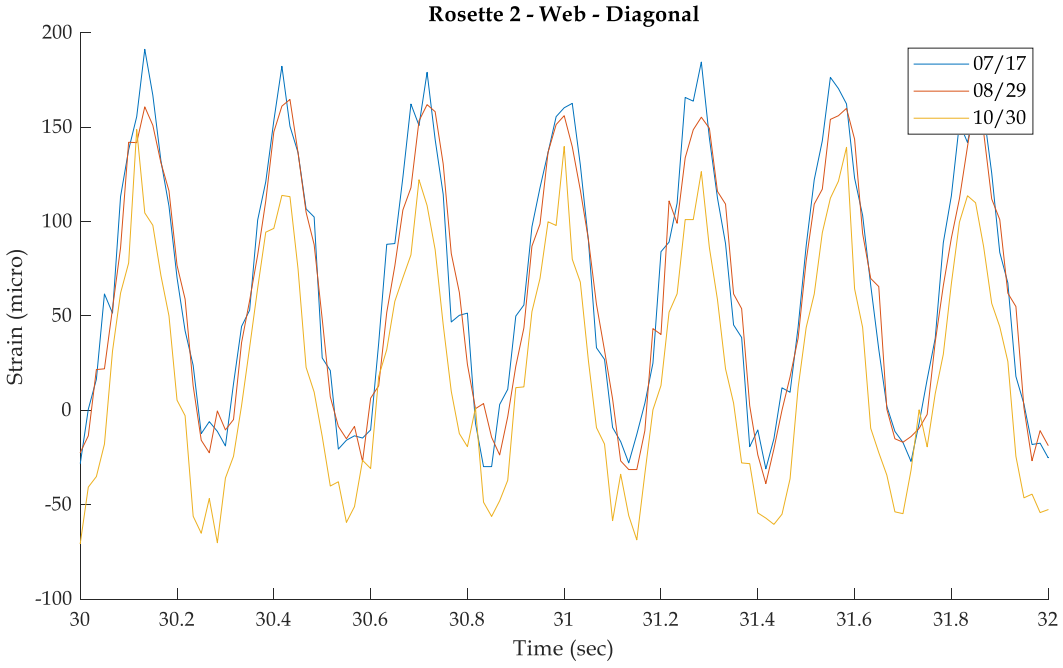

Figure 94 - NRW2 - Diagonal

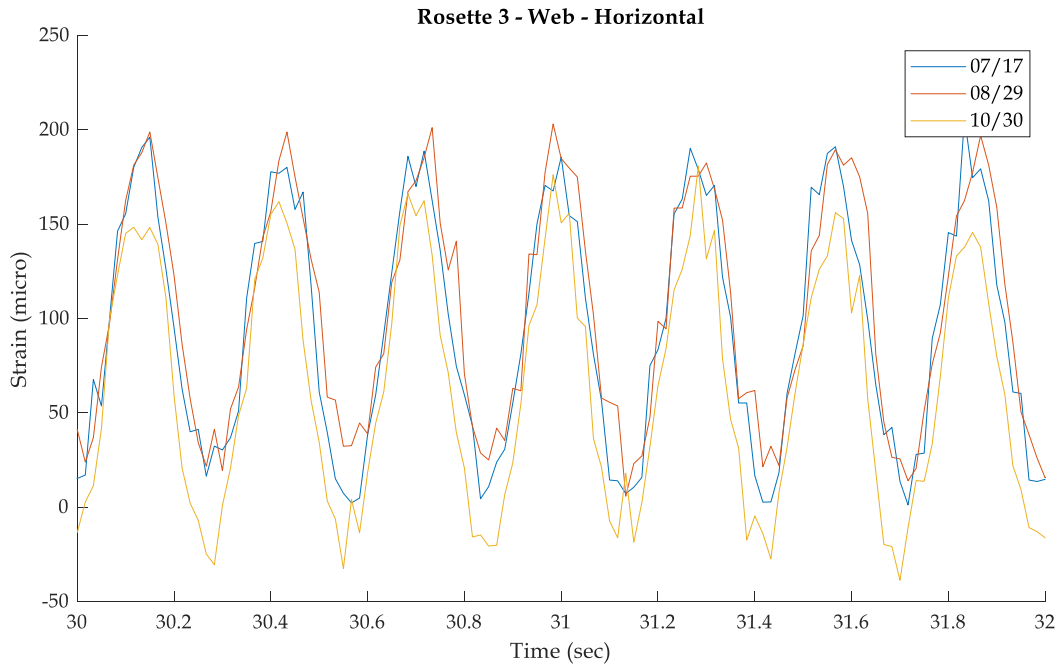

Figure 95 - NRW3 - Horizontal

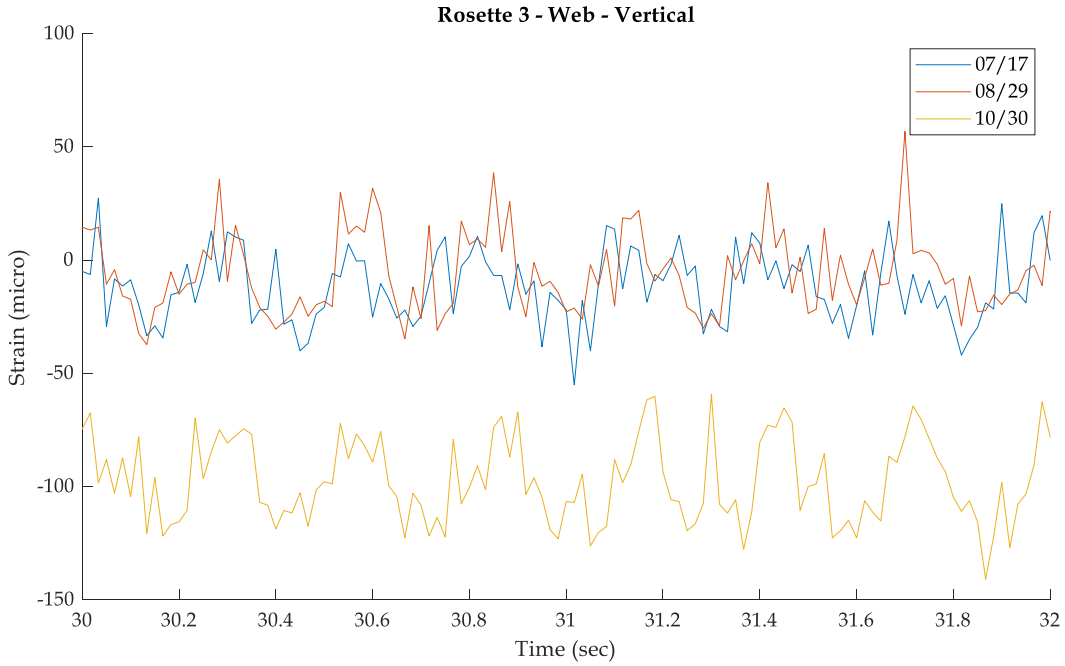

Figure 96 - NRW3 - Vertical

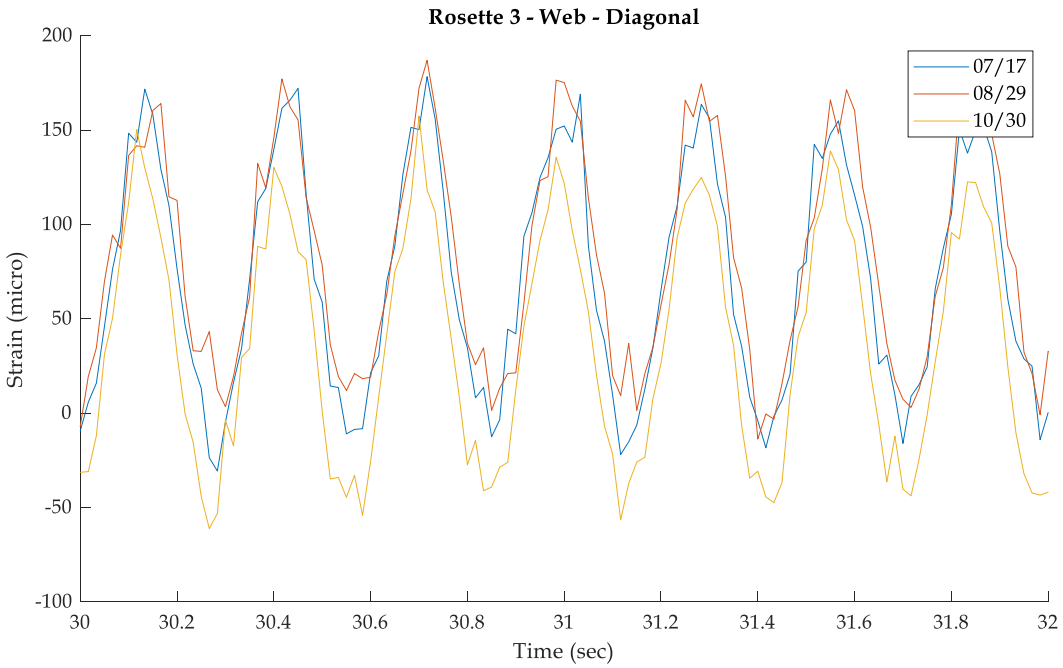

Figure 97 - NRW3 - Diagonal

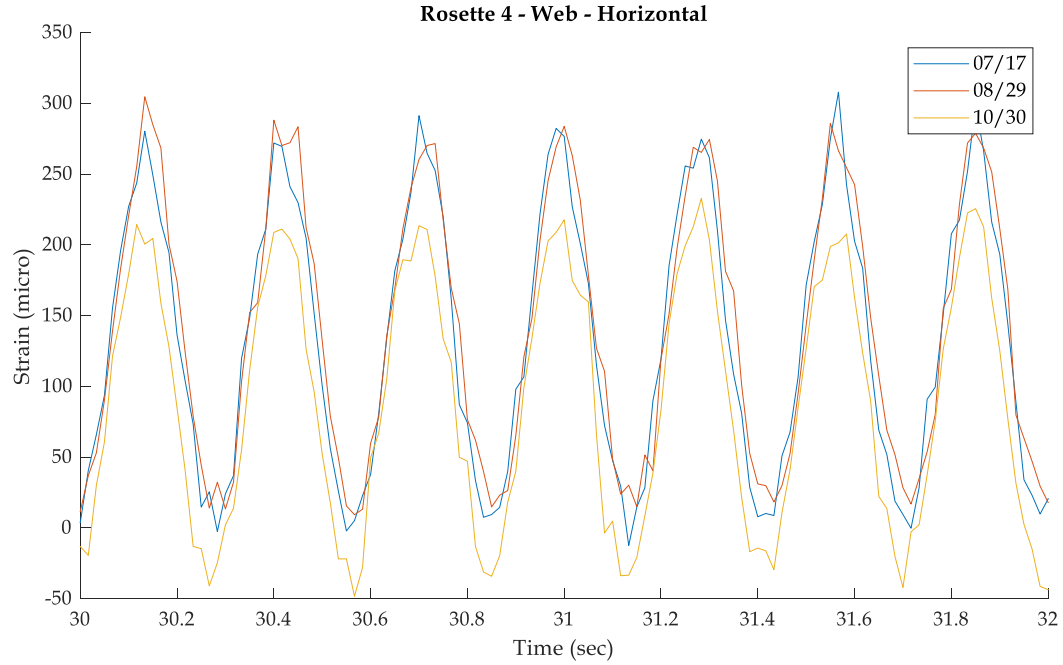

Figure 98 - NRW4 - Horizontal

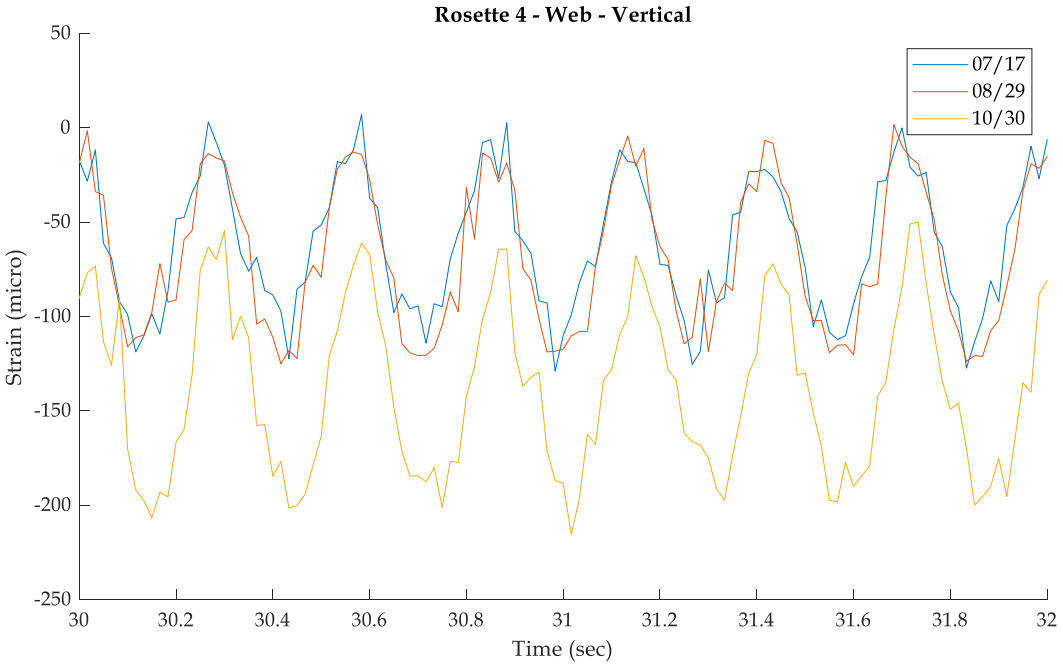

Figure 99 - NRW4 - Vertical

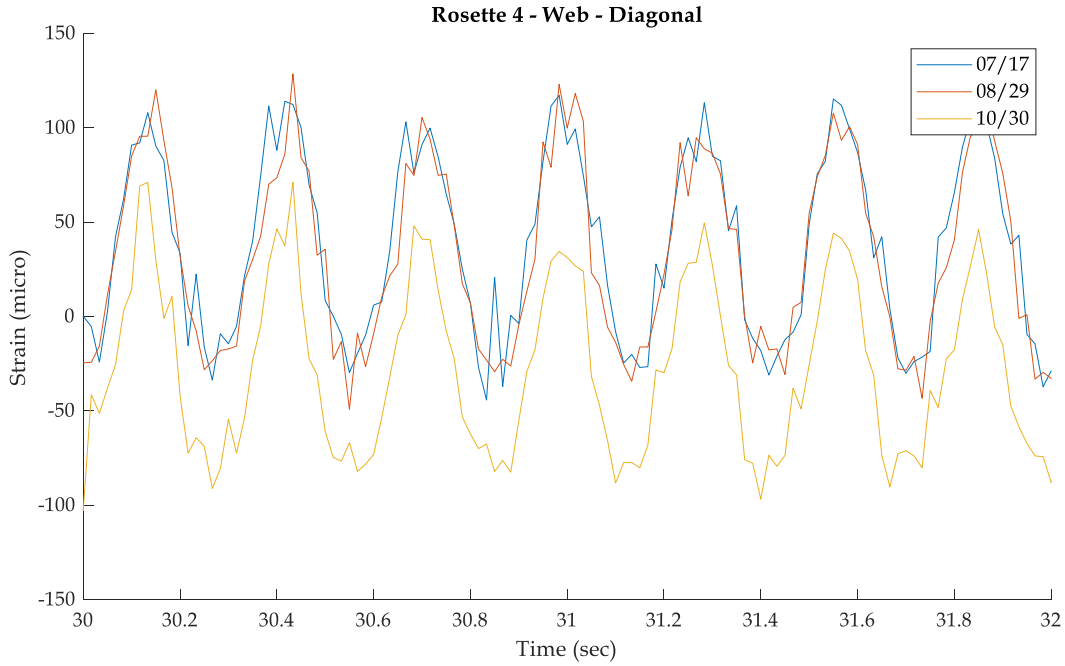

Figure 100 - NRW4 - Diagonal

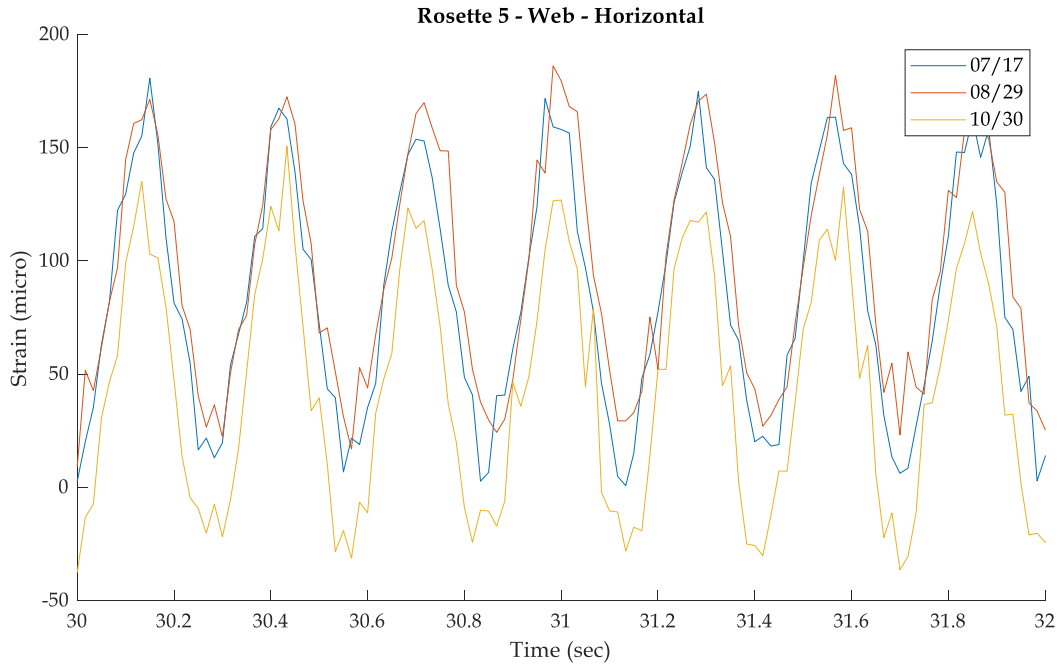

Figure 101 - NRW5 - Horizontal

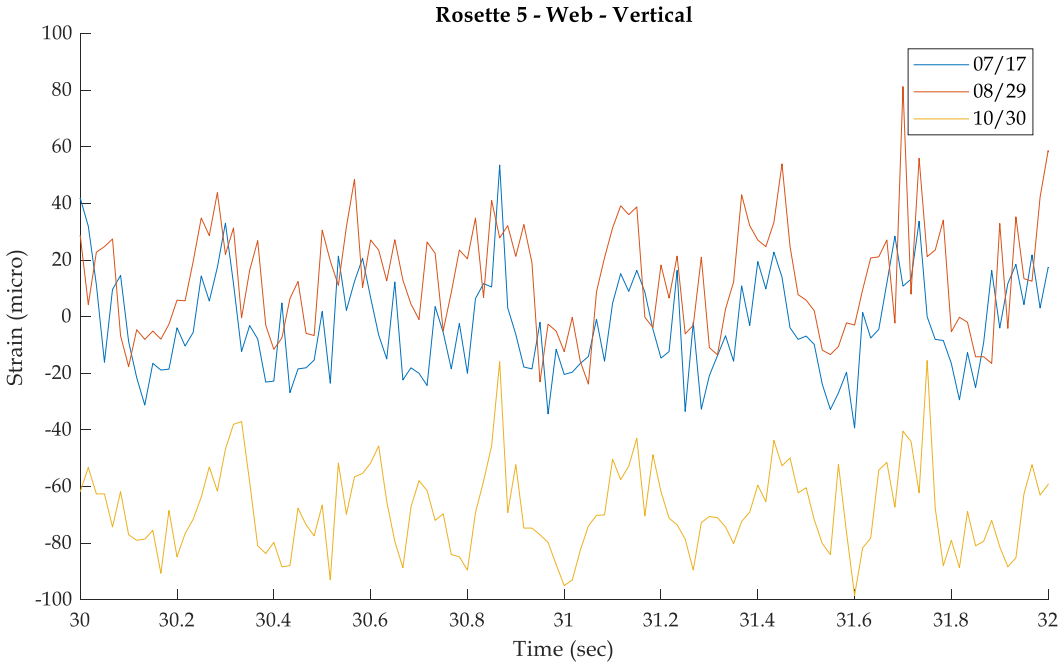

Figure 102 - NRW5 - Vertical

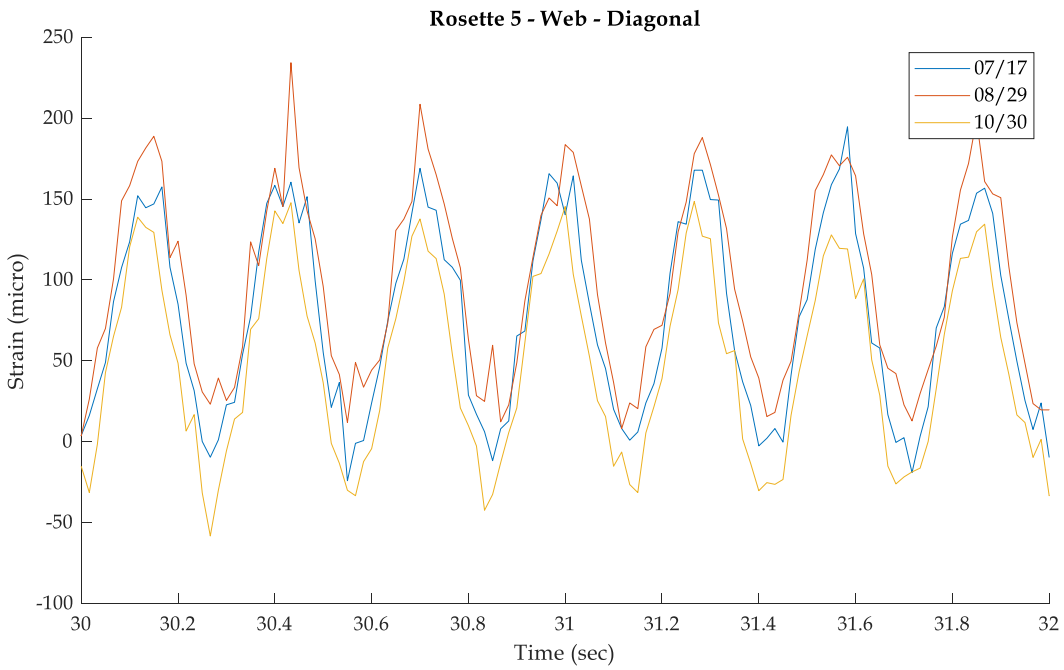

Figure 103 - NRW5 - Diagonal

APPENDIX E – RESIDUAL STRESS CODE

The following Appendix presents the MATLAB code developed to calculate residual stresses using the integral method presented in ASTM E837-13a.

```
%% Residual Stress Computations - Non-uniform Stress - ASTM e837 13a%%
% Author : Duncan W. McGeehan
% Version: Compact - 11/30/18
%%
clearvars
clc
mkdir(pwd,'Plots') % Make directory to store plotted figures
E = 29000; % Modulus of Elasticity Ksi
v = 0.290; %Poisson's Ratio
Hole_depth = 2; %Final depth of drilled hole (mm)
Hole_diameter = 1.66; %Final diameter of drilled hole (mm)
increments = 40; %number of increments for total hole depth assuming the same increments were used across entire depth
ipd = round(increments/Hole_depth,0); %increments per 1st mm of depth
ipdr = 20/ipd; %ipd to calibration matrix size ratio
gauge_D = 5.13; % nominal diameter of gauge (mm)
load('Strain Vectors.mat')  %import correctly formatted strain gauge data
%% Smoothing Strains
e1s = smooth(e1);
e2s = smooth(e2);
e3s = smooth(e3);
 %% Plot Strains to inspect for errors and compare to smoothed strains
 clc
 Title = 'Strain Relieved - Absolute';
 figure
 hold all
 plot(e1*10^6)
 plot(e2*10^6)
 plot(e3*10^6)
 plot(e1s*10^6)
 plot(e2s*10^6)
 plot(e3s*10^6)
 yL=ylabel('Strain (micro)');
 xL=xlabel('Increment');
 ttl=title(Title);
 lgd=legend('e1', 'e2', 'e3','e1s', 'e2s', 'e3s');
 ax=gca;
 ttl.FontSize = 12; xL.FontSize = 12; yL.FontSize = xL.FontSize;
 ttl.FontName = 'Book Antiqua';xL.FontName = 'Book Antiqua'; yL.FontName = 'Book Antiqua';
 lgd.FontName = 'Book Antiqua'; ax.FontName = 'Book Antiqua';
 lgd.FontSize = 11;ax.FontSize = 11;
 hold off
     saveas(gca,[pwd '\Plots\' Title '.fig']);
 %% Smooth or Don't Smooth
 % choose to use the smoothed strains if needed
 e1 = e1s;
 e2 = e2s;
 e3 = e3s;
 %% Combination Strain Vectors
 p_raw = (e3+e1)/2;
 q_raw = (e3-e1)/2;
 t_raw = (e3+e1-2*e2)/2;
%% Correcting the strain vectors for depth of calibration matrix
if (ipdr<=1)
    p = p_raw(ipdr^-1:ipdr^-1:ipd);
    q = q_raw(ipdr^-1:ipdr^-1:ipd);
    t = t_raw(ipdr^-1:ipdr^-1:ipd);
else
    p = p_raw(1:ipd);
    q = q_raw(1:ipd);
    t = t_raw(1:ipd);
end
```

Figure 104 - MATLAB Code 1

```
%% Computer Standard error in the combination strains
pp = zeros(ipd-3,1);
qq = zeros(ipd-3,1);
tt = zeros(ipd-3,1);
for k = 1:(ipd-3)
    pp(k,1)=(((p(k)-3*p(k+1)+3*p(k+2)-p(k+3))^2))/((20*(ipd-3)));
    qq(k,1)=(((q(k)-3*q(k+1)+3*q(k+2)-q(k+3))^2))/((20*(ipd-3)));
    tt(k,1)=(((t(k)-3*t(k+1)+3*t(k+2)-t(k+3))^2))/((20*(ipd-3)));
end
Pstd = sum(pp);
Qstd = sum(qq);
Tstd = sum(tt);
```

```
%% Importing Calibration matrices
load ('Calibration Matrix - Non-Uniform.mat') %Import the calibration matrices a and b for type A rosette from ASTM e837-13a
% adjust for diameter of hole
a_adj = a_raw*((Hole_diameter/2)^2);
b_adj = b_raw*((Hole_diameter/2)^2);
%adjust the size of the calibration matrices to match the strain vectors
if (ipdr<=1)
    a=a_adj;
    b=b_adj;
    c=c_raw;
else
   a = zeros(ipd,ipd);
   b = zeros(ipd,ipd);
    for ii = 1:ipd
        for jj = 1:ipd
            a(ii,jj)=sum(a_adj(ii*ipdr,(jj*ipdr-(ipdr-1)):jj*ipdr));
            b(ii,jj)=sum(b_adj(ii*ipdr,(jj*ipdr-(ipdr-1)):jj*ipdr));
        end
    end
end
%Adjust size of second derivative smoothing matrix
c = c_raw(1:ipd,1:ipd);
c (ipd,:) = zeros;
```

```
%% Check for conformity to ASTM Uniformity percent relieved
% clc
d_d = linspace(0,Hole_depth,increments+1);%vector of depth
d_p = d_d'/gauge_D;%vector of ratio of depth to gauge diameter
%the vectors p_p,q_p,and t_p are the percent strain relieved at each
%increment
p_p = zeros(increments+1,1); p_p(2:increments+1,1) = 100*abs(p_raw)/max(abs((p_raw)));
q_p = zeros(increments+1,1); q_p(2:increments+1,1)= 100*abs(q_raw)/max(abs((q_raw)));
t_p = zeros(increments+1,1); t_p(2:increments+1,1) = 100*abs(t_raw)/max(abs((t_raw)));
```

```
%% Plot Percent Strain relieved vs. Depth/Gauge Diameter
%see if it matches the behavior of the uniform stress state, if yes, a uniform analysis can be performed
clc
Title = 'ASTM Uniformity Check';
figure
hold all
plot(d_p,p_p,'-r')
plot(d_p,q_p,'-m')
plot(d_p,t_p,'-g')
yL=ylabel('Percent Strain Relieved','FontName','Book Antiqua','FontSize',12);
xL=xlabel('Depth/Gauge Diameter','FontName','Book Antiqua','FontSize',12);
ttl=title(Title,'FontName','Book Antiqua','FontSize',12);
lgd=legend('p', 'q', 't');
ax=gca;
ttl.FontSize = 12; xL.FontSize = 12; yL.FontSize = xL.FontSize;
ttl.FontName = 'Book Antiqua';xL.FontName = 'Book Antiqua'; yL.FontName = 'Book Antiqua';
lgd.FontName = 'Book Antiqua'; ax.FontName = 'Book Antiqua';
lgd.FontSize = 11;ax.FontSize = 11;
hold off
    saveas(gca,[pwd '\Plots\' Title '.fig']);
```

```
%% Smoothing variables - initial guess
clc
ap = 4*10^-6;
aq = 4*10^-6;
at = 4*10^-6;
```

Figure 105 - MATLAB Code 2

```
%% Residual Stress Vector - P
%iterate until apd<5
    P_Stress = ((a'*a+ap*c'*c)^-1)*(E/(1+v))*a'*p;
    pmis = p-((1+v)/E)*a*P_Stress;
    prms=(1/ipd)*sum(pmis.^2);
    pdiff=100*(1-Pstd/prms);
    ap = (Pstd/prms)*ap
    apd = abs(pdiff)
%% Residual Stress Vector - Q
%iterate until aqd<5
    Q_Stress = ((b'*b+aq*c'*c)^-1)*(E*b')*q;
    qmis = q-(1/E)*b*Q_Stress;
    qrms=(1/ipd)*sum(qmis.^2);
    qdiff=100*(1-Qstd/qrms);
    aq = (Qstd/qrms)*aq
    aqd = abs(qdiff)
%% Residual Stress Vector - P
%iterate until atd<5
    T_Stress = ((b'*b+at*c'*c)^-1)*(E*b')*t;
    tmis = t-(1/E)*b*T_Stress;
    trms=(1/ipd)*sum(tmis.^2);
    tdiff=100*(1-Tstd/trms);
    at = (Tstd/trms)*at
    atd = abs(tdiff)
%% Plot Combination Stress Vectors
Title = 'Stress Vectors vs. Depth';
figure
hold all
plot(P_Stress,-d_d(2:ipd+1))
plot(Q_Stress,-d_d(2:ipd+1))
plot(T_Stress,-d_d(2:ipd+1))
yL=ylabel('Depth(mm)');
xL=xlabel('Stress (ksi)');
ttl=title(Title);
lgd=legend('P', 'Q', 'T');
ax=gca;
ttl.FontSize = 12; xL.FontSize = 12; yL.FontSize = xL.FontSize;
ttl.FontName = 'Book Antiqua';xL.FontName = 'Book Antiqua'; yL.FontName = 'Book Antiqua';
lgd.FontName = 'Book Antiqua'; ax.FontName = 'Book Antiqua';
lgd.FontSize = 11;ax.FontSize = 11;
hold off
    saveas(gca,[pwd '\Plots\' Title '.fig']);
%% Convert Combination Stresses to Cartesian Stresses
Fxx = P_Stress-Q_Stress;
Fyy = P_Stress+Q_Stress;
Fxy = T_Stress;

% Principal Stresses
Fmax = P_Stress+sqrt(Q_Stress.^2+T_Stress.^2);
Fmin = P_Stress-sqrt(Q_Stress.^2+T_Stress.^2);
Beta = 2*pi()*.5*atan(-T_Stress./(-Q_Stress)); %angle to axis of principal stress
%% Plot Cartesian Stresses vs. Depth
Title = 'Cartesian Stress Vectors vs. Depth';
figure
hold all
plot(Fxx,-d_d(2:ipd+1),'r')
plot(Fyy,-d_d(2:ipd+1),'k')
plot(Fxy,-d_d(2:ipd+1),'g')

yL=ylabel ('Depth (mm)');
xL=xlabel ('Stress (ksi)');
lgd=legend ('Fxx','Fyy','Fxy');
ttl=title (Title);
ax=gca;
ttl.FontSize = 12; xL.FontSize = 12; yL.FontSize = xL.FontSize;
ttl.FontName = 'Book Antiqua';xL.FontName = 'Book Antiqua'; yL.FontName = 'Book Antiqua';
lgd.FontName = 'Book Antiqua'; ax.FontName = 'Book Antiqua';
lgd.FontSize = 11;ax.FontSize = 11;
    saveas(gca,[pwd '\Plots\' Title '.fig']);
hold off
```

Figure 106 - MATLAB Code 3

```
%% Plot Principal Stress vs. Depth
Title = 'Principal Stress Vectors vs. Depth';
figure
hold all
plot(Fmax,-d_d(2:ipd+1),'r')
plot(Fmin,-d_d(2:ipd+1),'k')
yL=ylabel ('Depth (mm)');
xL=xlabel ('Stress (ksi)');
lgd=legend ('Fmax','Fmin');
ttl=title (Title);
ax=gca;
ttl.FontSize = 12; xL.FontSize = 12; yL.FontSize = xL.FontSize;
ttl.FontName = 'Book Antiqua';xL.FontName = 'Book Antiqua'; yL.FontName = 'Book Antiqua';
lgd.FontName = 'Book Antiqua'; ax.FontName = 'Book Antiqua';
lgd.FontSize = 11;ax.FontSize = 11;
    saveas(gca,[pwd '\Plots\' Title '.fig']);
hold off
%% Save Calculated Stress Vectors
save('Calculated Stress Profile','Fxx','Fyy','Fxy','Fmax','Fmin','Beta')

%% Plot Stresses at a depth offset
Title = 'Cartesian Stress Vectors vs. Depth - Offset';
figure
hold all
ll = 1; ul=20; % ll = first increment to start plot at, ul = final increment to plot
plot(Fxx(ll:ul),-d_d(1+ll:ul+1),'r')
plot(Fyy(ll:ul),-d_d(1+ll:ul+1),'k')
plot(Fxy(ll:ul),-d_d(1+ll:ul+1),'g')
yL=ylabel ('Depth (mm)');
xL=xlabel ('Stress (ksi)');
lgd=legend ('Fxx','Fyy','Fxy');
ttl=title (Title);
ax=gca;
ttl.FontSize = 12; xL.FontSize = 12; yL.FontSize = xL.FontSize;
ttl.FontName = 'Book Antiqua';xL.FontName = 'Book Antiqua'; yL.FontName = 'Book Antiqua';
lgd.FontName = 'Book Antiqua'; ax.FontName = 'Book Antiqua';
lgd.FontSize = 11;ax.FontSize = 11;
    saveas(gca,[pwd '\Plots\' Title '.fig']);
hold off
```

Figure 107 - MATLAB Code 4

APPENDIX F – RESIDUAL STRESS RESULTS

This appendix will present the measured strains relieved, and the resulting calculated stresses from each of the holes drilled in this study. The following table provides a numbered list of the measurements made during this study with a brief description and some of the characteristic parameters.

Table 11 - Residual Stress Table of Measurements

#	Specimen	Description	Loading	Drilling Method	Hole Diameter (mm)	Hole Depth (mm)	Calc. increments	Total Increments
1	Gussetless 1	Underside of the top flange (left) near the diagonal termination. The hole is significantly far from the weld area. The specimen was on the ground and the 2mm was drilled in 10 equal depth increments	None	Plunge	1.66	2	5	10
2	Gussetless 1	Topside of the top flange (left) near the diagonal termination. The hole is in the same location as Res_in - 10i2mm but on the topside of the flange. The specimen was on the ground and the 2mm was drilled in 20 equal depth increments	None	Plunge	1.66	2	10	20
3	Gussetless 1	Topside of top flange (left), the location is close to the beginning of the curved section (measured in the curved section). It is placed away from the edge and the weld area similarly to the res_in and res_out measurements. The hole was drilled 2mm in 20 equal depth steps	Bolted	Plunge	1.66	2	10	20
4	Gussetless 1	Topside of top flange (left), the location is close to the baseline measurement but advanced further away from the flat portion of the flange. It is placed away from the edge and the weld area similarly to the res_in and res_out measurements. The hole was drilled 1mm in 20 equal depth steps. At 1mm the drill bit sheared off and the measurements were stopped.	Bolted	Plunge	1.66	1	20	20
5	Flat Plate - Flange Steel	The hole was drilled in the center of a flat plate made of the flange material from the gussetless specimen. The hole was drilled 2mm in 40 equal increments, but there was a discontinuity in the measured strain after the 20th increment.	None	Plunge	1.66	2	20	40
6	Flat Plate - Flange Steel	Hole drilled close to center of flange flat plate. The hole was drilled 2mm in 40 equal increments.	None	Plunge	1.66	2	20	40
7	Flat Plate - Annealed Steel	Hole drilled in the center of the "annealed" steel plate. Drilled 2mm in 40 increments.	None	Plunge	1.66	2	20	40
8	Flat Plate - Steel	Hole drilled in actuator transfer plate (for green frame). 2mm in 40 increments. Orbital method.	None	Orbital	2.045	2	20	40
9	Flat Plate - Annealed Steel	Center of annelead plate. Orbital method 20 increments for first 1mm, 10 increments for following 1mm.	None	Orbital	2.045	2	20	30
10	Gussetless 1	Hole drilled on top side of top flange (left). This measurement was in the same line as the previous top flange but moved further up the curve. This hole was drilled in 30 increments, the first 20 were evenly spaced across 1mm and the last 10 were evenly spaced across 1mm.	Bolted	Orbital	2.045	2	20	30
11	Gussetless 2	Hole drilled on top side of top flange on specimen two. The location was the same as Res_out -20i2mm.	None	Orbital	2.045	2	20	30

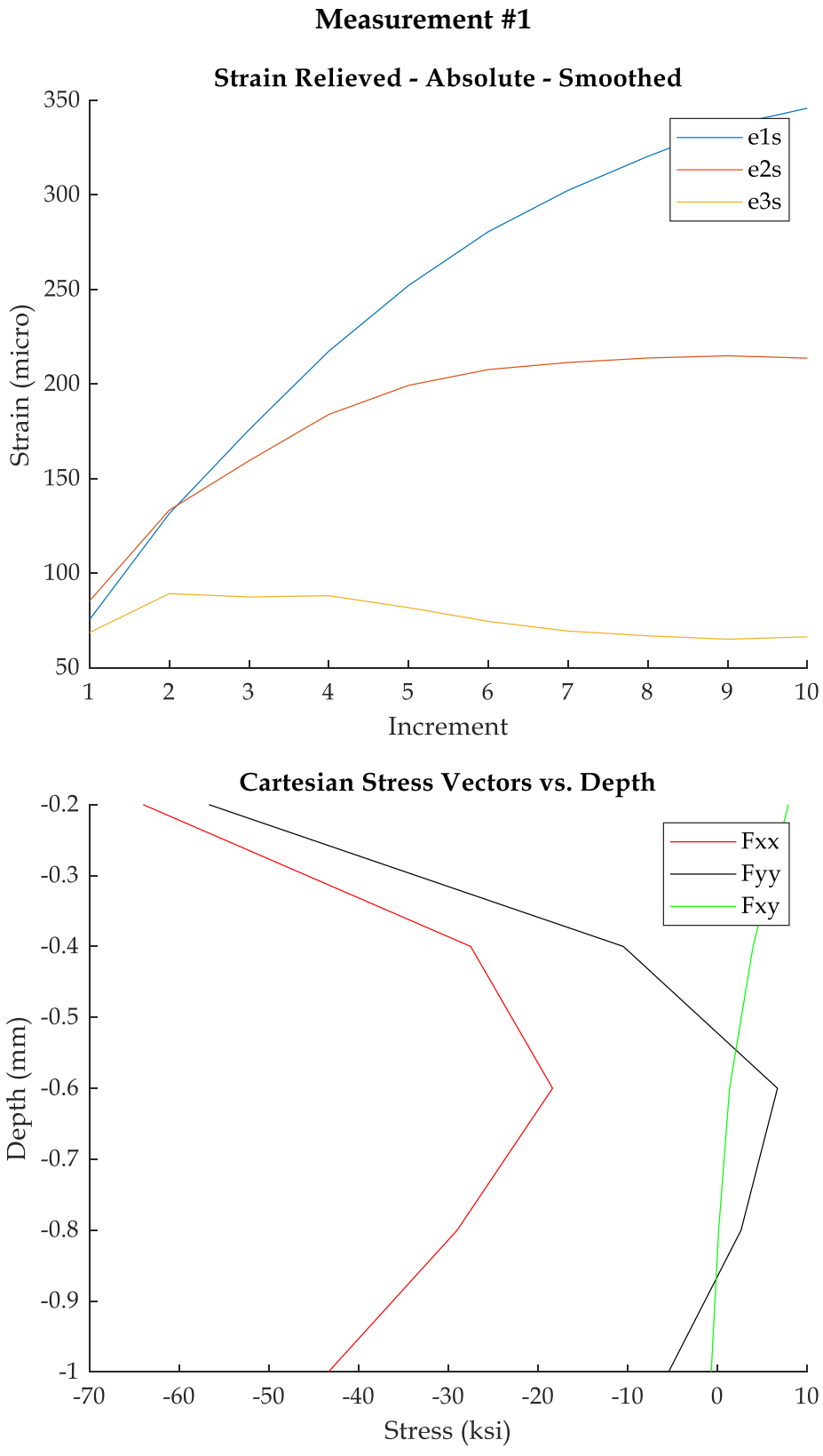

Figure 108 - Residual Stress Measurement #1 - Strain (top) and Stress (bottom)

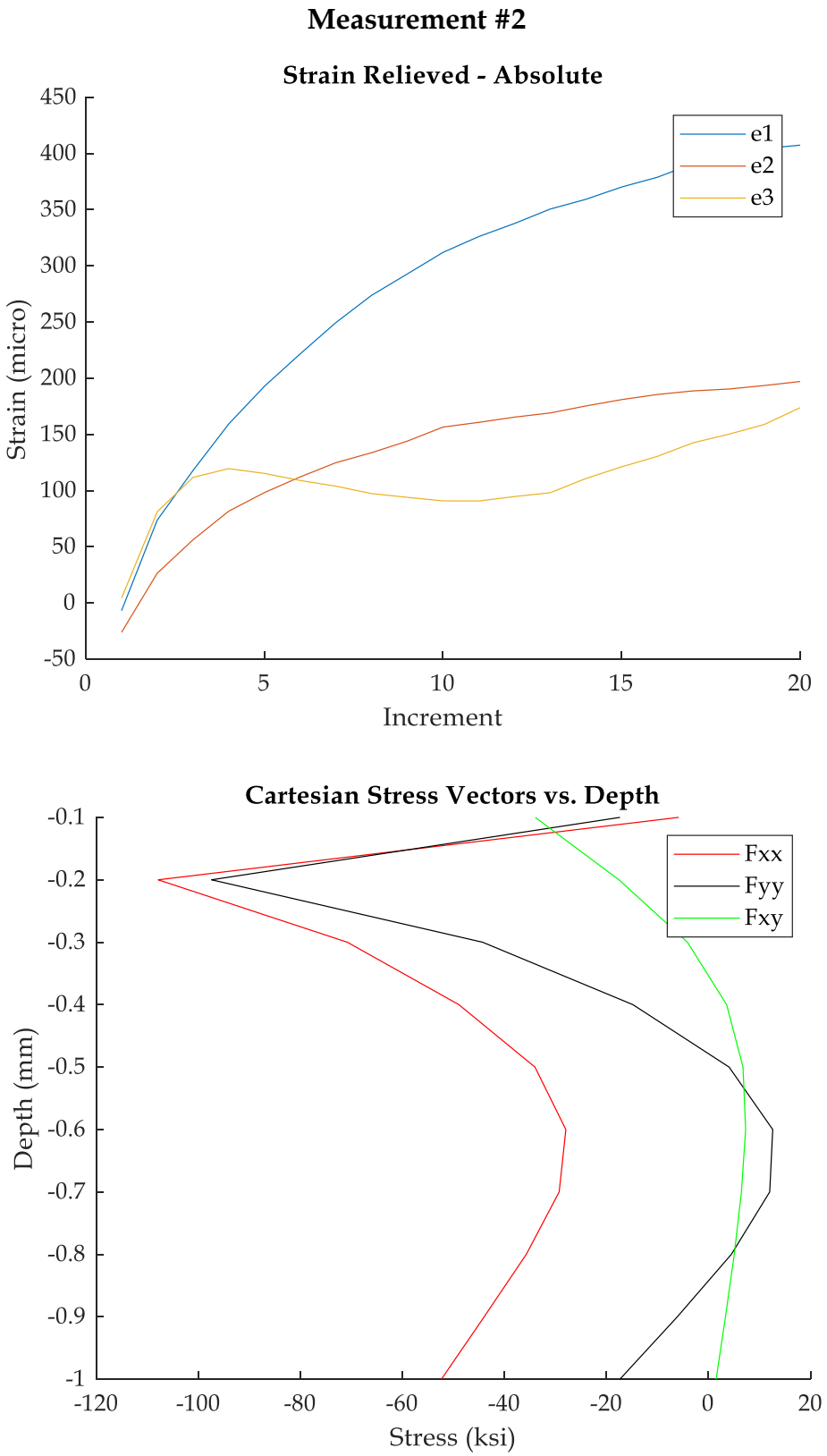

Figure 109 - Residual Stress Measurement #2 - Strain (top) and Stress (bottom)

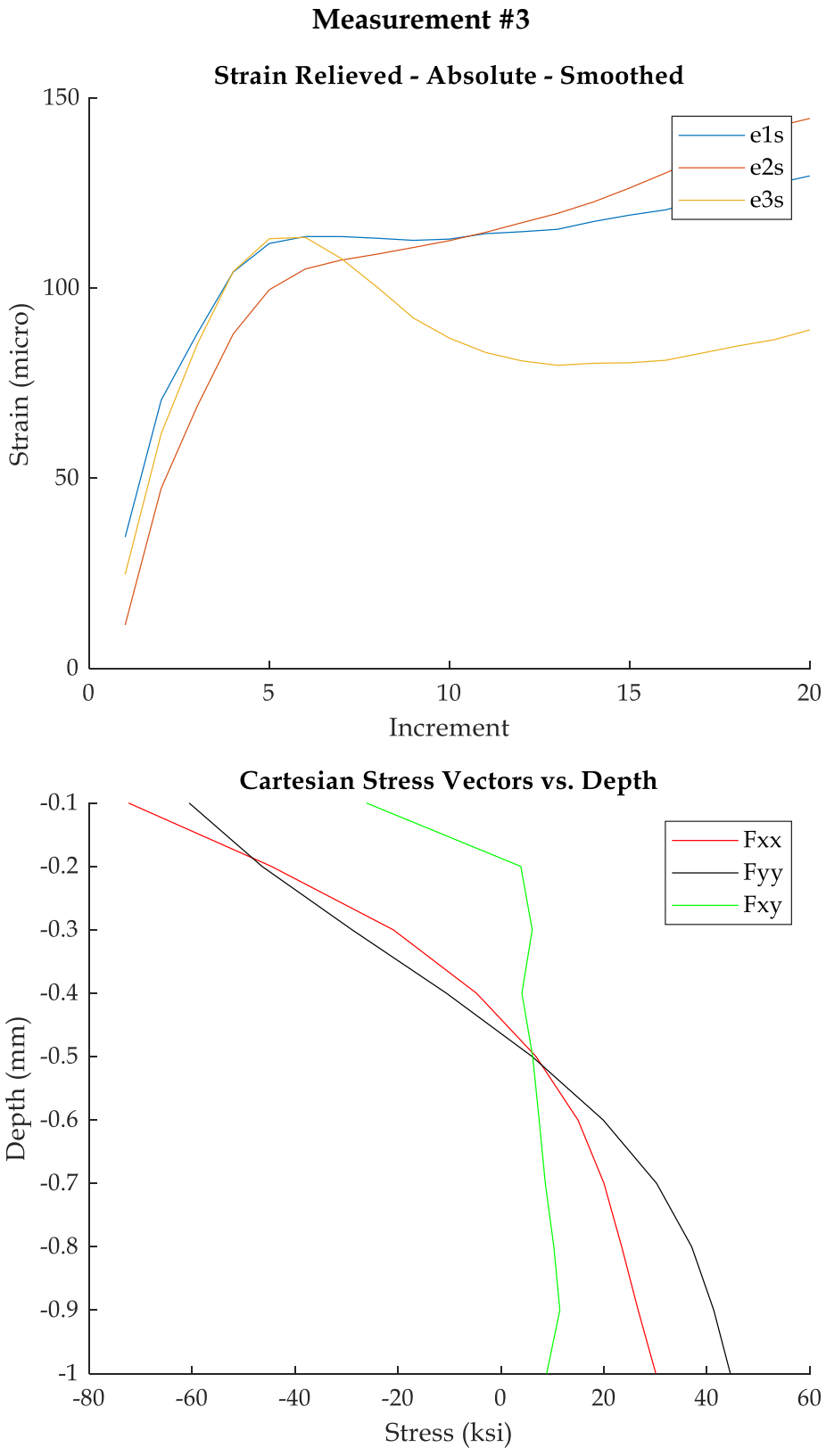

Figure 110 - Residual Stress Measurement #3 - Strain (top) and Stress (bottom)

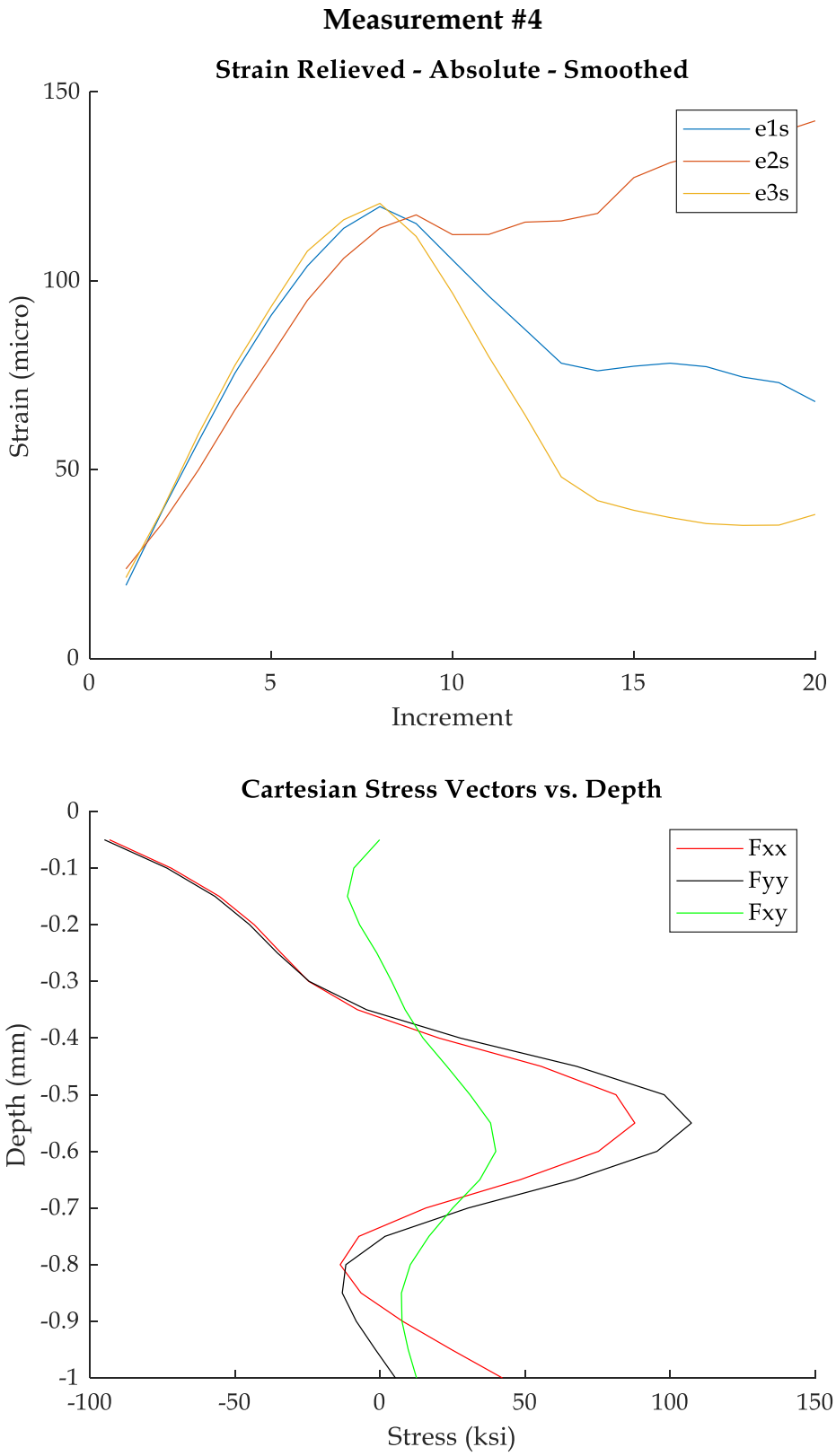

Figure 111 - Residual Stress Measurement #4 - Strain (top) and Stress (bottom)

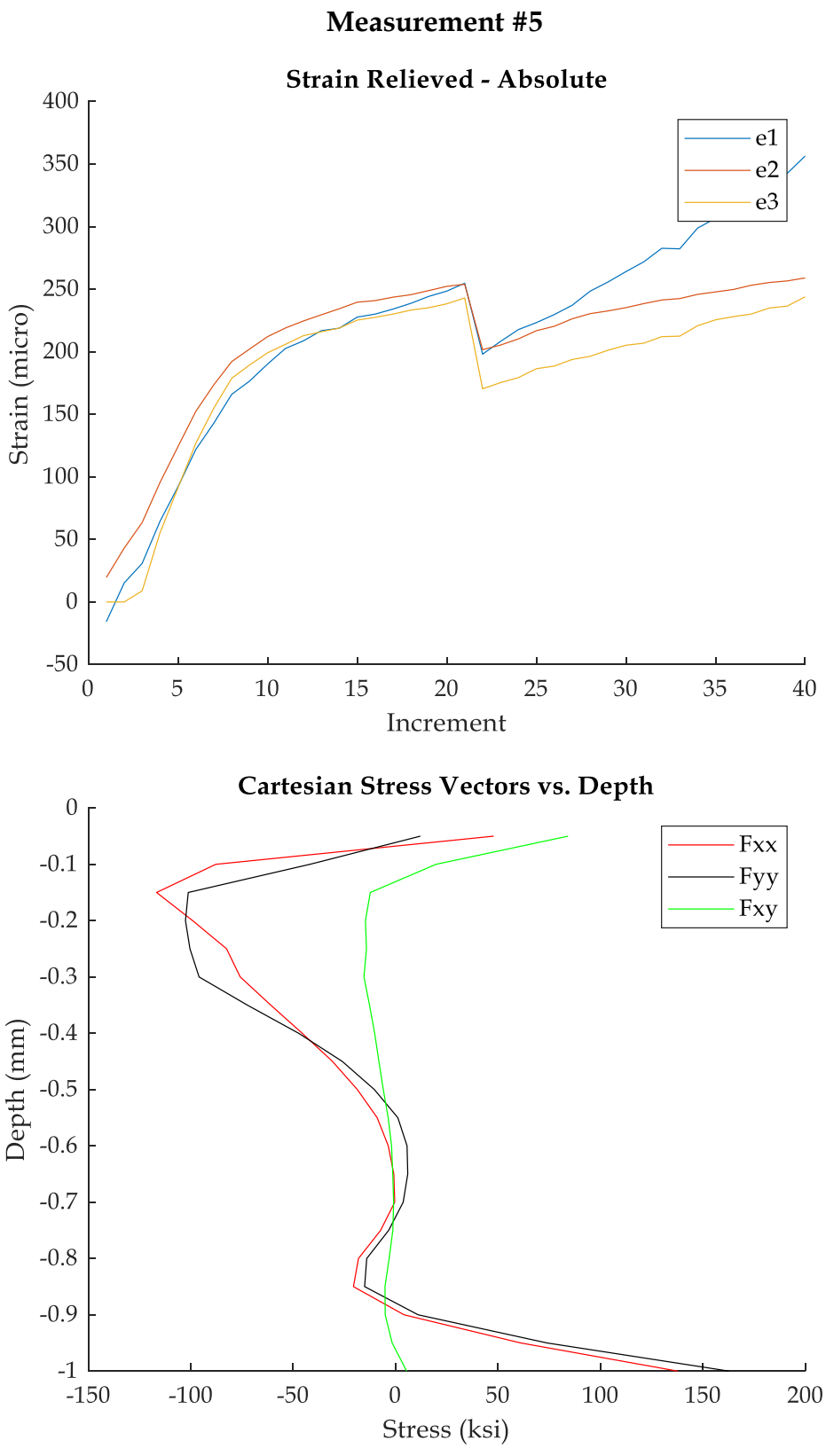

Figure 112 - Residual Stress Measurement #5 - Strain (top) and Stress (bottom)

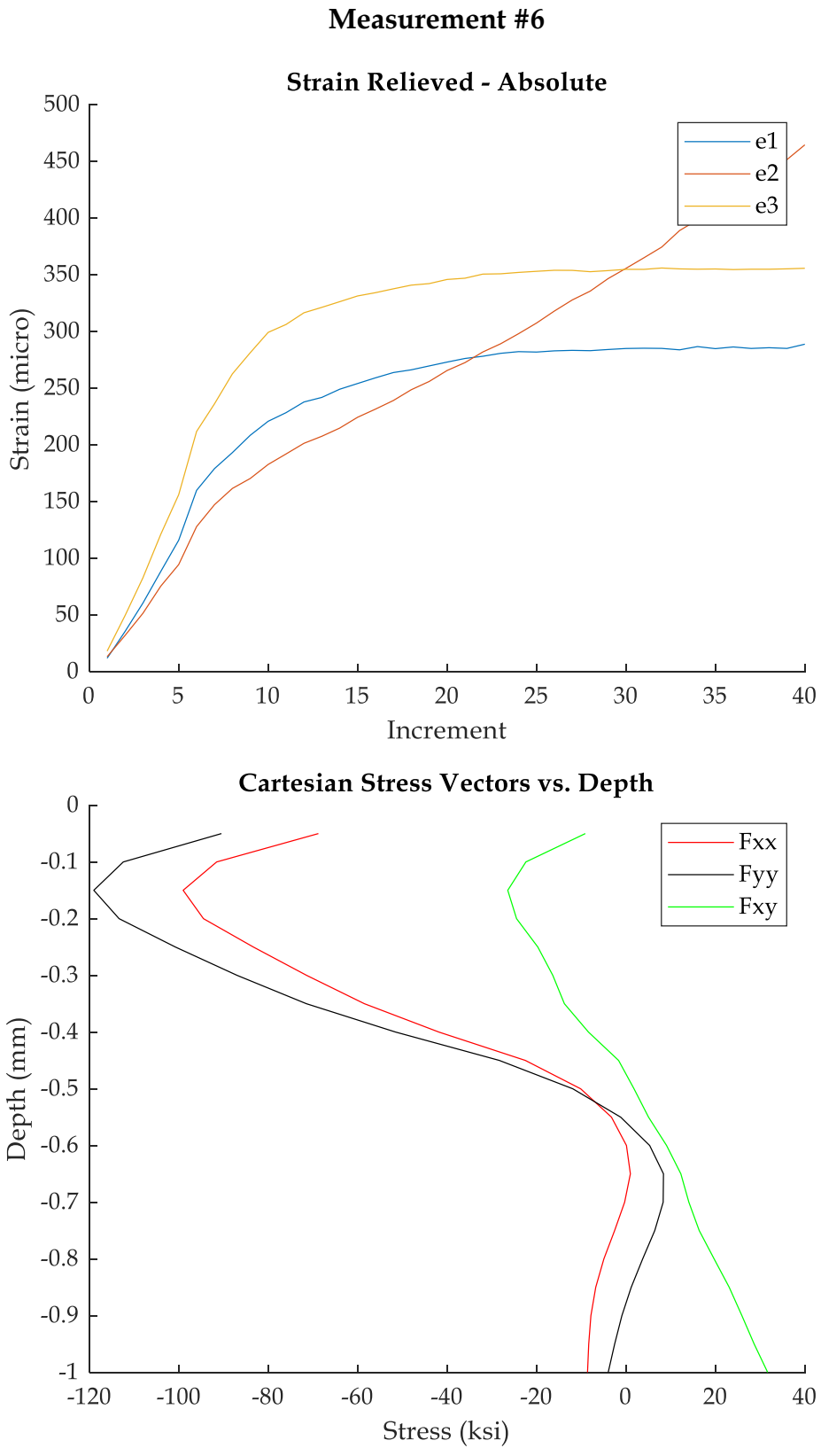

Figure 113 - Residual Stress Measurement #6 - Strain (top) and Stress (bottom)

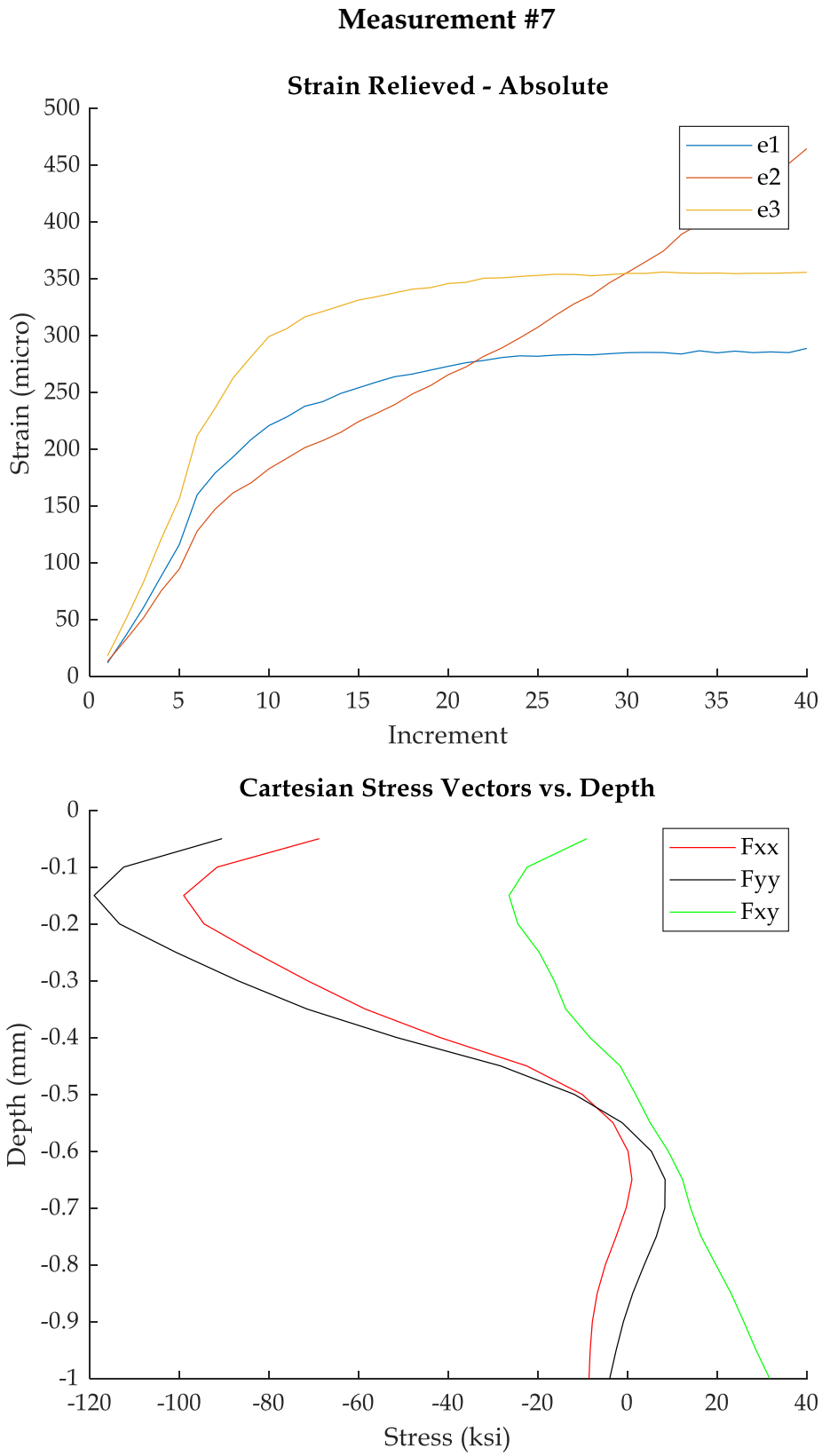

Figure 114 - Residual Stress Measurement #7 - Strain (top) and Stress (bottom)

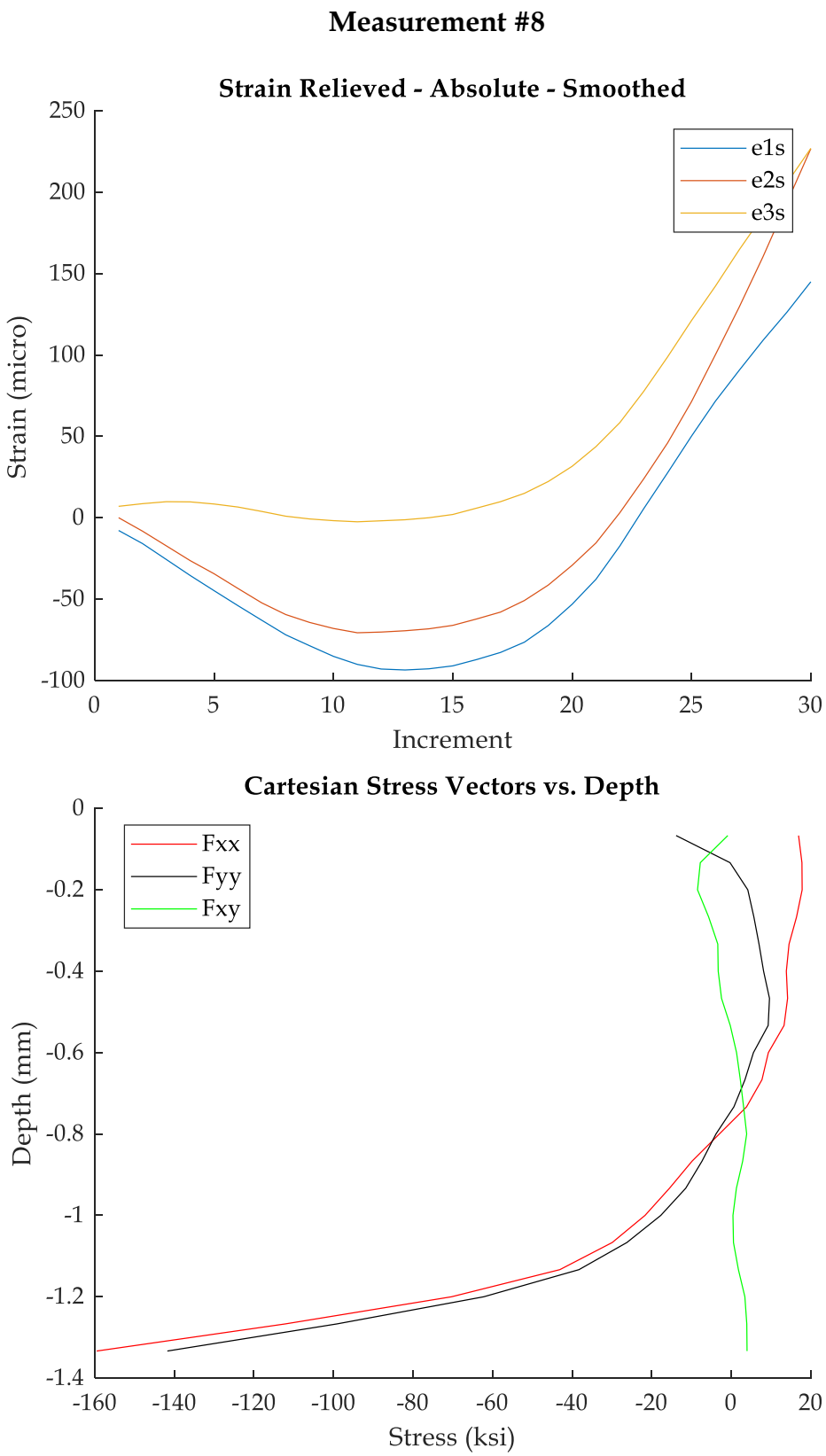

Figure 115 - Residual Stress Measurement #8 - Strain (top) and Stress (bottom)

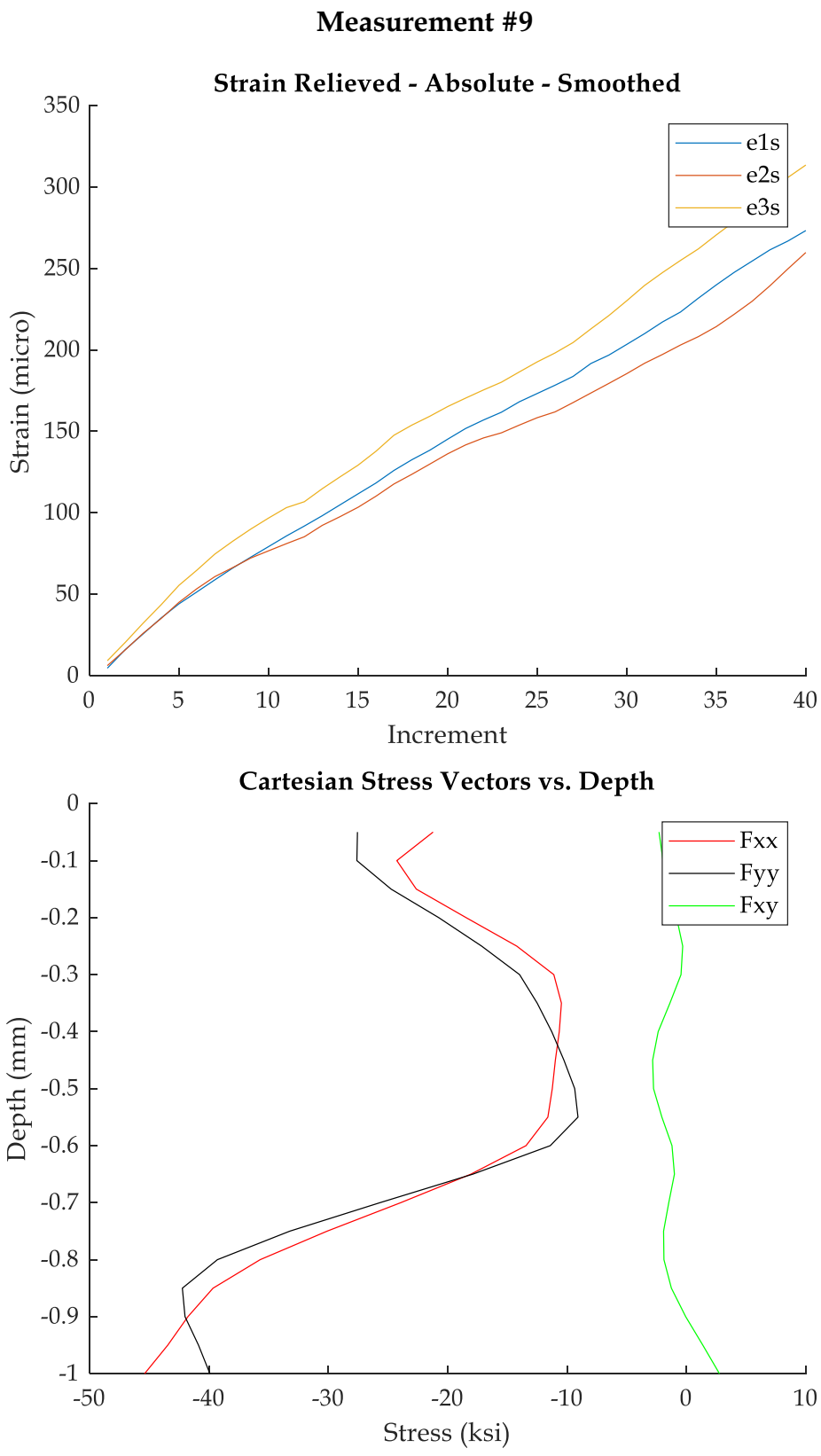

Figure 116 - Residual Stress Measurement #9 - Strain (top) and Stress (bottom)

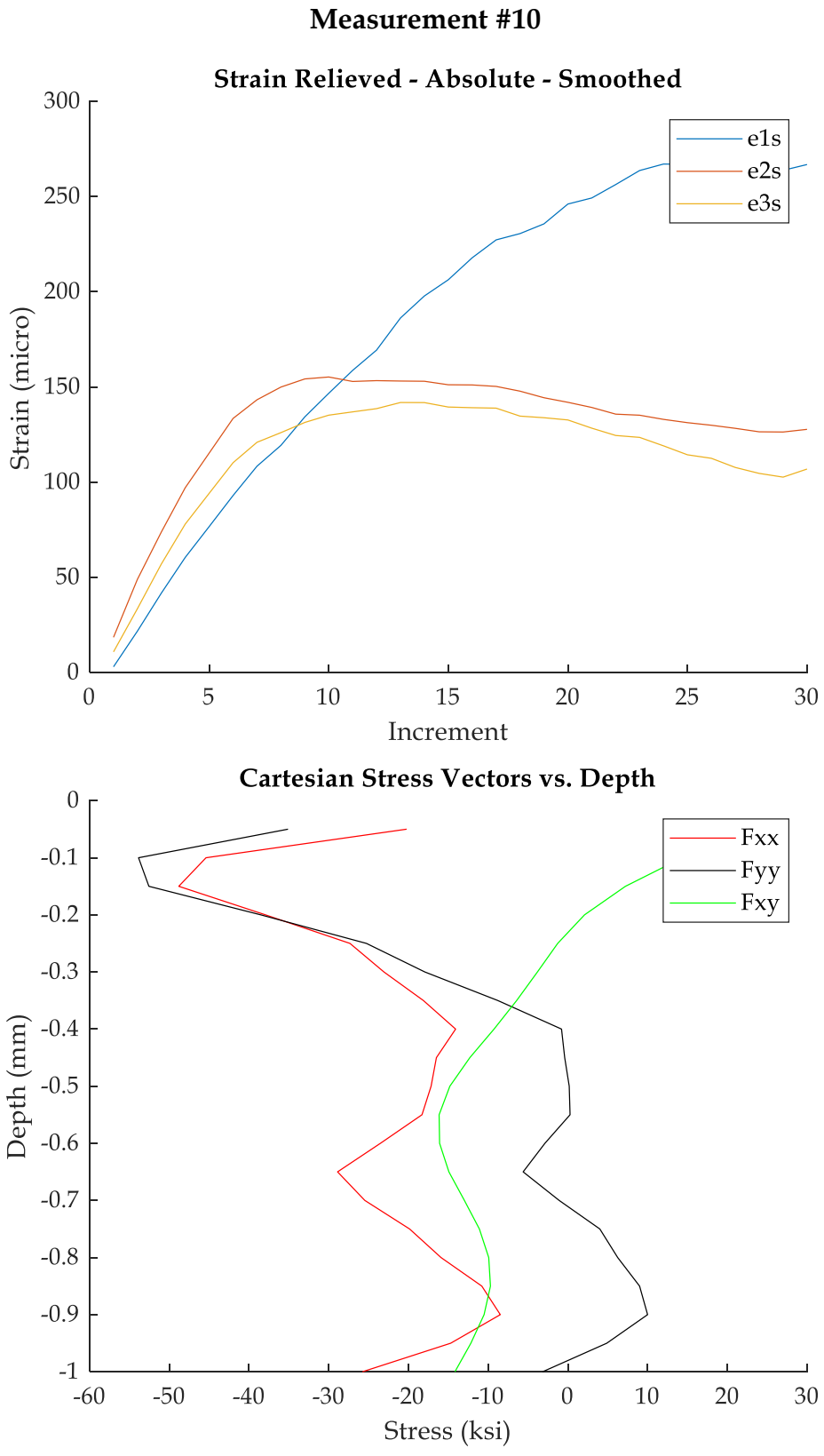

Figure 117 - Residual Stress Measurement #10 - Strain (top) and Stress (bottom)

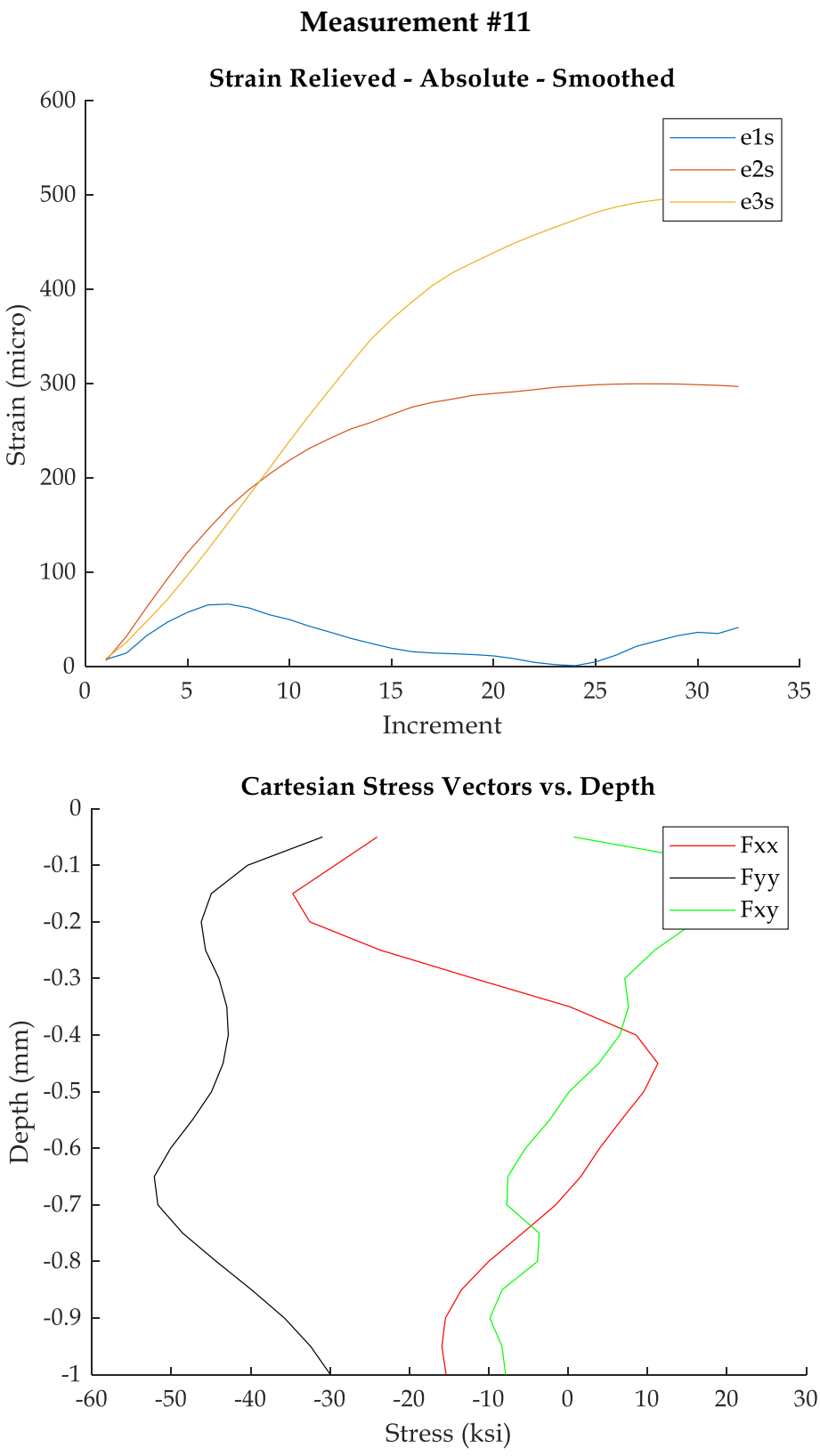

Figure 118 - Residual Stress Measurement #11 - Strain (top) and Stress (bottom)